University of Nevada, Reno

Power System Transient Diagnostics Based on Novel Traveling Wave Detection

A dissertation submitted in partial fulfillment of the
requirements for the degree of Doctor of Philosophy in
Electrical Engineering

By

Reza Jalilzadeh Hamidi
Dr. Hanif Livani, Dissertation Advisor

August, 2017

THE GRADUATE SCHOOL

We recommend that the dissertation
prepared under our supervision by

REZA JALILZADEH HAMIDI

Entitled

Power System Transient Diagnostics Based on Novel Traveling Wave Detection

be accepted in partial fulfillment of the
requirements for the degree of

DOCTOR OF PHILOSOPHY

Dr. H. Livani, Advisor

Prof. M. Sami-Fadali, Committee Member

Prof. M. Etezadi-Amoli, Committee Member

Dr. M. Ben-Idris, Committee Member

Prof. T. Quint, Graduate School Representative

David W. Zeh, Ph. D., Dean, Graduate School

August, 2017

ABSTRACT

Modern electrical power systems demand novel diagnostic approaches to enhancing the system resiliency by developing the state-of-the-art algorithms. The proliferation of high-voltage optical transducers and high time-resolution measurements provide opportunities to develop novel diagnostic methods of very fast transients in power systems. At the same time, emerging complex configurations, such as multi-terminal hybrid transmission systems, limit the applications of the traditional diagnostic methods, especially in fault location and health monitoring.

The impedance-based fault-location methods are inefficient for cross-bounded cables, which are widely used for connection of offshore wind farms to the main grid. Thus, this dissertation first presents a novel traveling wave-based fault-location method for hybrid multi-terminal transmission systems. The proposed method utilizes time-synchronized high-sampling voltage measurements. The traveling wave arrival times (ATs) are detected by observing the squares of wavelet transformation coefficients. Using the ATs, an over-determined set of linear equations are developed for noise reduction, and consequently, the faulty segment is determined based on the characteristics of the provided equation set. Then, the fault location is estimated. The accuracy and capabilities of the proposed fault location method is evaluated and also compared to the existing traveling-wave-based method for a wide range of fault parameters.

In order to improve power systems stability, auto-reclosing (AR), single-phase auto-reclosing (SPAR), and adaptive single-phase auto-reclosing (ASPAR) methods have been developed with the final objectives of distinguishing between the transient and permanent faults to clear the transient faults without de-energization of the solid phases. However, the

features of the electrical arcs (transient faults) is severely influenced by a number of random parameters, including the convection of the air and plasma, wind speed, air pressure, and humidity. Therefore, the dead-time (the de-energization duration of the faulty phase) is unpredictable. Accordingly, conservatively long dead-times are usually considered by protection engineers. However, if the exact arc distinction time is determined, the power system stability and quality will be enhanced. Therefore, a new method for detection of arc extinction times leading to a new ASPAR method utilizing power line carrier (PLC) signals is presented. The efficiency of the proposed ASPAR method is verified through simulations and compared with the existing ASPAR methods.

High-sampling measurements are prone to be skewed by the environmental noises and analog-to-digital (A/D) converters quantization errors. Therefore noise-contaminated measurements are the major source of uncertainties and errors in the outcomes of traveling wave-based diagnostic applications. The existing AT-detection methods do not simultaneously provide enough sensitivity and selectivity. Therefore, a new AT-detection method based on short-time matrix pencil (STMPM) is developed to accurately detect ATs of the traveling waves with low signal-to-noise (SNR) ratios. As STMPM is based on matrix algebra, it is a challenging to implement this new technique in microprocessor-based fault locators. Hence, a fully recursive and computationally efficient method based on an adaptive discrete Kalman filter (ADKF) is introduced for AT-detection, which is proper for microprocessor implementation and can accomplish accurate AT-detection for online applications such as ultra-high-speed protection. Both proposed AT-detection methods are evaluated based on extensive simulation studies and the superior outcomes are compared to the existing methods.

Acknowledgements

I am deeply indebted to Dr. Hanif Livani, my advisor and the committee chair, for giving me the opportunity to be part of a unique research opportunity. He provided me valuable advice, encouragement, and support during my graduate study. My sincere appreciation to the members of my graduate advisory committee, Drs. M. Sami-Fadali, M. Ben-Idris, T. Quint, and M. Etezadi-Amoli for their insightful comments and time.

Table of Contents

Chapter 1. Introduction....1
1.1 Background and Motivation....1
1.2 Contributions....3
1.2.1 Traveling-Wave-Based Fault location algorithm for Hybrid Multi-Terminal Circuits....3
1.2.2 Adaptive Single-Phase Auto-Reclosing Method using Power Line Carrier Signals....4
1.2.3 Traveling-Wave Arrival-Time Detection....5
1.3 Dissertation Organization....6
Chapter 2. Traveling Wave-Based Fault Location Algorithm for Hybrid Multi-Terminal Circuits....7
2.1 Introduction....7
2.2 Proposed Fault location Method....11
2.3 Theory of the Proposed Method....11
2.4 Algorithm....15
2.5 Simulation Results and Discussions....16
2.5.1 Illustrative Test Case....19
2.6 Fault Type and Grounding....21
2.7 Comparison....32
2.8 Conclusion....33
Chapter 3. Adaptive Single-Phase Auto-Reclosing Method using Power Line Carrier Signals....35
3.1 Introduction....35
3.2 Technical Background and Methodology....39
3.2.1 2. 1. Power Line Carriers....40
3.2.2 2. 2. Transient Faults and Secondary Arcs....40
3.3 Proposed ASPAR Method....41
3.3.1 2. 3. 1. Proposed Method Flowchart....45
3.4 Test Cases and Simulation Results....47
3.4.1 Sensitivity Assessment....49
3.4.2 Power System Frequency....49
3.4.3 Fault Location....50
3.4.4 Faulty Phase....50
3.4.5 System Loading....51
3.4.6 Transmission Line Transposition....52
3.4.7 Shunt Reactor Effect....52
3.4.8 PLC Carrier Frequency and Operating Mode....53
3.5 Comparison....53
3.6 Conclusion....55
Chapter 4. Traveling-Wave Arrival-Time Detection....56
4.1 Introduction....56
4.2 Traveling-wave detection technique using short-time matrix pencil method....59
4.2.1 Short-Time Matrix Pencil Method (STMPM)....59
4.2.2 Trace of Arriving Waves and STMPM Formulation....61
4.2.3 STMPM Formulation....62
4.2.4 Arrival Time Detection....64
4.2.5 The Proposed Technique Flowchart....66
4.2.6 Computational Burden of the Method....67
4.2.7 Test Case....68

4.2.8 Arrival Time Detection 69
4.2.9 Comparison 81
4.3 Recursive Method for Traveling Wave Arrival Time Detection in Power Systems 83
4.3.1 Introduction 83
4.3.2 Methodology 84
4.3.3 Case Study and Discussion 92
4.3.4 Comparison 102
4.3.5 Conclusion 103
Chapter 5. Conclusion and Future Work 105
Appendix A 108
A. 1 ……. 108
A. 2 ……. 109
A. 3 ……. 109
Appendix B 111
Appendix C 112
C. 1 ……. 112
C. 2 ……. 112
Appendix D 114
D. 1 ……. 114
D. 2 ……. 115
D. 3 ……. 115
References 116

Table of Figures

Figure 1. Timescale of different phenomena in power systems, figure from [1]. 2
Figure 2. One-line diagram of hybrid multi-terminal transmission systems (equipped with transient recorders and GPS signal receivers). 8
Figure 3. Lattice diagram of traveling waves initiated by a fault in Segment 1-J. 11
Figure 4. The flowchart of the proposed fault location algorithm. 16
Figure 5. One-line diagram of the test case (seven-terminal hybrid system). 17
Figure 6. WTC^{2}s of mode-1 voltages in scale-1, SLG fault in the overhead line at 50 mi from Terminal 1, Fs $=$ 200 kHz, and Zf $= 1\ \Omega$. 18
Figure 7. Three phase voltages at Terminal 2 (SLG fault in the middle of Segment 2-J, Zf $= 1\ \Omega$, FIA $= 8^0$). (a) Grounded system. (b) Ungrounded system. 23
Figure 8. Noise and arriving waves for a fault in the middle of Segment 1-J (Fs $= 500$ kHz, Zf $= 1\ \Omega$, FIA=8^0). The arriving waves at Terminals 1 to 4 are distinguishable from noise. However, the arriving waves at Terminals 5 to 7 disappears in the noise because of the larger attenuation factors of Segments 5-J, 6-J and 7-J. 26
Figure 9. The mode-1 voltages at the overhead line terminal for faults in the middle of the overhead line, Zf $=$ R $+$ jXL $= 10\ \Omega$ and *X/R* ratio is variant. 28
Figure 10. The effects of arc leader propagation and long arc on the proposed method (fault in the overhead line at 50 mi from Terminal 1, FS $= 200$ kHz). (a) The current through arc channel. (b) The mode-1 voltage at Terminal 1. (c)-(i) Normalized WTC^{2}s at Terminals 1 to 7. 29
Figure 11. Fault location errors along the segments, Zf $= 1\ \Omega$, FIA $= 8^0$, FS $= 200$ kHz. 32
Figure 12. Schematic of PLC coupling. 40
Figure 13. The sequence of the events during the arc lifetime. (a) Typical voltage of a faulty phase. (b) Dynamic arc resistance. (c) The path that PLC signals pass through. (d) Typical PLC signal amplitude. P1 shows fault inception. P2 shows de-energization of the faulty phase by the protection system (e.g., distance relays along with CBs). P3 indicates the secondary arc extinction. 42
Figure 14. The PLC signal traveling waves at the fault location. 43
Figure 15. (a) The PLC signal amplitude in a short span before arc extinction. 44
Figure 16. The flowchart of the proposed method. 47
Figure 17. Single-line diagram of the test transmission lines. 48
Figure 18. (a) Pulse-shape signal and sliding window. (b) Reconstructed pulse by STMPM and sliding discrete Fourier transform (SDFT) with the same number of terms. The sampling frequency is 200 kHz. ..60
Figure 19. The complex frequencies extracted by applying STMPM to the pulse shown in Figure 1(a). Diamonds, circles, and squares show the complex frequencies when the pulse is in the right, middle, and left side of the sliding window, respectively. 61
Figure 20. A typical fault-induced arriving wave. The fault inception time is set such that the first arriving wave reaches the ending terminal at 7.5 ms. The sampling frequency is 100 kHz. 64
Figure 21. (a) The damping factor-time diagram obtained by applying STMPM to the measurement shown in Figure 3. (b) The fitted line to the dispersed damping factors, and its zero-crossing point. 64
Figure 22. The estimated arrival times for the first four arriving waves shown in Figure 20. 66
Figure 23. The flowchart of the proposed technique. 67
Figure 24. One-line diagram of the test system. 69
Figure 25. Arrival time detection by different techniques. (a) the aerial mode of three-phase voltage measurement at Terminal 1. (b) Normalized WTC^{2}s with db-4 in scale 1. (c) Normalized WTC^{2}s with db-4

in scale 2. (d) Normalized WTC^{2}s with Haar in scale 1. (e) Normalized squared instantaneous frequency. (f) The proposed technique. 71
Figure 26. Arrival time detection by different techniques. (a) The aerial mode of three-phase voltage measurement at Terminal 1. (b) Normalized WTC^{2}s with db-4 in scale 1. (c) Normalized WTC^{2}s with db-4 in scale 2. (d) Normalized WTC^{2}s with Haar in scale 1. (e) Normalized squared instantaneous frequency. (f) The proposed technique. 72
Figure 27. Fault location error, SLG fault at 100 mi away from Terminal 1, $Zf = 5\ \Omega$, and $FIA = 30^0$, and $FS = 200$ kHz. (a) Noiseless case. (b) $SD = 0.005$Vp. (c) $SD = 0.0075$Vp. (d) $SD = 0.01$Vp. (e) $SD = 0.0125$Vp. 74
Figure 28. Fault location error, SLG fault at 1 mi away from Terminal 1, $Zf = 5\ \Omega$, and $FIA = 30^0$, and $FS = 200$ kHz. (a) Noiseless case. (b) $SD = 0.005$Vp. (c) $SD = 0.0075$Vp. (d) $SD = 0.01$Vp. (e) $SD = 0.0125$Vp. 75
Figure 29. Arriving waves at Terminals 1 and 2 for different Xf/Rf ratios. 77
Figure 30. Fault location errors related to $Zf = Rf + jXf = 2\ \Omega$ with a variant Xf/Rf ratio. Tech. indices are: 1, the proposed technique; 2, db-4 in scale 1; 3, db-4 in scale 2; 4, Haar; and 5, HT. 77
Figure 31. Fault location errors along the transmission line with different sampling frequencies, SLG fault, $Zf = 1\ \Omega$, and $FIA = 90^0$. 81
Figure 32. Typical aerial mode of voltage and current measurements with a high sampling rate after the occurrence of a fault. The voltage level is 230 kV and the sampling frequency is 200 kHz. 84
Figure 33. The flowchart of the proposed method. 85
Figure 34. One-line schematic of the test case 1. 91
Figure 35. An SLG fault in the middle of the line at $t = 250$ ms and $Zf = 1\ \Omega$. (a) and (b) the measured and estimated signals as well as the normalized residual in the beginning of the method. (c) and (d) the estimated and measured signals and also the normalized residuals after the buffering time. (e) and (f) the fault-induced arriving wave and the corresponding normalized residual that is larger than the EWMA threshold. (g) and (h) the entire measurement and normalized residuals during the procedure. 94
Figure 36. Fault location errors, SLG fault in the middle of the line, $Zf = 10\ \Omega$, $FIA = 150$, and $FS = 200$ kHz. (a) $\sigma 2 = 0.075$Vp. (b) $\sigma 2 = 0.01$Vp. (c) $\sigma 2 = 0.0125$Vp. 96
Figure 37. Fault location errors with respect to the sampling frequency. (a) The fault is 5 mi away from Bus 1 ($AFL = 5$ mi). (b) The fault is 10 mi away from Bus 1 ($AFL = 10$ mi). 98
Figure 38. Fault-impedance effect on the arriving waves at Bus 1, $AFL = 10$ mi from Bus 1, $Fs = 200$ kHz, $Zf = Rf + jXf = 2\ \Omega$, and $FIA = 90^0$ 99
Figure 39. Fault-impedance effect on fault location errors. 100
Figure 40. (a) the schematic of the test system in RSCAD. (b) The schematic of the hardware for converting the analog measurements to digital and sent to MATLAB. 101
Figure 41. (a) and (b) show the arriving waves at Buses 1 and 2, respectively. (c) and (d) show the corresponding normalized residuals and the ATs. 102
Figure 42. (a) Typical fault induced distortion in the voltage waveform. (b) db-4 mother wavelet. (c) The resulted normalized WTC^2. 110
Figure 43. The relationship between FIA and arriving waves. (a) $FIA \approx 90^0$. (b) $FIA \approx 15^0$. (c) $FIA \approx 0^0$. 110
Figure 44. One-line diagram of the hybrid three-terminal test case. 113

List of Tables

Table 1. Traveling times in different segments 20
Table 2. Relation between fault type and error 22
Table 3. Effect of FIA 24
Table 4. Relation between the Sampling Frequency and Errors....25
Table 5. Comparison of the Fault Location Methods 33
Table 6. Timer start and stop times corresponding to Figure 15. 45
Table 7. Specifications of the test systems. 48
Table 8. Delays in detection of arc extinction 50
Table 9. Delays in detection of arc extinction 51
Table 10. Delays in detection of arc extinction 51
Table 11. Delays in detection of arc extinction 52
Table 12. Noise efficiency....54
Table 13. Comparison of the existing and proposed methods 54
Table 14. Processing times of the proposed algorithm steps 68
Table 15. Absolute errors resulted from different techniques 72
Table 16. The effect of FIA on fault location....78
Table 17. Comparison of the AT-detection methods....82
Table 18. Harmonic Contents in the Voltage 91
Table 19. The effect of FIA on fault location....97
Table 20. Average fault location errors in Test Case 2 102
Table 21. Comparison of the AT-detection methods....103
Table 22. Fault location accuracy....113

Chapter 1. Introduction

1.1 Background and Motivation

Conventional protective relays and meters are designed to detect and possibly record the events in power grids for a frequency range of up to several harmonics of the nominal frequency. However, the events, such as lightning, switching, and faults, generate traveling waves moving along the conductors at a pace up to the speed of light. These traveling waves contain high frequency contents as high as several megahertz (MHz). Therefore, the measuring or protective devices cannot detect the traveling waves. Figure 1 depicts the timescale of different phenomena in power systems. In the timescale classification, the fastest transients such as switching surges and lightning propagation, are classified as transients or fast transients [1] and [2]. The lifespans of electrical transients are short, however, the power systems components are exposed to high-current and high-voltage peaks, resulting in considerable damages to the power components during transient events. Moreover, detection of the source of traveling waves has applications in power system diagnostics and preventive maintenance that are crucial for decreasing the outage rates, and increasing the power system resiliency. On the other hand, power systems have become more complex with new topologies and components (i.e., submarine cables for integration of offshore wind farms, power electronic-based components) being emerged, and the current diagnostic methods may be ineffective. At the same time, as the demand for electrical energy is drastically increasing, power outages are not acceptable [3] and [4]. Accordingly, new diagnostic methods applicable to the emerging advanced high-frequency transient measurement technologies are required. The new measurement technologies

provide foundational opportunities for very-fast electromagnetic transient events analysis and diagnostics.

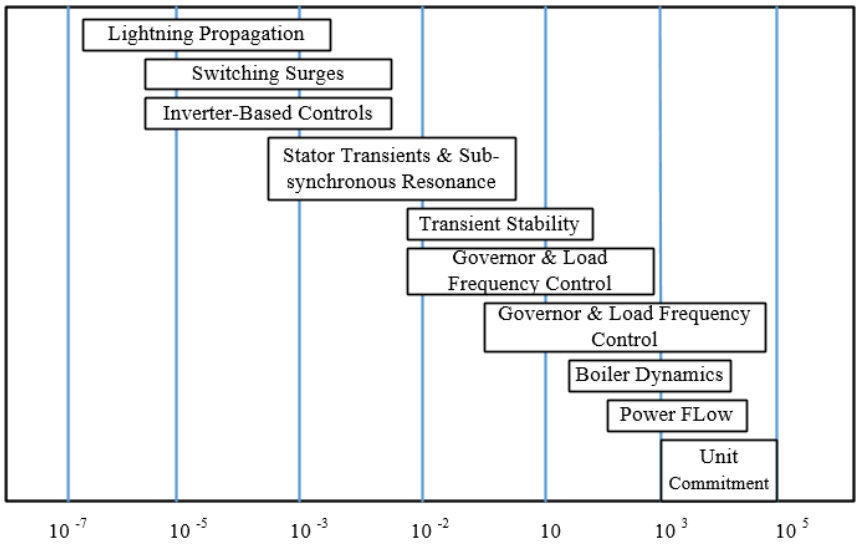

Figure 1. Duration of different events in power systems, [1].

Power system transient studies started in 1880's by Oliver Heaviside who developed a transmission line model for transient studies. Based on the model suggested by Heaviside, the telegraph equations are developed, that is, a pair of linear differential equations (DEs) describing the voltage and current along a transmission line based on the traveling wave concept. However, the analytical approach provided by Heaviside is restricted to linear circuits. In the case of complex networks, the application of the abovementioned method becomes deficient due to the complexity and nonlinearity of power system components. Therefore, numerical approaches are required to perform transient analysis. In 1950, it was first shown that the design of a switchgear is closely related to electrical transient phenomena [5]. In 1951, different realistic examples regarding faults, sudden loss of load, and switching surges based on transient simulations were published in [6]. Since then, the research on power system transients has continued and different diagnostic applications

based on traveling waves such as fault location and health monitoring, are proposed [7], [8]-[18]. Recently, wide-area monitoring and diagnostics of fast transient events using high-frequency time-synchronized measurements is presented in [19] and [20]. Electromagnetic transient events (EMTEs) are short-duration events (i.e., in order of microseconds) with high-frequency contents that may remain hidden from grid operators. EMTEs can lead to failure in power system equipment (e.g., transformers). For example, the arriving waves caused by a switching lead to overvoltages over the insulators [21] and [22]. Therefore, diagnostics of fast EMTEs in transmission grids increase the situational awareness of such abnormal events and can be used by utilities to prioritize the targeted and preventive maintenance scheduling[1].

1.2 Contributions

The main contributions of this dissertation are concisely described below under three main subjects, and then the proposed solutions are discussed through the corresponding chapters.

1.2.1 Traveling-Wave-Based Fault location algorithm for Hybrid Multi-Terminal Circuits

A novel traveling wave-based fault location algorithm is proposed for hybrid multi-terminal transmission systems that consist of one onshore overhead line and multiple offshore submarine cables. Such hybrid transmission systems are common for interconnection of offshore wind farms to the main grid. The input to the algorithm is time-synchronized high-resolution transient voltage measurements from all of the substations.

[1] Reprinted in line with copyright and author-rights for "Wide-area electromagnetic transient events (EMTE) classification in transmission grids," by M. Khoshdeli, I. Niazazari, R. J. Hamidi, H. Livani, and B. Parvin, Jul. 2017, IEEE PES General Meeting.

These measurements are obtained by optical voltage transducers equipped with Global Positioning System (GPS) receivers for time synchronization. The discrete wavelet transformation is utilized to decompose the mode-1 voltages at the receiving ends. The first wave arrival times (ATs) are then obtained by observing the squares of the wavelet transformation coefficient (WTC^2s). Through an apriori provided over-determined set of linear equations based on the power grid topology, the faulty segment of the transmission system, and consequently, the location of the fault are estimated. The transient simulations and the post fault analysis are carried out using EMTP-RV and MATLAB Wavelet Toolbox, respectively. The accuracy, limitations, and capabilities of the proposed algorithm are presented and discussed for different fault conditions in the corresponding chapter.

1.2.2 Adaptive Single-Phase Auto-Reclosing Method using Power Line Carrier Signals

A new method for adaptive single-phase auto-reclosing (ASPAR) in transmission lines is proposed that improves the rate of successful reclosing actions after the occurrence of a transient single-phase fault, and prevents unsuccessful reclosing. After the occurrence of a fault, the only faulty phase is disconnected by the protection system (e.g., distance relays and circuit breakers). The proposed method deploys power line carrier (PLC) signals for determination of the secondary arc extinction time and releasing the reclosing signals to the circuit breakers. In spite of the growing use of new communication systems (e.g., fiber-optic links), PLC systems are still widely used, cost-effective, and reliable, and may not be considered for replacement in the next decades. Therefore, the proposed method can be utilized as an auxiliary application of PLC systems to enhance the resiliency and stability

of power grids. The simulation studies are carried out using EMTP-RV and MATLAB, and the advantages and disadvantages of the proposed method are discussed and compared with the existing ASPAR methods in Chapter 3.

1.2.3 Traveling-Wave Arrival-Time Detection

The first step in dealing with traveling waves is to detect their arrival times (ATs). In this regard, this dissertation proposes two novel AT-detection methods to enhance the existing AT-detection techniques as follows:

● First, a new technique is proposed for detection of traveling wave arrival times (ATs) in power systems that is robust against high-resolution measurement noise. Accurate estimation of traveling wave ATs enhances most of traveling wave-based fault-location methods. The proposed technique is based on the short-time matrix pencil method (STMPM) that decomposes the measurement samples in a sliding window into time-indexed complex frequencies. Traveling wave ATs are estimated based on the fact that the extracted damping factors (i.e., the real part of the complex frequencies) are zero when the arriving wave is located in the middle of the sliding window. The proposed technique is compared to the existing AT-detection techniques such as discrete wavelet transformation (DWT) with commonly used mother wavelets and Hilbert transformation (HT), using MATLAB Wavelet Toolbox and MATLAB Hilbert transformation. The sensitivity analysis based on the simulation results demonstrates that the proposed technique is less affected by the measurement noise, sampling frequency, and fault parameters.

● Second, a robust and computationally efficient recursive method for detection of the first traveling wave arrival times (ATs) in power grids is proposed, that enhances the performance of the traveling wave-based fault-location methods relying on the first wave

ATs. The proposed method is based on the detection of the abrupt changes in the innovation sequence (residuals) generated by an adaptive discrete Kalman filter (ADKF). As the proposed method is recursive, it is proper for being implemented in microprocessors for online applications. The transient simulations are carried out using EMTP-RV and RSCAD (RTDS) with A/D converter-in-the-loop. The simulation results are then fed into MATLAB for evaluation of the proposed method. The performance of the proposed method is compared to the state-of-the-art AT-detection methods such as discrete wavelet transformation (DWT) with commonly used mother wavelets, Hilbert transformation (HT), and short time matrix pencil method (STMPM). The sensitivity analysis based on the simulation results demonstrates that the proposed method is less affected by the measurement noises as well as fault parameters.

1.3 Dissertation Organization

This dissertation is organized following 'Alternative Formatting for Dissertations' [24]. The main contributions of this dissertation are organized in three chapters. As the contributions in any chapter follow specific goals, a detailed literature review and problem statement is presented in the beginning of each chapter. The proposed methodologies, results, and discussion are then provided accordingly. Therefore, the remaining of the dissertation is as follows: In Chapter 2, a new traveling wave-based fault location method for hybrid multi-terminal transmission lines is described. In Chapter 3, the application of PLC signals in adaptive single-phase auto-reclosing (ASPAR) is presented for the first time. In chapter 4, two novel and robust AT-detection methods based on STMPM and Kalman filter are presented. In Chapter 5, the conclusion and future works are presented.

Chapter 2. Traveling Wave-Based Fault Location Algorithm for Hybrid Multi-Terminal Circuits[2]

This chapter introduces a new fault-location algorithm able to determine the location of faults in hybrid multi-terminal transmission systems. The synchronized transient voltages at all of the receiving ends are measured and fed into the proposed algorithm. The transient measurements are acquired by means of optical voltage transducers along with global positioning system (GPS) signal receivers. The discrete wavelet transformation (DWT) is used for time-frequency decomposition of the obtained mode-1 (i.e., aerial mode) voltages. The arrival times (ATs) of the fault-induced traveling waves are detected by observing the squares of the wavelet transformation coefficient (WTC^2s). The transient simulations and post fault analysis are carried out using EMTP-RV and MATLAB Wavelet Toolbox, respectively. The pros and cons of the proposed algorithm are provided and discussed for a variety of fault conditions.

2.1 Introduction

Nowadays, a growing number of wind farms are deployed in offshore areas. Offshore wind farms are often connected to the main grid via a hybrid transmission system consisting of an overhead line, a collector bus, and several submarine (subsea) cables, as shown in Figure 2 [24] and [26]. Accurate fault location is a necessary post-fault tool that results in a quick system restoration after a fault and prevents more economic losses. Fault location in submarine transmission systems is a challenging task due to the following reasons:

[2] Reprinted in line with copyright and author-rights for "Traveling wave-based fault location algorithm for hybrid multi-terminal circuits," by R. J. Hamidi and H. Livani, Feb. 2017, IEEE Trans. Power Delivery, Vol. 143, No. 1, pp. 135-144.

- Wind farms are mostly built in wild seas, which are harsh working places for maintenance crews.
- Submarine cables are usually Cross-linked PolyEthylene (XLPE) insulated [24]-[27]. The fault arc does not solidly burn through the entire XLPE insulation [28]. Therefore, the fault path is available only when the cable is energized, and thus, offline fault location methods have limited practical applicability.
- Hybrid transmission systems have a relatively complex structure that makes fault location a difficult task.

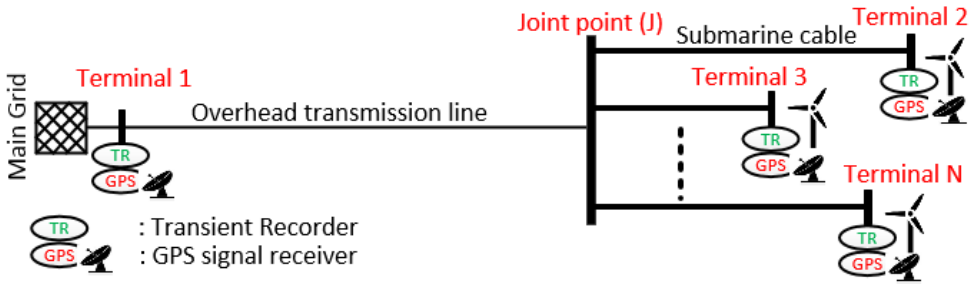

Figure 2. One-line diagram of hybrid multi-terminal transmission systems (equipped with transient recorders and GPS signal receivers).

Historically, fault location methods are mainly divided into three categories [29]: power frequency-based (i.e., impedance-based), traveling wave-based, and artificial intelligence-based methods. In [30] and [31], it is shown that the zero-sequence impedance of a fault loop and the fault location are not linearly proportional for cross-bonded cables because of discontinuities at the cross-bondings. References [32] and [33] show that the impedance-based methods estimate the fault location in cross-bonded cables only when the faulty major section is identified. In [34], a fault location method based on distributed sequential impedances is presented. This method identifies the faulty section in cross-bonded cables for only single-line-to-ground (SLG) faults. In [35], a power frequency-based fault location method is presented that locates SLG faults in underground cables without laterals. In [36], a power frequency-based method is improved using characteristic frequencies

corresponding to every possible fault location. Due to the above-mentioned limitations, power frequency-based fault location methods have limited applicability for cables.

Traveling wave-based fault location methods are more accurate and reliable compared to power frequency-based methods [37]. The advent of optical high-voltage transducers together with high-frequency transient recorders (TRs) makes traveling wave-based methods practical [38]. In [39], fault initiated traveling waves are extracted and used for fault location. The use of discrete wavelet transformation (DWT) for extracting the traveling waves from the modal voltages is first proposed in [40]. Reference [41] presents a traveling wave-based fault location method for three-terminal transmission systems consisting of three overhead lines. In [43], a fault location method based on current traveling waves for multi-terminal transmission systems is proposed. In [20], synchronized arrival times of the traveling waves are utilized for faulty line identification and fault location in overhead transmission grids. References [26] and [31] demonstrate that the modal transformation reduces the cross-bonding effect, and the use of traveling wave-based fault location methods are thus applicable to hybrid transmission systems. In [44], a single-ended traveling wave-based fault location method for hybrid transmission systems consisting of an overhead line and an underground cable is presented. In [45], a support vector machine (SVM) classifier is utilized for faulty segment and faulty half identification. This method is applicable on the systems comprising one overhead line and one underground cable. In [47], an online fault location method for underground cables is presented that uses sheath currents. In [48], a traveling wave-based fault location method is presented for a hybrid three-terminal transmission system with one overhead line and two submarine cables. Hybrid multi-terminal transmission systems are widely used for

interconnection of offshore wind farms to the main grid. However, custom-designed fault location methods for the mentioned systems have been less addressed in the literature and still remain an open problem.

In this dissertation, the preliminary results in [48] are extended and a traveling wave-based fault location method for hybrid multi-terminal transmission systems consisting of one overhead line and multiple submarine cables is presented. The sensitivity of the proposed algorithm is evaluated for the following parameters: fault type, grounding system, fault inception angle (FIA), transducer bandwidth, TR sampling frequency, fault resistance, non-ideal fault, and non-linear arc. The advantages of the proposed method are: 1) It is not severely affected by the fault parameters. 2) The proposed method is based on an analytical solution and does not require a large number of simulations for training data as required by artificial intelligence-based methods. 3) It estimates fault location via the weighted least squares (WLS) method, which uses the first arrival times of fault induced traveling waves. Therefore, the fault location errors due to measurement uncertainties are reduced.

Our proposed fault location algorithm has the following major steps: 1) Synchronized transient voltages of power system terminals are measured through optical transducers equipped with GPS signal receivers. 2) The Clarke's transformation is applied to the measured voltages for obtaining the mode-1 voltages. 3) Discrete wavelet transformation (DWT) is applied to the calculated mode-1 voltages, and the first arrival times are measured by observing the squares of wavelet transformation coefficient (WTC^2s). 4) The faulty segment identification and fault location are executed using the differences among the measured first arrival times.

2.2 Proposed Fault location Method

The proposed fault location method is based on the following assumptions and requirements: 1) Optical voltage transducers are available at all power system terminals [40] and [43]. 2) The terminals are equipped with GPS signal receivers for synchronizing the transient voltage measurements [43]. 3) Measuring devices at the joint point (so-called, collector bus, "J" in Figure 3) are not required. 4) The wave traveling time (i.e., the time that a traveling wave passes along a segment) in each segment is known a priori [26], [40], and [41].

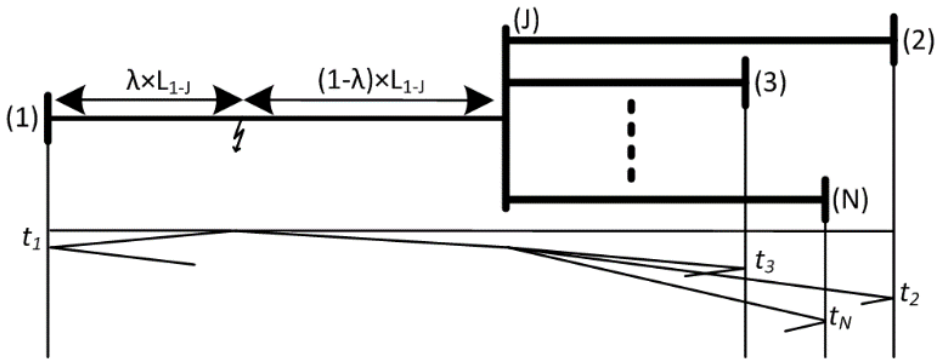

Figure 3. Lattice diagram of traveling waves initiated by a fault in Segment 1-J.

2.3 Theory of the Proposed Method

Synchronized transient voltage measurements are obtained using TRs equipped with GPS signal receivers. DWT is applied to the calculated mode-1 voltages, and the first wave arrival times are measured by observing the WTC^{2}s. Then, the arrival time differences are compared to the a priori known wave traveling time differences. This provides sufficient information for identifying the faulty segment. Once the faulty segment is identified, the fault location is estimated. Figure 3 shows the lattice diagram of a fault in the overhead line (i.e., Segment 1-J). The fault induced first arrival times at Terminals 1 to N are

$$\begin{bmatrix}\tilde{t}_1\\ \tilde{t}_2\\ \vdots\\ \tilde{t}_N\end{bmatrix}=\begin{bmatrix}\lambda & 0 & \dots & 0\\ (1-\lambda) & 1 & \dots & 0\\ \vdots & \vdots & \ddots & \vdots\\ (1-\lambda) & 0 & \dots & 1\end{bmatrix}\begin{bmatrix}\tau_1\\ \tau_2\\ \vdots\\ \tau_N\end{bmatrix}+\begin{bmatrix}t_f\\ t_f\\ \vdots\\ t_f\end{bmatrix}+\begin{bmatrix}\varepsilon_1\\ \varepsilon_2\\ \vdots\\ \varepsilon_N\end{bmatrix} \quad (1)$$

where $\tilde{t}_1$ to $\tilde{t}_N$ [s] are the measured first arrival times at Terminals 1 to N due to an unknown fault location on Segment 1-J. λ is the unknown ratio of the fault-to-terminal distance to the faulty segment length as shown in Figure 3. τ_1 to τ_N [s] are the known wave traveling times in Segments 1-J to N-J, t_f [s] represents fault inception time, which is also unknown, and $\varepsilon_i \sim \mathcal{N}(0, \sigma_i^2), \forall i = 1,2,\dots,N$ are zero-mean Gaussian noises with σ_i^2 variances. The noises are independent, but non-identical. t_f in (1), can be canceled out by subtraction of any two arrival times. Therefore, $\tilde{t}_{mn}$ is defined as

$$\tilde{t}_{mn} = \tilde{t}_m - \tilde{t}_n, \forall (m,n) = 1,2,\dots,N \quad (2)$$

where $\tilde{t}_m$ and $\tilde{t}_n$ [s] are the measured first arrival times, m and n are terminal indices. Applying (2) to (1) yields

$$\boldsymbol{\Delta\tilde{t}} = \begin{bmatrix}0 & \tilde{t}_{12} & \dots & \tilde{t}_{1N}\\ \tilde{t}_{21} & 0 & \dots & \tilde{t}_{2N}\\ \vdots & \vdots & \ddots & \vdots\\ \tilde{t}_{N1} & \tilde{t}_{N2} & \dots & 0\end{bmatrix} \quad (3)$$

where $\boldsymbol{\Delta\tilde{t}}$ is the matrix form of arrival time differences. Each $\tilde{t}_{mn}$ can have only one of the following general forms

$$\begin{cases}\tilde{t}_{mn} = (2\lambda-1)\tau_m - \tau_n + \varepsilon_{mn}, \text{if } m\text{-}J \text{ is faulty}\\ \tilde{t}_{mn} = (1-2\lambda)\tau_n + \tau_m + \varepsilon_{mn}, \text{if } n\text{-}J \text{ is faulty}\\ \tilde{t}_{mn} = \tau_m - \tau_n + \varepsilon_{mn}, \text{neither } m\text{-}J \text{ nor } n\text{-}J \text{ is faulty}\end{cases} \quad (4)$$

In the upper and lower triangular parts of the matrix $\boldsymbol{\Delta\tilde{t}}$, there are $(N-1)$ elements related to the faulty segment and the remaining elements are related to the non-faulty segments. The differences between each pair of the wave traveling times are shown with

$\boldsymbol{\Delta\tau}$ as

$$\boldsymbol{\Delta\tau} = \begin{bmatrix} 0 & \tau_{12} & \dots & \tau_{1N} \\ \tau_{21} & 0 & \dots & \tau_{2N} \\ \vdots & \vdots & \ddots & \vdots \\ \tau_{N1} & \tau_{N2} & \dots & 0 \end{bmatrix} \tag{5}$$

where $\tau_{mn} = \tau_m - \tau_n$, and the wave traveling times are known a priori. In order to compare $\boldsymbol{\Delta\tilde{t}}$ with $\boldsymbol{\Delta\tau}$, the matrix $\boldsymbol{\Delta}$ is defined as follows

$$\boldsymbol{\Delta} = |\boldsymbol{\Delta\tilde{t}} - \boldsymbol{\Delta\tau}| \tag{6}$$

where $|.|$ denotes the absolute value. $\boldsymbol{\Delta}$ is a symmetrical matrix with zero diagonal elements. Referring to (4) and (5), the differences between each $\tilde{t}_{mn}$ and its corresponding τ_{mn} related to non-faulty segments are relatively small (i.e., they are not exactly zero due to the measurement uncertainties). Therefore, a Δ_{mn} related to a non-faulty segment is relatively small. On the contrary, the difference between each $\tilde{t}_{mn}$ and its corresponding τ_{mn} related to the faulty segment is large, and therefore, the corresponding Δ_{mn} is large. Thus, the largest values in $\boldsymbol{\Delta}$ have an index (m or n) equal to the faulty segment, and they are also located in one row and its corresponding column. Accordingly, the row/column number with $(N-1)$ maximal values indicates the faulty segment.

In order to identify the faulty segment, the matrix $\boldsymbol{\Delta}$ is first calculated. Then, the $(N-1)$ maximal values in $\boldsymbol{\Delta}$ are identified. If they are located in the same row/column, the row/column number (denoted by c^*) identifies the ending terminal of the faulty segment (i.e., all the segments have a common end "J", therefore, with one terminal index, the faulty segment can be identified), and thus, the Segment c^*-J is faulty. Otherwise, the faulty segment is unidentifiable and the proposed method is not able to find the fault location. The ability of the proposed method in detection of the faulty segment is discussed in

Appendix A.1.

Once the faulty segment is identified, the elements on the c^*-th column of $\boldsymbol{\Delta\tilde{t}}$ are utilized to provide $(N-1)$ equations for estimation of λ as follows

$$\tilde{t}_{mc^*} = (1-2\lambda)\tau_{c^*} + \tau_m + \varepsilon_{mc^*}, \forall m = 1,2,\dots,N, m \neq c^* \quad (7)$$

where c^* is the terminal index corresponding to the identified faulty segment (c^*-J). τ_{c^*} refers to the wave traveling time in the identified faulty segment. τ_m denotes the wave traveling time in non-faulty segments. Equation (7) is written in matrix form as

$$\boldsymbol{\Delta\tilde{t}}^*_{(N-1)\times 1} = -2\boldsymbol{\tau}^*_{(N-1)\times 1}\lambda + \boldsymbol{\tau}^*_{(N-1)\times 1} + \boldsymbol{\tau}_{(N-1)\times 1} + \boldsymbol{\varepsilon}_{(N-1)\times 1} \quad (8)$$

where

$\boldsymbol{\Delta\tilde{t}}^* = [\tilde{t}_{1c^*}, \tilde{t}_{2c^*}, \dots, \tilde{t}_{mc^*}]^T, \forall m = 1,2,\dots,N, m \neq c^*$

$\boldsymbol{\tau}^* = [\tau_{c^*}, \tau_{c^*}, \dots, \tau_{c^*}]^T$

$\boldsymbol{\tau} = [\tau_1, \tau_2, \dots, \tau_{m,}], \forall m = 1,2,\dots,N, m \neq c^*$

$\boldsymbol{\varepsilon} = [\varepsilon_1 - \varepsilon_{c^*}, \varepsilon_2 - \varepsilon_{c^*}, \dots, \varepsilon_m - \varepsilon_{c^*}]^T, \forall m = 1,2,\dots,N, m \neq c^*.$

In order to make (8) more readable, $\boldsymbol{b} = \boldsymbol{\tau}^* + \boldsymbol{\tau} - \boldsymbol{\Delta\tilde{t}}^*$ is defined, and (8) is rewritten as

$$2\boldsymbol{\tau}^*_{(N-1)\times 1}\lambda = \boldsymbol{b}_{(N-1)\times 1} + \boldsymbol{\varepsilon}_{(N-1)\times 1} \quad (9)$$

Equation (9) is an overdetermined set of linear equations, therefore, λ is estimated using the WLS method as [42]

$$\min_{\lambda} (2\boldsymbol{\tau}^*\lambda - \boldsymbol{b})^T \boldsymbol{R}^{-1} (2\boldsymbol{\tau}^*\lambda - \boldsymbol{b}) \quad (10)$$

Additional explanations for the WLS-based method are provided in Appendix A. 2. Once $\hat{\lambda}$ is calculated (i.e., the estimated value of λ) the fault location is calculated by

$$EFD = \hat{\lambda} \times L \quad (11)$$

where EFD [mi] is the estimated fault-to-terminal distance and L is the length of the

identified faulty segment [mi].

2.4 Algorithm

Figure 4 shows the flowchart of the proposed algorithm with the following steps:

1. Transient three-phase voltages at all terminals are synchronously measured through optical voltage transducers equipped with GPS signal receivers.
2. The Clarke's transformation is applied to the measured voltages to obtain mode-1 voltages. The usage of mode-1 voltages reduces the effect of environmental parameters [31].
3. DWT is utilized to calculate wavelet transformation coefficients (WTCs). We use Daubechies-4 (db-4) mother wavelet in scale-1 for time-frequency decomposition of the synchronized mode-1 voltages at all terminals. A typical fault induced distortion in the voltage waveform, db-4 mother wavelet, and the resulted normalized WTC^2 are provided in Appendix A. 3.
4. The first wave arrival times ($\tilde{t}$) at all the terminals are obtained by observing the WTC^2.
5. Time differences between each pair of the synchronized arrival times ($\tilde{t}_{mn}$) are calculated using (2).
6. In order to compare the matrix $\boldsymbol{\Delta\tilde{t}}$ with $\boldsymbol{\Delta\tau}$, the matrix $\boldsymbol{\Delta}$ is calculated using (6).
7. $(N-1)$ maximal values in the matrix $\boldsymbol{\Delta}$ are found.
8. If all the maximal values are in the same row/column, the row/column number is denoted by c^*, and the faulty segment is c^*-J. Otherwise, the faulty segment is unidentifiable and the proposed method fails to find the fault location.
9. Having found the faulty segment, one can find $\hat{\lambda}$ using (10).

10. The fault location is estimated using (11).

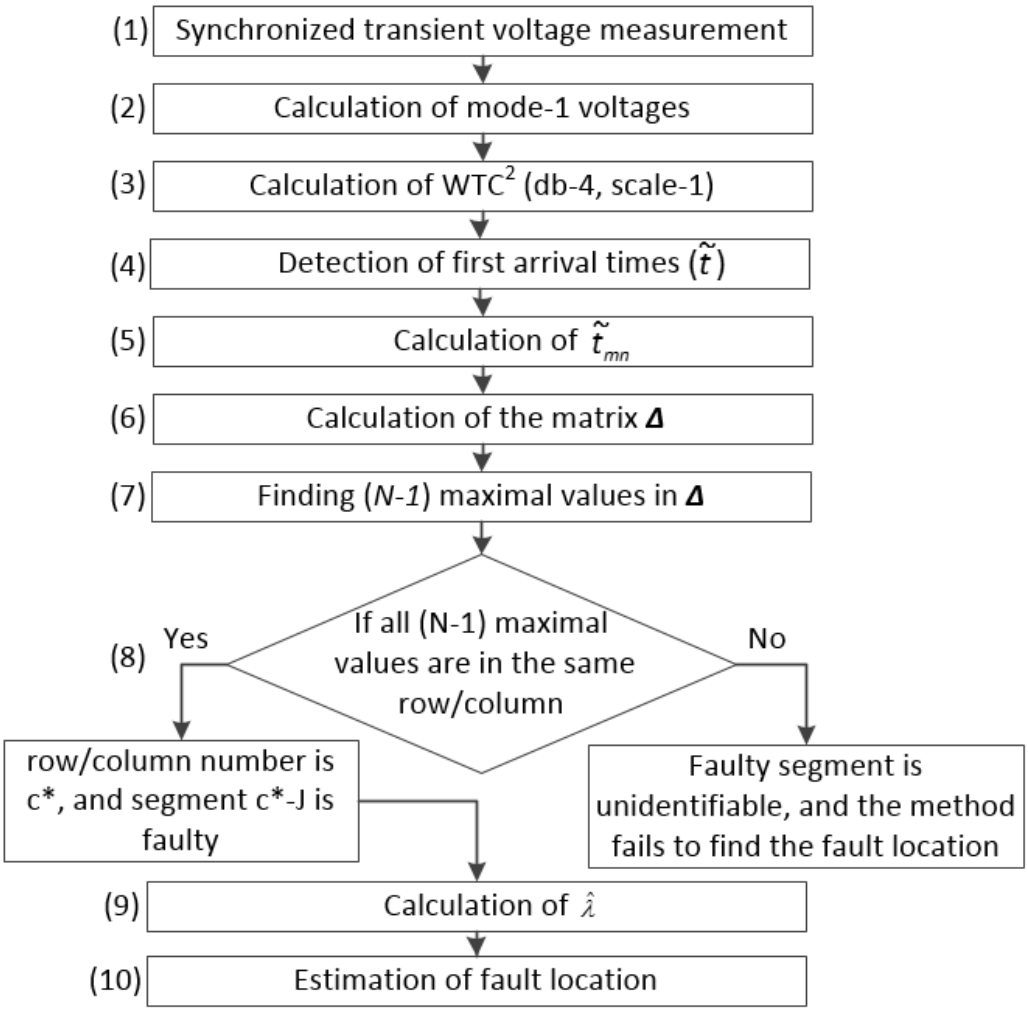

Figure 4. The flowchart of the proposed fault location algorithm.

In the following section, the simulation results and the related discussions are presented.

2.5 Simulation Results and Discussions

In order to evaluate the proposed fault location algorithm, we used EMTP-RV and MATLAB Wavelet Toolbox to carry out the transient simulations and post-fault analysis, respectively. The test case is a 170-kV, 60-Hz, hybrid seven-terminal transmission system. The transmission system consists of one overhead line and six submarine cables, as shown in Figure 5. The frequency-dependent line and cable models (EMTP FD and FDQ models)

are used for the overhead transmission line and cables. The lengths of the segments and traveling times are provided in Table 1. The sheaths of the cables are assumed to be fully cross-bonded and steel wire armour is continuously grounded [48]. Overhead line specifications are based on [49]. Two different cable types are used for submarine cables (i.e., Cable type 1 and 2 are based on Nexans, "TKRA 170 kV" and "A2XS(FL)2Y RM 87/150 170 kV", respectively [50]). Cable type 1 is used for Segments 2-J, 3-J, and 4-J, and cable type 2 is used for the Segments 5-J, 6-J, and 7-J. Transmission line transposition increases its attenuation constant [8] .Therefore, the traveling waves initiated by faults are more mitigated, and fault location becomes more challenging. Accordingly, we used a fully transposed overhead line in our simulation studies. In order to consider the effect of measurement uncertainties, zero-mean Gaussian noises with variances of $(V_p \times 0.01)$ are added to all transient voltage measurements, and V_p is the peak voltage of the system voltage [45]. Referring to Figure 2, the main grid and wind farms are simulated using voltage sources behind series impedances with the following resistance and inductance

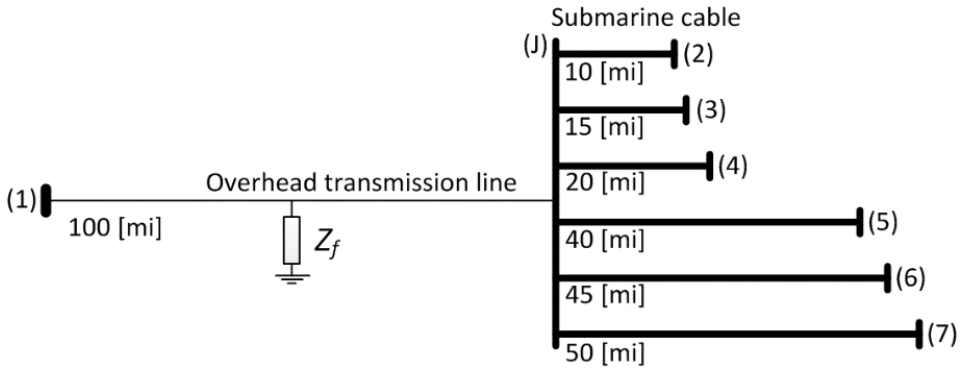

Figure 5. One-line diagram of the test case (seven-terminal hybrid system).

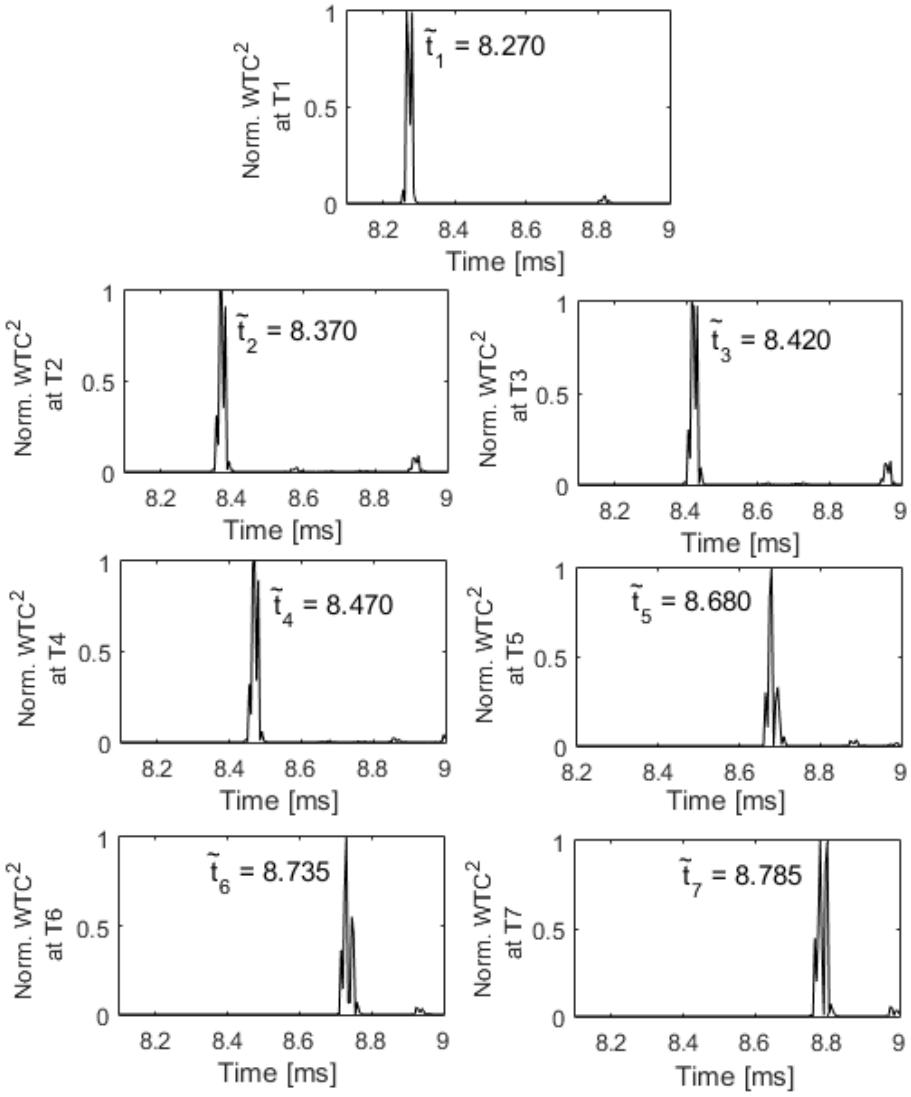

Figure 6. WTC²s of mode-1 voltages in scale-1, SLG fault in the overhead line at 50 mi from Terminal 1, $F_s = 200$ kHz, and $Z_f = 1\ \Omega$.

matrices:

$$R_m = \begin{bmatrix} 1.8 & 0.4 & 0.4 \\ 0.4 & 1.8 & 0.4 \\ 0.4 & 0.4 & 1.8 \end{bmatrix}, L_m = \begin{bmatrix} 0.0132 & 0.0053 & 0.0053 \\ 0.0053 & 0.0132 & 0.0053 \\ 0.0053 & 0.0053 & 0.0132 \end{bmatrix}$$

$$R_w = \begin{bmatrix} 2.5 & 0.8 & 0.8 \\ 0.8 & 2.5 & 0.8 \\ 0.8 & 0.8 & 2.5 \end{bmatrix}, L_w = \begin{bmatrix} 0.0185 & 0.0074 & 0.0074 \\ 0.0074 & 0.0185 & 0.0074 \\ 0.0074 & 0.0074 & 0.0185 \end{bmatrix}$$

where R_m [Ω] and L_m [H] are related to the main grid, R_w [Ω] and L_w [H] are related to the wind farms.

2.5.1 Illustrative Test Case

The steps of the proposed method for an SLG fault are provided in this section. The SLG fault is located in the middle of the overhead line (Segment 1-J) with the following conditions: $Z_f = 1\ \Omega$, which is the fault impedance, $FIA = 8^0$, and $F_S = 200$ kHz, which is the sampling frequency of the TRs. Figure 6 shows the normalized WTC^{2}s and the corresponding first arrival times based on steps 1 to 5. Table 1 provides wave traveling time differences ($\boldsymbol{\Delta\tau}$) and the measured arrival time differences ($\boldsymbol{\Delta\tilde{t}}$). The matrix $\boldsymbol{\Delta}$ is also provided in Table 1, and the six maximal values are located in the first row/column. Hence, $c^* = 1$, and therefore, Segment 1-J is identified as the faulty segment. According to (8) to (10), the below vectors are used to find the fault location in the identified faulty segment,

Table 1. Traveling times in different segments

Segment Lengths [mi] [1]	$L_{1\text{-}J}$ =100, $L_{2\text{-}J}$ =10, $L_{3\text{-}J}$ =15, $L_{4\text{-}J}$ =20, $L_{5\text{-}J}$ =40, $L_{6\text{-}J}$ =45, $L_{7\text{-}J}$ =50
Wave Traveling Times (τ) [μs] at 75 kHz [2]	$\tau_{1\text{-}J}$ = 550, $\tau_{2\text{-}J}$ = 105, $\tau_{3\text{-}J}$ = 155, $\tau_{4\text{-}J}$ = 205, $\tau_{5\text{-}J}$ = 410, $\tau_{6\text{-}J}$ = 460, $\tau_{7\text{-}J}$ = 510
$\boldsymbol{\Delta\tau} = \begin{bmatrix} 0 & 445 & 395 & 345 & 140 & 90 & 40 \\ -445 & 0 & -50 & -100 & -305 & -355 & -405 \\ -395 & 50 & 0 & -50 & -255 & -305 & -355 \\ -345 & 100 & 50 & 0 & -205 & -255 & -305 \\ -140 & 305 & 255 & 205 & 0 & -50 & -100 \\ -90 & 355 & 305 & 255 & 50 & 0 & -50 \\ -40 & 405 & 355 & 305 & 100 & 50 & 0 \end{bmatrix}$	
$\boldsymbol{\Delta\tilde{t}} = \begin{bmatrix} 0 & -100 & -150 & -200 & -410 & -465 & -515 \\ 100 & 0 & -50 & -100 & -310 & -365 & -415 \\ 150 & 50 & 0 & -50 & -260 & -315 & -365 \\ 200 & 100 & 50 & 0 & -210 & -265 & -315 \\ 410 & 310 & 260 & 210 & 0 & -55 & -105 \\ 465 & 365 & 315 & 265 & 55 & 0 & -50 \\ 515 & 415 & 365 & 315 & 105 & 50 & 0 \end{bmatrix}$	
$\boldsymbol{\Delta} = \begin{bmatrix} \mathbf{0} & \mathbf{545} & \mathbf{545} & \mathbf{545} & \mathbf{550} & \mathbf{555} & \mathbf{555} \\ \mathbf{545} & 0 & 0 & 0 & 5 & 10 & 10 \\ \mathbf{545} & 0 & 0 & 0 & 5 & 10 & 10 \\ \mathbf{545} & 0 & 0 & 0 & 5 & 10 & 10 \\ \mathbf{550} & 5 & 5 & 5 & 0 & 5 & 5 \\ \mathbf{555} & 10 & 10 & 10 & 5 & 0 & 0 \\ \mathbf{555} & 10 & 10 & 10 & 5 & 0 & 0 \end{bmatrix}$	

[1] L denotes segment length.

[2] As sampling frequency is 200 kHz, the measurement frequency contents are up to 100 kHz, and in wavelet scale-1, the frequency range from 50 to 100 kHz is considered. Therefore, wave traveling times at 75 kHz are utilized.

$\boldsymbol{\Delta\tilde{t}}^* = [100,150,200,410,465,515]^T$,

$\boldsymbol{\tau}^* = [550,550,550,550,550,550\ ]^T$,

$\boldsymbol{\tau} = [105,155,205,410,460,510]^T$, and

$\boldsymbol{b} = [555,555,555,550,545,545\ ]^T$.

The system voltage is 170 kV and noise variances in all the measurements are $170000 \times$

$\sqrt{2/3} \times 0.01$,therefore, $\boldsymbol{R} = \text{diag}(2800,2800,2800,2800,2800,2800)$ based on Appendix A. 2. The estimated λ is $\hat{\lambda} = 0.50075$ and the fault location is calculated using (11) as $EFD = 0.50075 \times 100 = 50.075$ mi. The fault location errors are finally calculated using [46]

$$err = \frac{|AFD - EFD|}{L} \times 100\% \tag{12}$$

where err is the fault location error, AFD [mi] is the actual fault distance, EFD [mi] is the estimated fault distance, and L is the faulty segment length [mi]. The error related to the illustrative case is $\frac{|50-50.075|}{100} \times 100 = 0.075\%$.

2.5.1.1 Sensitivity Assessment

In this section, the sensitivity of the proposed algorithm is evaluated for the following parameters: fault type, grounding system, FIA, optical transducer bandwidth, TR sampling frequency, fault resistance, non-ideal fault, and non-linear arc.

2.6 Fault Type and Grounding

In this dissertation, all five types of fault (i.e., single-line-to- ground (SLG), line-to-line (LL), line-to-line-to-ground (LLG), three-phase (3L), and three-phase-to-ground (3LG)) are studied. The magnitudes of the traveling waves increase for multiple-phase type of faults. Therefore, the signal-to-noise ratio (SNR) increases, and the fault initiated traveling waves are more detectable. Table 2 provides the average of the fault location errors for 1000 Monte Carlo simulations (MCSs) ($Z_f = 1\ \Omega$, $FIA = 8^0$, $F_S = 200$ kHz) at different locations. In each MCS, Gaussian random numbers are added to the simulated transient voltages to account for the measurement noises. As it is observed in Table 2, the proposed

method is not affected by the fault type since the traveling waves initiated by SLG faults are large enough to be detected.

Table 2. Relation between fault type and error

	Faulty Seg.	AFD [mi]	Fault Type				
			SLG	LL	LLG	3L	3LG
Error [%]	1-J	1	0.174	0.174	0.173	0.173	0.173
		50	0.080	0.080	0.080	0.079	0.080
		99	0.296	0.294	0.295	0.295	0.294
	2-J	1	3.010	3.010	3.012	2.998	2.998
		5	0.375	0.374	0.374	0.372	0.372
		9	8.174	8.174	8.175	8.167	8.167
	3-J	1	3.454	3.455	3.454	3.454	3.454
		7	0.146	0.146	0.146	0.143	0.144
		14	7.059	7.048	7.091	7.052	7.051
	4-J	1	2.687	2.692	2.698	2.688	2.689
		10	0.198	0.198	0.201	0.198	0.198
		19	5.375	5.374	5.376	5.366	5.366
	5-J	1	0.268	0.268	0.267	0.266	0.266
		20	0.013	0.012	0.012	0.011	0.011
		39	0.467	0.467	0.468	0.468	0.466
	6-J	1	0.335	0.334	0.334	0.332	0.332
		22	0.012	0.012	0.012	0.011	0.011
		44	0.499	0.504	0.505	0.488	0.487
	7-J	1	0.272	0.273	0.273	0.272	0.272
		25	0.017	0.015	0.016	0.014	0.014
		49	0.406	0.404	0.407	0.405	0.404

The effect of grounding system is also studied in this dissertation. Although the fault currents are smaller in ungrounded systems compared to that in grounded systems, the voltages are more distorted in ungrounded systems, as shown in Figure 7 (SLG fault in the middle of Segment 2-J, $Z_f = 1\ \Omega$, and $FIA = 8^0$). Therefore, the traveling wave magnitudes are larger and more detectable. As the proposed method is less efficient in grounded systems, the studies are limited to grounded systems.

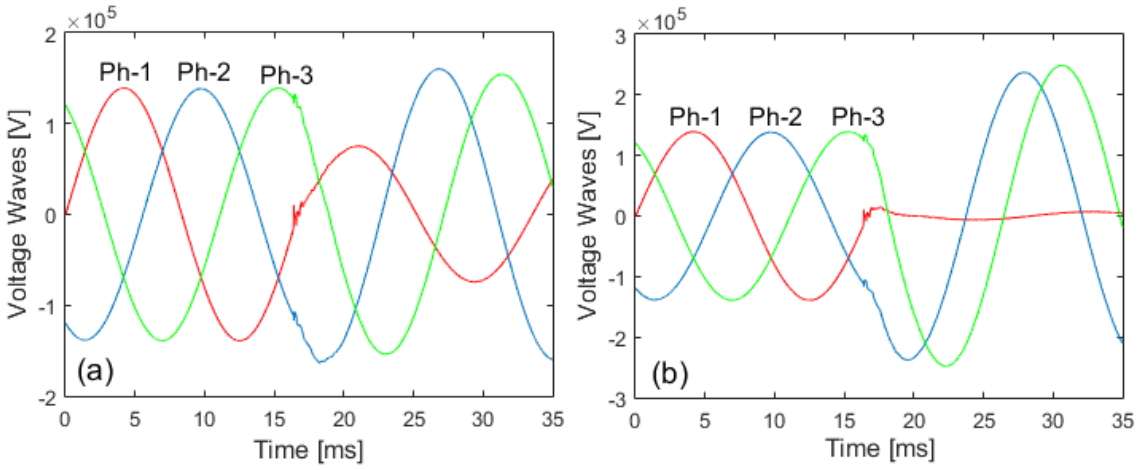

Figure 7. Three phase voltages at Terminal 2 (SLG fault in the middle of Segment 2-J, $Z_f = 1\ \Omega$, $FIA = 8^0$). (a) Grounded system. (b) Ungrounded system.

2.6.1 Fault Inception Angle (FIA)

FIA affects the severity of the traveling waves initiated by a fault. As the FIA of a fault decreases, SNRs of the arriving waves decrease. Thus, detection of the traveling waves, and estimation of the fault location become more challenging. This concept is shown in Appendix A. 3. Table 3 shows the effect of FIA on the proposed method. As the closest locations to the terminals and joint point are the most challenging locations for the proposed method, SLG faults with different FIAs at those places are studied and the results are given in Table 3. The location of the faults with the minimum FIA of 8^0 are estimated by the proposed method ($Z_f = 1\ \Omega$, $F_S = 200$ kHz). However, the location of the faults with smaller FIAs can be estimated for segments with lesser attenuation factors (i.e., attenuation factor equals $e^{-\alpha l}$, where α is attenuation constant, l is segment length [mi], [51]) or in less noisy situations.

Table 3. Effect of FIA

Faulty Segment	AFD [mi]	FIA [^{0}]			
		5	6	7	8
1-J	1	N/A	N/A	✓	✓
	99	N/A	N/A	N/A	✓
2-J	1	N/A	✓	✓	✓
	9	N/A	✓	✓	✓
3-J	1	N/A	✓	✓	✓
	14	N/A	✓	✓	✓
4-J	1	N/A	✓	✓	✓
	19	N/A	N/A	✓	✓
5-J	1	N/A	✓	✓	✓
	39	N/A	N/A	✓	✓
6-J	1	N/A	N/A	✓	✓
	44	N/A	N/A	✓	✓
7-J	1	N/A	N/A	✓	✓
	49	N/A	N/A	N/A	✓

N/A shows that the proposed method is not applicable.
✓ shows that the proposed method is applicable.

2.6.2 Measuring Device Characteristics

An optical voltage transducer has a limited bandwidth. According to the Nyquist-Shannon's sampling theorem, frequency contents up to half of the sampling frequency of TRs can be measured. Hence, transducers together with TRs filter out high frequency contents of the transient voltages, and thus, the sharpness and magnitudes of the measured arriving waves reduce. Consequently, they become less detectable by DWT. Furthermore, as sampling frequency decreases, the proposed method resolution decreases [52]. Table 4 shows the relation between the sampling frequency and the proposed algorithm accuracy for SLG faults at the given locations ($Z_f = 1\ \Omega$, $FIA = 8^0$). It is noted that the accuracy of the proposed method increases as sampling frequency increases. On the other hand, the attenuation constants of the line and cables increase for higher frequencies of traveling waves. Therefore, the higher frequencies of traveling waves mitigate more and the

traveling waves received at the terminals fade in the noise.

Figure 8 shows normalized WTC[2]s related to the arriving waves induced by a fault identical to that in the illustrative test case. However, the sampling frequency is 500 kHz. It is observed that the arriving waves are well-distinguishable from the noise in Segment 1-J whose attenuation factor is 0.6274 at 187.5 kHz (for 50 mi, $\alpha = 0.009323$). Cable type 1 is used for Segments 2-J, 3-J, and 4-J and their attenuation factors are: 0.4365, 0.2885, and 0.1906 at 187.5 kHz, respectively ($\alpha = 0.082897$). Therefore, the arriving waves are still distinguishable from the noise as shown in Figure 8. Cable type 2 is used for Segments 5-J, 6-J, and 7-J and their attenuation factors are: 2.8833×10^{-4}, 1.0403×10^{-4}, and 3.7537×10^{-5} at 187.5 kHz ($\alpha = 0.203785$), respectively. Therefore, arriving waves mitigate more, and consequently, the traveling waves disappear in the noise. Thus, the attenuation factors limit the highest applicable sampling frequency. However, higher sampling frequencies can be utilized in a less noisy situation, with higher DWT scales such as scale 2, or using the suggestions in [53] and [54] for reducing the noise effects.

Table 4. Relation between the Sampling Frequency and Errors

Faulty Seg.	AFD [mi]	F_S [kHz]	Error [%]	Faulty Seg.	AFD [mi]	F_S [kHz]	Error [%]
1-J	50	100	0.74	5-J	20	100	1.03
		200	0.08			200	0.01
2-J	5	100	2.38	6-J	22	100	0.95
		200	0.37			200	0.01
3-J	7	100	0.43	7-J	25	100	0.73
		200	0.14			200	0.01
4-J	10	100	2.44				
		200	0.19				

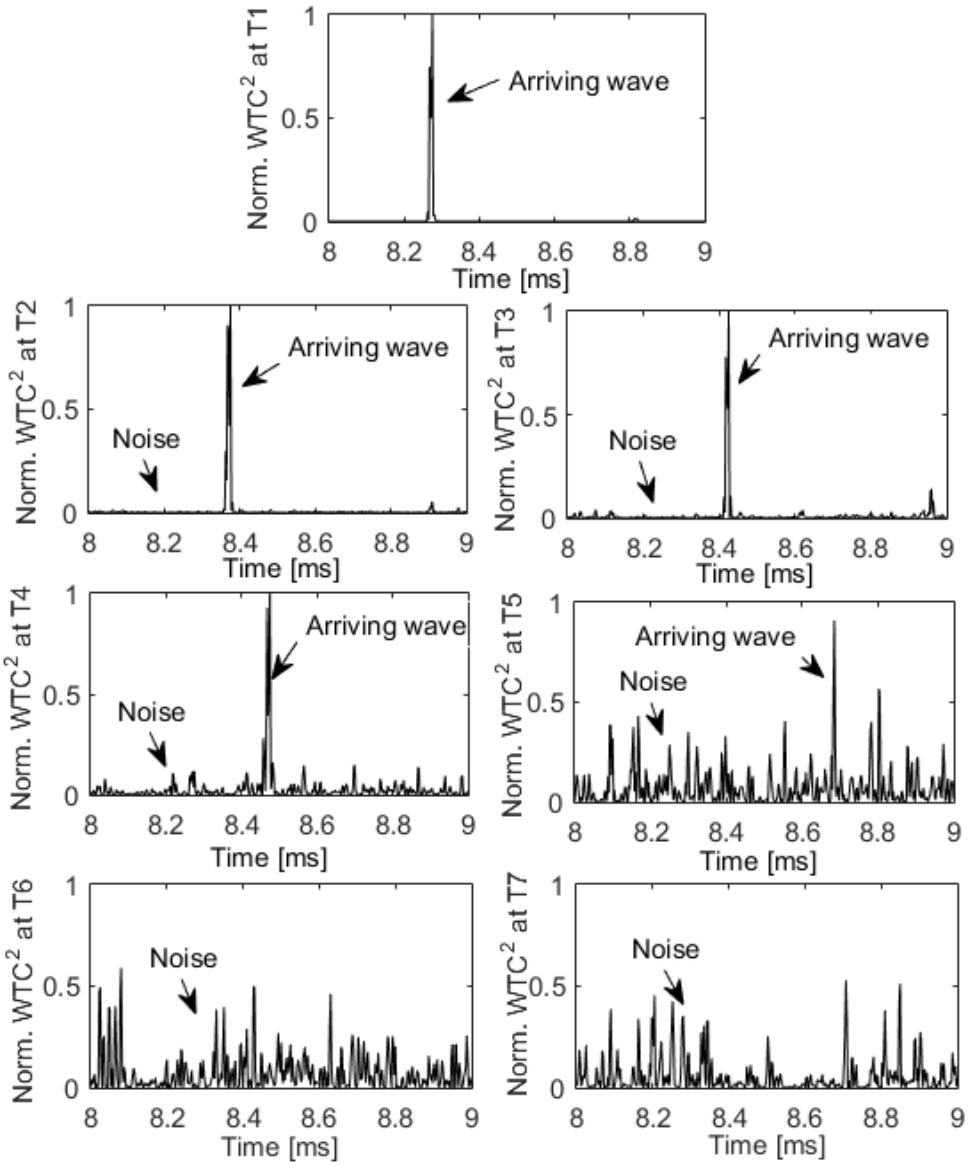

Figure 8. Noise and arriving waves for a fault in the middle of Segment 1-J ($F_s = 500$ kHz, $Z_f = 1\ \Omega$, FIA=8^0). The arriving waves at Terminals 1 to 4 are distinguishable from noise. However, the arriving waves at Terminals 5 to 7 disappears in the noise because of the larger attenuation factors of Segments 5-J, 6-J and 7-J.

2.6.3 Fault Resistance

The proposed method is evaluated for a range of fault resistances. As the fault resistance increases, the magnitudes of the fault initiated traveling waves decrease. Therefore, the traveling waves are prone to vanish because of attenuation factors and noises. The proposed method is able to estimate the location of a fault with a resistance up to 150 Ω ($FIA = 8^0$,

and $F_S = 200$ kHz).

2.6.4 Non-Ideal Faults

In this section, the effect of fault impedance (Z_f in Figure 5) on the proposed method performance is studied. As a common practice, a resistive Z_f is considered in the literature. However, when a fault occurs between phases and ground wires or towers, the inductive part of Z_f becomes larger [55] and [56]. Figure 9 shows the effect of inductive fault impedances on traveling wave shapes. Total fault impedance is constant in all the cases, however, the X/R ratio varies ($Z_f = R + jX_L = 10\ \Omega$). The fault impedances with larger X/R ratios generate traveling waves with smooth shapes. Consequently, the detectability of traveling waves degrades. Our simulation studies indicate that faults with $X/R \leq 71$, which corresponds to $L/R \leq 0.19$ H/Ω, and $FIA \geq 8^0$ enable traveling waves to be detectable using DWT with db-4 mother wavelets and $F_s = 200$ kHz. As stated in [55] and [56], the inductive part of a fault impedance is usually small compared to its resistance. Hence, the proposed method is not affected by usual inductive faults in power systems. As for R-C fault impedances, the capacitive part does not make the traveling wave smooth. Therefore, R-C faults do not affect the proposed method performance.

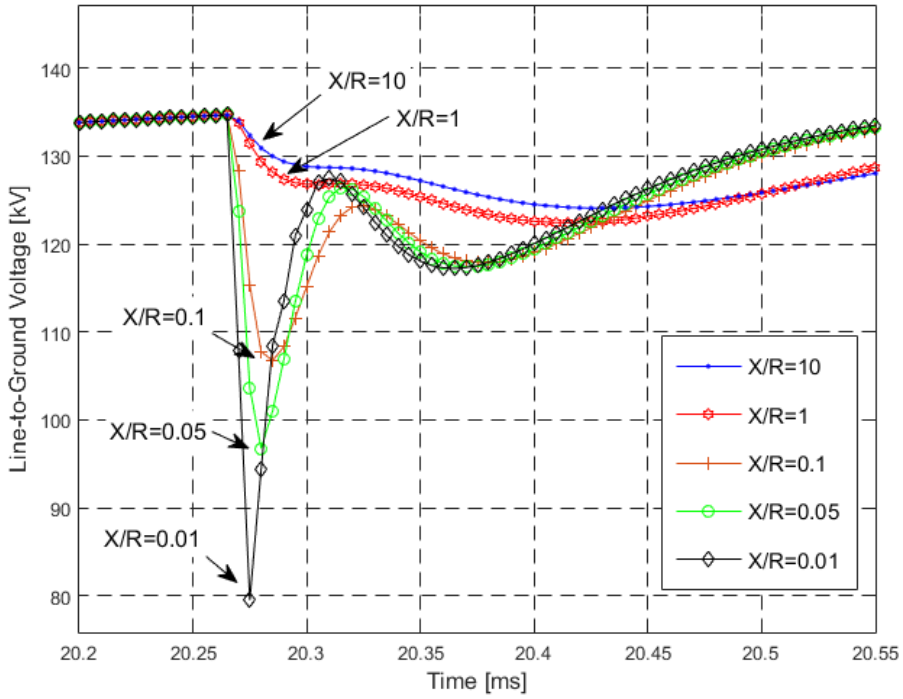

Figure 9. The mode-1 voltages at the overhead line terminal for faults in the middle of the overhead line, $Z_f = R + jX_L = 10\ \Omega$ and *X/R* ratio is variant.

2.6.5 Non-Linear Arc

The proposed algorithm is evaluated for long non-linear arcs that can occur in the overhead segment. A long arc is a non-linear fault influenced by a number of factors (e.g., the convection of the air and plasma, wind speed, pressure, and humidity) [57]. An arc in the air has two main stages:

- The first stage is the arc leader propagation in which the air gap breaks down and provides an ionized hot plasma channel [57] and [58]. The arc leader propagation for string insulator or rod-plane is modeled as [57]

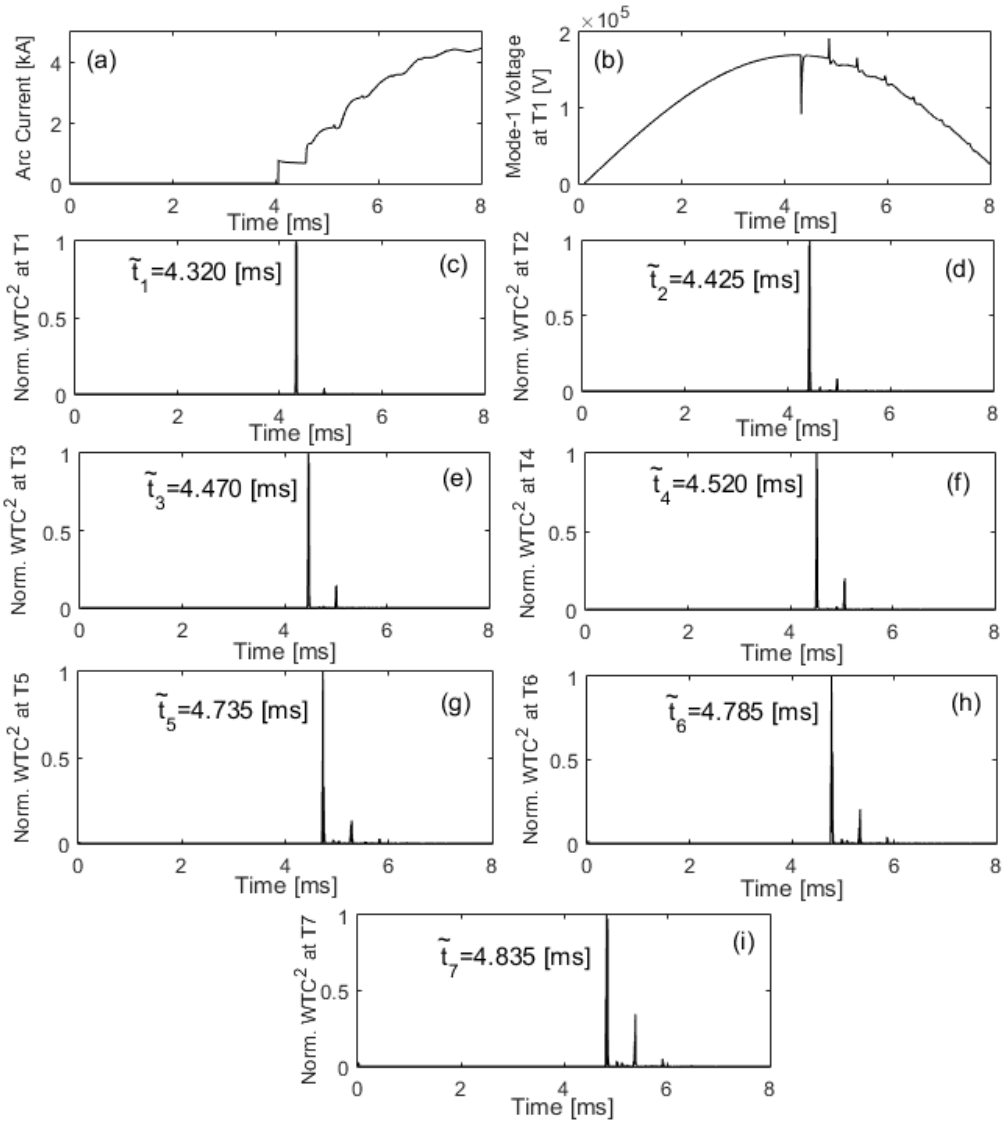

Figure 10. The effects of arc leader propagation and long arc on the proposed method (fault in the overhead line at 50 mi from Terminal 1, $F_S = 200$ kHz). (a) The current through arc channel. (b) The mode-1 voltage at Terminal 1. (c)-(i) Normalized WTC^{2}s at Terminals 1 to 7.

$$\begin{cases} v = k_1 \dfrac{V^2}{(D-x)} + k_2 \dfrac{Vi}{(D-x)} \left(\dfrac{x}{D}\right) \\ i = C_1.V.v \end{cases} \tag{13}$$

where v is the arc leader propagation velocity [m/s], V [V] is the voltage across the air gap, i is the pre-discharge current [A], D and x [m] are the gap and leader lengths, respectively, and $C_1 = 5 \times 10^{-10}$ F/m according to [57]. We assume D is 0.3 m. The following

parameters are utilized for simulations mostly based on [59]: $V = V_p \sin(2\pi \times 60 \times t)$, $V_p = 138.8$ kV that equals to 170 kV (LL-RMS), $k_1 = 2 \times 10^{-7}$ and $k_2 = 3 \times 10^{-3}$ for both positive and negative leaders.

- The second stage considers the dynamic behavior of an established long arc in which the arc resistance is non-linear and time-variant. Long arcs are modeled as [60]

$$\begin{cases} R_{arc} = 1/g \\ dg/dt = 1/\tau\ (G - g) \\ G = |i_{arc}|/V_{st} \end{cases} \tag{14}$$

where R_{arc} [Ω] is the time-varying arc resistance, g [S] is the time-varying arc conductance, i_{arc} [kA] is the arc current, G [S] is the stationary arc conductance, τ [s] is the arc time constant, and V_{st} [kV] is the stationary arc voltage, defined as

$$V_{st} = (u_0 + r.|i_{arc}|) \times l \tag{15}$$

where u_0 [V/cm] is the constant voltage per arc length, r [m Ω/cm] is the arc resistance per length, and l [cm] is the arc length. The following parameters are utilized for the simulation study: $\tau = 10^{-3}$ s, $u_0 = 12$ V/cm, $r = 2$ mΩ/cm, and $l = 40$ cm.

Similar to the illustrative test case, the arc fault is located at 50 mi from Terminal 1 and $F_S = 200$ kHz. The fault current through the arc is shown in Figure 10(a) to demonstrate the arc leader behavior. As it is observed, there is a sharp increase in the arc current during the first stage that generates large and sharp traveling waves. Figure 10(b) shows the mode-1 voltage at Terminal 1 in which a sharp change in the voltage waveform is observed due to the fault induced traveling waves. Figure 10(c)-(i) show the resulting WTC^{2}s and their corresponding arrival times. The estimated fault location error is 0.08%. Thus, considering the second row of Table 2, the proposed method accuracy does not deviate for non-linear

arcs since they generate sharp large-amplitude traveling waves.

2.6.6 Error Assessment

One thousand MCSs for SLG faults ($Z_f = 1\ \Omega$, $FIA = 8^0$, and $F_S = 200$ kHz) at every mile along the segments are carried out. A small portion of the faults are not correctly identified due to the measurement uncertainties. The unsuccessful fault locations in the case studies are as follows:

a) For faults at 99, 98, 97, and 96 mi from Terminal 1, the faulty segment is not correctly identified in 78, 58, 29, 8% of MCSs, respectively. b) For the faults at 44 mi from Terminal 6, 9% of the faults are not correctly identified. c) For the faults at 49 and 48 mi from Terminal 7, 16 and 8% of the faults are not correctly identified. For the other locations, the faults are identified in all Monte Carlo case studies.

Figure 11 shows the average of the fault location errors in the logarithmic plane for all segments. A common trend is observed in all the segments, that is, the fault location errors decrease for the faults in the middle of the segments. Additionally, the faults close to the terminals and joint point lead to higher fault location errors. Furthermore, the faults close to the joint point result in higher errors compared to the faults near the terminals in accordance with [43]-[45]. The fault location errors in the cables are larger compared to the errors in the overhead line since (12) is used for calculation of the errors and the shorter lengths of the cables lead to larger errors. The average errors related to the Segments 2-J, 3-J, and 4-J are larger compared to the errors in the literature because the lengths of these segments are shorter than the lengths in the literature [43]-[45] and [61].

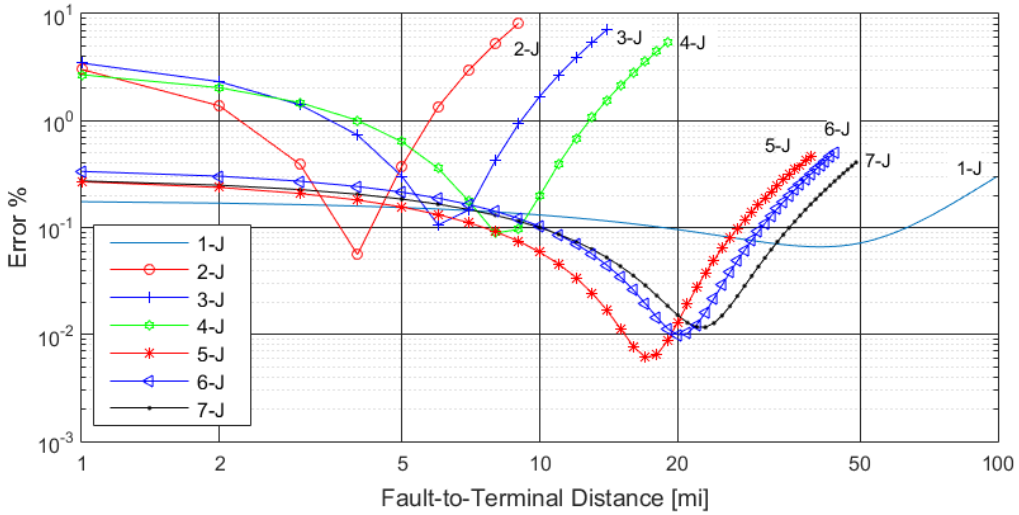

Figure 11. Fault location errors along the segments, $Z_f = 1\ \Omega$, $FIA = 8^0$, $F_S = 200$ kHz.

2.6.7 Cable Aging

The inductance of a cable increases with cable aging. Therefore, traveling wave velocity decreases, and consequently, wave traveling time increases [62]. As the proposed method is based on a priori known wave traveling times, its accuracy degrades with cable aging. This shortcoming can be addressed by introducing a correction factor, which translates the changes in cable parameters to a change in traveling wave velocity. The correction factor can be determined by carrying out site tests in certain time intervals or by employing a parameter estimation tool.

2.7 Comparison

The accuracy and requirements of the proposed method are compared with the existing methods in the literature. The average errors are calculated and presented in Table 5 for providing an insight into the accuracy of other methods. As it is observed from Table 5, traveling wave-based fault location methods are more accurate compared to power frequency-based (i.e., impedance-based) methods. It is also observed that the proposed method has less error compared to the existing methods, however, it requires synchronized

transient recorders at all terminals which can be economically justified for important transmission systems such as offshore wind power interconnection.

Table 5. Comparison of the Fault Location Methods

System Topology	S/A[1]	P/T [2]	Error Ave. [%]	Noise	Number of Meas.	Ref.
UC [3] 1-Segment	-	P	2.74	No	1	[34]
UC 1-Segment	-	P	1.73	No	1	[35]
UC 1-Segment	-	T	1.132	Yes	1	[63]
UC 2-Segment	S	T	0.43	No	3	[64]
Hybrid 2-Segment	-	T	0.81	Yes	1	[45]
Hybrid 2-Segment	S	T	0.3	Real [4]	2	[65]
Hybrid 3-Terminal	S	T	1.37	No	3	[48]
Hybrid 7-Terminal	S	T	0.36	Yes	7	Proposed Method

[1] S/A indicates synchronous or asynchronous measurements.
[2] P/T indicates power frequency-based or traveling wave-based fault location methods.
[3] UC indicates underground cable.
[4] Only one real experience is reported.

2.8 Conclusion

This chapter proposes a traveling wave-based fault location algorithm for hybrid multi-terminal transmission systems consisting of one overhead line and multiple submarine cables. Hybrid transmission systems are common for interconnection of offshore wind farms to the main grid. The proposed algorithm uses synchronized transient voltage measurements at all ending terminals. The measurements are provided using optical voltage transducers equipped with GPS signal receivers. The mode-1 voltages at all terminals are calculated using the Clarke's transformation. Discrete wavelet transformation (DWT) is then applied to the calculated mode-1 voltages to obtain the time-frequency

components. The squares of wavelet transformation coefficients (WTC^2s) of mode-1 voltages are observed to detect the arrival times at the terminals. The proposed faulty segment identification algorithm and fault location formulation are based on the differences among the first arrival times at all terminals. The effectiveness of the proposed method is evaluated through simulation results of a hybrid seven-terminal transmission system. The transient simulations and the post fault analysis are carried out using EMTP-RV and MATLAB Wavelet Toolbox, respectively. The performance of the proposed algorithm is studied for the following conditions: fault type, grounding system, fault inception angle (FIA), transducer bandwidth, measurement device sampling frequency, fault resistance, non-ideal fault, and non-linear arc. According to the simulation results, the proposed method is able to identify the faulty segment and estimate the fault location. However, its performance reduces in the case of the faults close to the joint point and ending terminals.

Chapter 3. Adaptive Single-Phase Auto-Reclosing Method using Power Line Carrier Signals[3]

In this chapter, a new method for adaptive single-phase auto-reclosing (ASPAR) is proposed for enhancing successful auto-reclosing in transmission systems. In single-phase reclosing, after occurrence of a fault, only the faulty phase is disconnected by the protection system (e.g., distance relays and circuit breakers). The proposed method utilizes power line carrier (PLC) signals for determination of the secondary arc extinction time. Despite the increasing application of modern communication systems (e.g., fiber-optic links), PLC systems are still widely used, cost-effective, and reliable. Therefore, the proposed method provides an ancillary application for PLC systems in order to improve the power system resiliency and stability. The simulation studies are carried out using EMTP-RV and MATLAB, and the pros and cons of the proposed method are presented and compared to the existing ASPAR methods.

3.1 Introduction

A large number of faults in power transmission systems are transient [66] and [67], and auto-reclosing (AR) is an efficient approach to clearing such faults and avoiding long-time outages. As most of the faults in transmission lines are single-line-to-ground (SLG), single-phase auto-reclosing (SPAR) is developed for disconnection and reconnection of the only faulty phase [66]-[71]. Therefore, SPAR improves power system transient stability and reliability [69]-[75], as the non-faulty phases can be still used for power transmission in a grid. SPAR also decreases switching over voltages and generator shaft oscillations [66],

[3] Reprinted in line with copyright and author-rights for "Adaptive auto-reclosing using power line carrier signals," [Submitted] by R. Jalilzadeh Hamidi and H. Livani, Elsevier IJEPES.

[69]-[74]. In the traditional AR and SPAR, the tripped circuit breaker (CB) stays open for a fixed and predefined dead time for the arc to be extinguished [67]-[73]. However, arcs have a non-linear nature influenced by a number of random factors such as convection of the plasma and the surrounding air, the wind, humidity, and atmospheric pressure [76] and [77]. Thus, arc lifetimes arbitrarily vary, and consequently, the following issues arise from the fixed-time (conventional) auto-reclosing: 1) if the fault is permanent, reclosing actions put more stress on the power system components and decrease power system stability [78]. 2) In the case of a transient fault with a lifetime longer than the predefined dead time, reclosing actions re-energize the arc. Therefore, in addition to imposing more stress on power system equipment, it is probable that the transient fault becomes permanent [69], [73], and [78]. 3) If the fault arc extinguishes before the predefined dead time, the power system profits less from AR. Accordingly, the ideal time for a CB to reclose is the time immediately after the arc extinction [69]. Therefore, adaptive single-phase auto-reclosing (ASPAR) is introduced in the literature for accurate determination of the arc extinction time to reclose the CBs. According to the required data for determination of the secondary arc extinction, ASPAR can be broadly divided into: 1) non-communication-based (single-ended) ASPAR that requires only the data from the local bus. 2) Communication-based (double-ended) ASPAR that requires the data from both local and remote buses.

Several methods for single-ended ASPAR are introduced in the literature. In [68], the proposed single-ended ASPAR relies on the waveform pattern of the local bus voltage after disconnection of CBs. The RMS value of the faulty-phase voltage is calculated, and it becomes relatively large once the secondary arc extinguishes. However, this method is relatively slow mainly due to the required time for calculation of the full-cycle RMS value.

In [69], the proposed single-ended ASPAR utilizes the adaptive cumulative summation method (ACUSUM) to detect the secondary arc extinction. In [73], a single-ended ASPAR is proposed that employs the voltage phasor of the faulty phase to distinguish between permanent and transient faults and also to detect the arc extinction time. In [78], a method is proposed based on the voltage measurement at the local bus. The total harmonic distortion (THD) of the measured voltage is calculated using discrete Fourier transformation (DFT) and the arc extinction time is detected according to the calculated THD level. In [79], a single-ended ASPAR is proposed that calculates the post-fault zero-sequence voltage of the local bus. Then, the third harmonic level in the zero-sequence voltage is utilized for detection of the arc extinction. In [80], a single-ended ASPAR is proposed, in which the currents of the non-faulty phases are measured at a fixed sampling rate of 10 kHz, and then using wavelet packet decomposition (WPD), the absolute values of the calculated wavelet nodes are added and used as an index for distinction of permanent and transient faults and for identification of the arc extinction as well. In [81], the proposed single-ended ASPAR discriminates transient and permanent faults by comparing the voltage pattern of the faulty and non-faulty phases in a complex plane. A single-ended ASPAR based on numerical spectral domain is proposed in [82], which discriminates transient and permanent faults and also estimates the fault distance. This method utilizes the fundamental and third harmonic contents of the local voltage and current measurements to distinguish between the transient and permanent faults. However, it is not capable of detecting the arc extinction time. In [83], a single-ended ASPAR is proposed in which the frequency contents of the measured voltages at the local bus are analysed using discrete wavelet transform (DWT) with Daubechies mother wavelet. Then, the secondary arc

extinction is detected based on the levels of certain frequencies. In [84], a single-ended ASPAR is introduced that uses the local voltage of the faulty phase. It distinguishes between permanent and transient faults and estimates the arc extinction time using the adaptive linear neuron (ADALINE) method. Another single-ended ASPAR is proposed in [85], which is able to distinguish between permanent and transient faults under different fault types, including ground faults, cross-line faults, and interphase faults. This method is based on the summation of the faulty-phase recovery voltage with respect to time. The summation is almost zero for permanent faults, while it is large for transient faults. However, the method is not able to detect the arc extinction time.

With respect to double-ended ASPAR, several methods have been proposed in the literature. The proposed double-ended ASPAR in [86] is based on synchronized current and voltage measurements at both ends of the line. The time-synchronized measurements are converted to spectral domain using DFT. Then, permanent and transient faults are distinguished and the arc extinction time is determined based on the harmonic level in the frequency spectrum. This method is able to determine the arc resistance as well. However, this method requires a capable communication link for data transfer and the algorithm is only proper for single circuit lines. The double-ended ASPAR in [87] utilizes the voltage and current phasors provided by synchronized phasor measurement units (PMUs) at both ends of the line. Then, THD is calculated and used as an index for distinguishing permanent faults from transient faults. In [88], a double-ended ASPAR is proposed for only transposed transmission lines. This method predicts the faulty-phase voltage using the non-faulty phase voltages measured by PMUs. Once the voltage phasor of the faulty phase is close to the predicted value, the arc extinction is determined. In [89], an ASPAR method is

proposed in which Prony analysis is utilized to extract the features of the voltage measurements during a fault. Then, the transient and permanent faults are discriminated using the extracted features and artificial neural network (ANN). However, the proposed method requires extensive off-line simulations for training the ANN-based decision-making process.

The applications of power line carriers (PLCs) in fault location and health monitoring in transmission lines are introduced in [8] and [91]. In this dissertation, the application of power line carriers (PLCs) in the detection of the secondary arc extinction is proposed for the first time and a new double-ended ASPAR method based on PLC signals is proposed to detect the secondary arc extinction time and to prevent unsuccessful reclosing of CBs. Therefore, it improves the overall power quality and system reliability. The proposed method does not require high computational capabilities, and it can be implemented using commercial micro-controllers. As PLC systems are widely used all over the world [92], the proposed method can be considered as an auxiliary application of PLC systems. The efficiency of the proposed method is evaluated using simulation results. It is shown that the proposed ASPAR is not influenced by fault location, faulty phase, system loading, transmission line transposition, shunt reactors, PLC carrier frequency. Also, it has a proper resiliency with respect to the measurement noise.

3.2 Technical Background and Methodology

In this section, the technical features of PLC systems and arc stages are briefly discussed, and the proposed ASPAR method is then described through an illustrative example.

3.2.1 Power Line Carriers

PLC systems are widely used for communication between substations over transmission lines. They usually generate carrier frequencies in the range of 30 to 500 kHz [93], however, 10 kHz is mentioned as the lowest PLC carrier frequency in [94]. This frequency range is sufficiently high to be isolated from the power frequency and power system noises [95]. A PLC system is coupled to a transmission line as shown in Figure 12. The coupling circuit (i.e., the coupling capacitor and drain coil) provides low- and high-impedance paths for the PLC carrier and power frequencies, respectively.

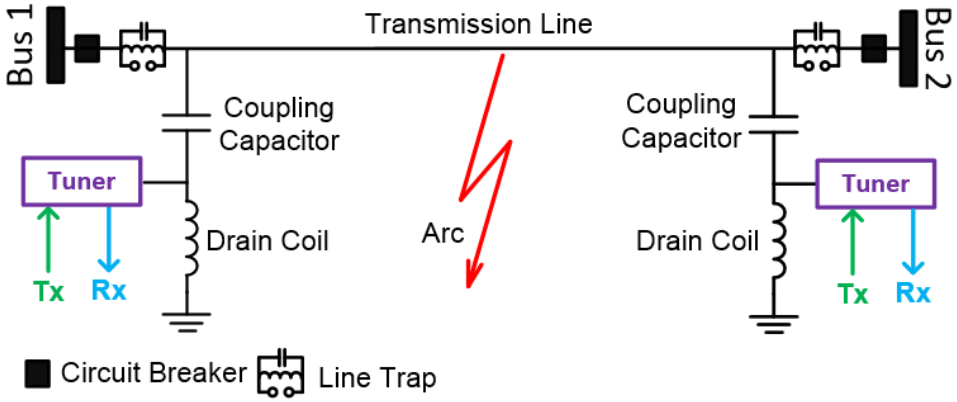

Figure 12. Schematic of PLC coupling.

3.2.2 Transient Faults and Secondary Arcs

An arc fault consists of two main stages: 1) before CBs disconnect the faulty phase, the arc is fed by the energy source. This high current arc is called a primary arc. 2) After disconnection of the faulty phase, a relatively low amplitude current still flows to the earth through the arc channel which is fed by the trapped charge and the mutual inductance and capacitance among the faulty phase and the un-faulty phases. This low current arc is called a secondary arc, and it sustains for a relatively short period of time. However, the CBs must

stay open until the secondary arc is fully extinguished [67]-[76]. The dynamic behaviour of arcs is modelled as [54], [97]

$$\begin{cases} R_{arc} = 1/g \\ dg/dt = 1/\tau\ (G - g) \\ G = \dfrac{|i_{arc}|}{V_{st}} \\ \tau = \tau_0 \left(\dfrac{l_{arc}}{l_0}\right)^{\alpha} \end{cases} \tag{16}$$

where R_{arc} [Ω] is the time-varying arc resistance, g [S] is the time-varying arc conductance, G [S] is the stationary arc conductance, i_{arc} [kA] is the arc current, τ [s] is the variant arc time constant, τ_0 [s] is the initial arc time constant, α is the negative exponent of the time constant [97] which is in the range of -0.1 to -0.6 [96], l_0 [cm] is the initial arc length, and l_{arc} is the instantaneous arc length [96]. V_{st} [kV] is the stationary arc voltage, defined as

$$V_{st} = (u_0 + r.|i_{arc}|) \times l_0 \tag{17}$$

where u_0 [V/cm] is the constant voltage per arc length and r [m Ω/cm] is the arc resistance per length.

3.3 Proposed ASPAR Method

Referring to Figure 12, the faulty-phase voltage at Bus 2 from inception to extinction of a transient SLG arc is shown in Figure 13(a). At $t = 40$ ms, the primary arc establishes, and then the fault-induced traveling waves reach Bus 2 as shown with P1 in Figure 13(a). Assume that after three power cycles (48 ms), at $t = 88$ ms, the protective relays (e.g., distance protection) along with the CBs disconnect the faulty phase as shown with P2 in Figure 13(a). As the faulty phase is no longer connected to the system, the secondary arc starts from P2 and extinguishes at P3. Figure 13(b) shows the arc resistance during the

fault. The primary arc resistance is between P1 and P2 and the secondary arc resistance is between P2 and P3, which resonates at a frequency of 120 Hz, two times the power frequency (60 Hz) since the arc plasma is reignited at each half power cycle [76], [77], and [98].

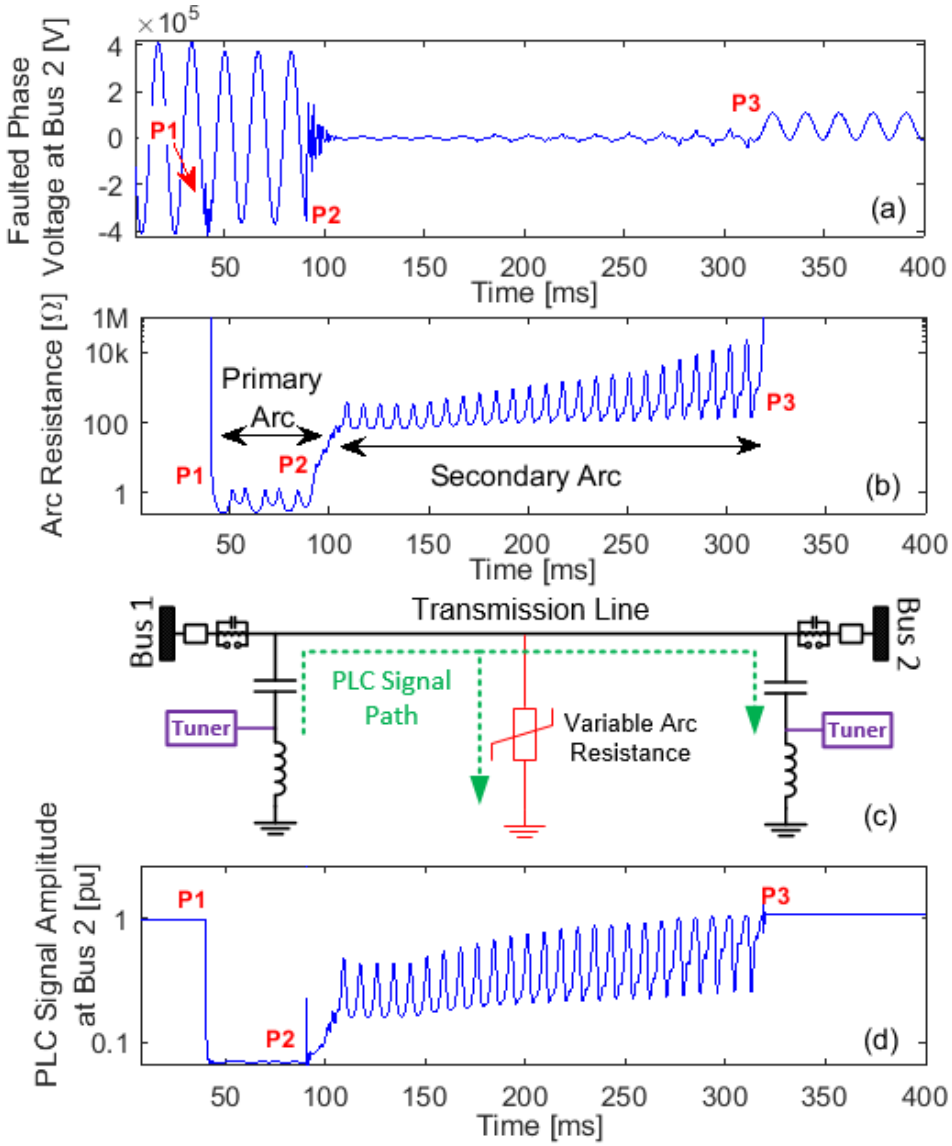

Figure 13. The sequence of the events during the arc lifetime. (a) Typical voltage of a faulty phase. (b) Dynamic arc resistance. (c) The path that PLC signals pass through. (d) Typical PLC signal amplitude. P1 shows fault inception. P2 shows de-energization of the faulty phase by the protection system (e.g., distance relays along with CBs). P3 indicates the secondary arc extinction.

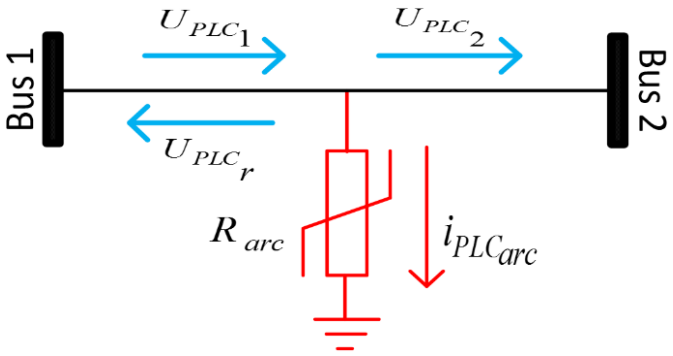

Figure 14. The PLC signal traveling waves at the fault location.

Figure 13(c) shows that the PLC carrier signal divides into two portions at the arc location. Referring to Figure 14, the PLC signal amplitude at the fault location is formulated as (18) and the detailed formulation is provided in Appendix B.

$$U_{PLC_2} = U_{PLC_1} \frac{2R_{arc}}{2R_{arc} + Z_C} \tag{18}$$

where U_{PLC_1} and U_{PLC_2} are the forward PLC signal waves before and after the fault location, Z_C is the characteristic impedance of the line at the PLC signal frequency, R_{arc} is the arc resistance. Based on (18), the PLC signal amplitude reaching the other end is related to arc resistance as $R_{arc} \to 0$, then $U_{PLC_2} \to 0$, therefore, the other end does not receive the PLC signal. When $R_{arc} \to \infty$, then $U_{PLC_2} \to U_{PLC_1}$, therefore, the PLC signal is not mitigated at the fault location, where '→' indicates that the left side approaches the right side. The received PLC signal at Bus 2 varies with the frequency twice the main power frequency, in step with the secondary arc resistance variations, as shown in Figure 13(d). As it can be seen in Figure 13(a), a considerable distortion occurs after disconnection of CBs. The distortion consists of a wide range of frequencies, including the PLC carrier frequency. Therefore, a relatively large rise exists in the received PLC signal at Bus 2 close to P2 in Figure 13(d). As the waveform pattern changes at the secondary arc extinction time (P3),

a range of frequencies as well as the PLC carrier frequency, are provided. Thus, a distortion adjacent to P3 exists in Figure 13(d). However, it is obvious in Figure 13(d) that the PLC signal amplitude continuously returns to its normal value after the extinction of the secondary arc.

Figure 15(a) shows the PLC signal amplitude at Bus 2 for several milliseconds before arc extinction. A threshold, 95% of the normal PLC signal amplitude, is considered. Once the measured PLC signal at Bus 2 becomes equal to or greater than the threshold, a timer starts, and when the PLC signal magnitude becomes less than the threshold, the timer stops and resets, as shown in Figure 15(b). The timer is able to count for half of a power cycle only if the secondary arc is extinguished, and then a reclosing command is released after a time margin, as shown in Figure 15(c).

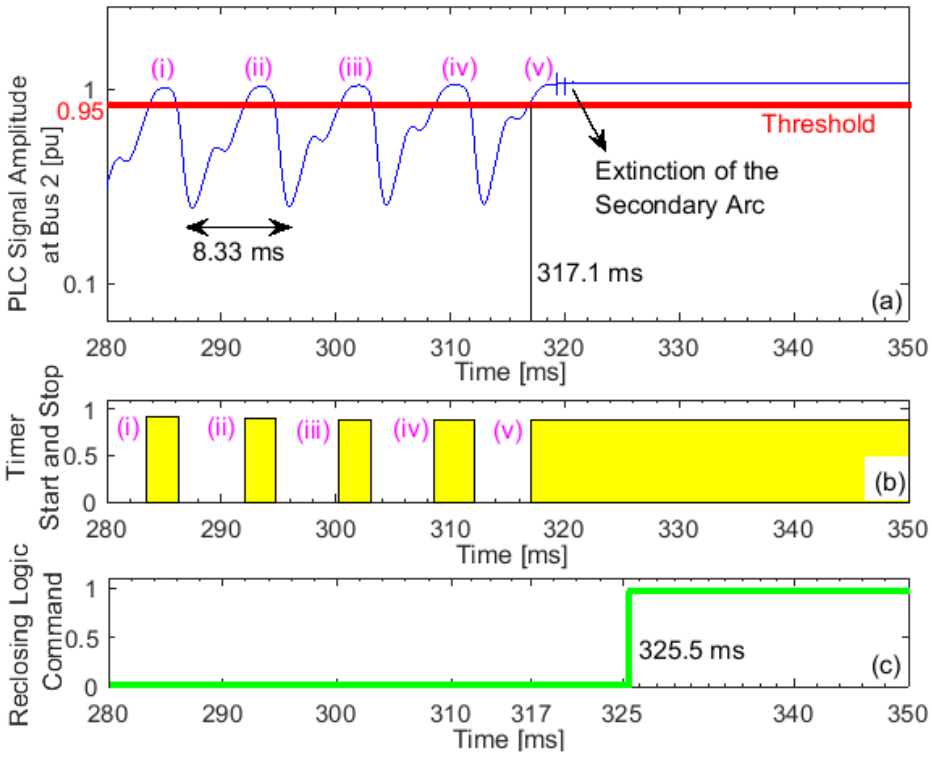

Figure 15. (a) The PLC signal amplitude in a short span before arc extinction. (b) Timer operations. (c) Reclosing command.

Table 6 presents the measured times corresponding to the PLC signal peaks shown in Figure 15(a). It is noticed that the timer starts and stops twice each power cycle during the secondary arc lifetime. Referring to Figure 15(b), at $t = 317.1$ ms, the timer starts since the PLC signal passes the threshold, and as the PLC signal does not fall below the threshold, the reclosing signal is released after 8.4 ms, which is equal to 8.33 ms (half power cycle for the power system frequency of 60 Hz) in addition to a time margin of 0.07 ms.

Table 6. Timer start and stop times corresponding to Figure 15.

Timer Actuation	Start Time [ms]	Stop Time [ms]
(i)	283.7	286
(ii)	292	294.5
(iii)	300.4	303.8
(iv)	308.2	312.1
(v)	317.1	-

3.3.1 Proposed Method Flowchart

The proposed method is implemented at each end of the line to control the local CB based on the amplitude of the received PLC signal from the other end. The flowchart of the proposed method is shown in Figure 16 and the steps are described as follows.

1. The amplitude of the received PLC signal for logical one is measured, $A(t)$.

2. The proposed method relies on the comparison of PLC signal amplitudes before and after the fault inception. As there is always a delay between inception and detection of the fault due to the protective device delay (e.g., distance relay), a buffer with a size based on the protective device speed provides a history of the PLC signal amplitude. Therefore, the last measured amplitude for logical one, $A(t)$, is fed into a first-in-last-out (FILO) buffer, and the last output of the FILO buffer is called A^*, where τ is the time step for sampling $A(t)$.

3. Once a fault is detected by the protection system (e.g., distance relays), the PLC system installed at each end of the faulty phase starts sending logical one to the other end, continuously.

4. The amplitude of the received PLC signal is measured at each end of the faulty phase, $A(t)$.

5. The amplitude of the measured signal is compared to a threshold based on the last output of the FILO buffer, A^*, and if it is greater than or equal to the threshold, the timer starts or continues counting. If A^* becomes less than the threshold, the timer stops and resets. This can be formulated as

$$\begin{cases} A(t) \geq Threshold \rightarrow timer\ starts\ or\ continues \\ A(t) < Threshold \rightarrow timer\ stops\ and\ resets \end{cases} \quad (19)$$

where $Threshold = k \times A^*$, as the amplitude of the received PLC signal after arc extinction may contain small deviations. Then, the k multiplier with a value smaller than but close to one (e.g., 0.95) is selected to eliminate the effect of probable small deviations. The selection of a smaller value for k decreases the delay in detection of arc extinction as the timer starts counting before the PLC signal reaches its peak. However, a small k may lead to unsuccessful reclosing.

6. If the timer passes the predefined time $T = \frac{1}{2 \times power\ frequency} + time\ margin$ [s], then the secondary arc is extinguished. Therefore, a reclosing signal is released and the PLC system returns to its normal function. A small time margin can be considered for improvement of the proposed method reliability. However, larger time margins reduce the speed of the proposed ASPAR method.

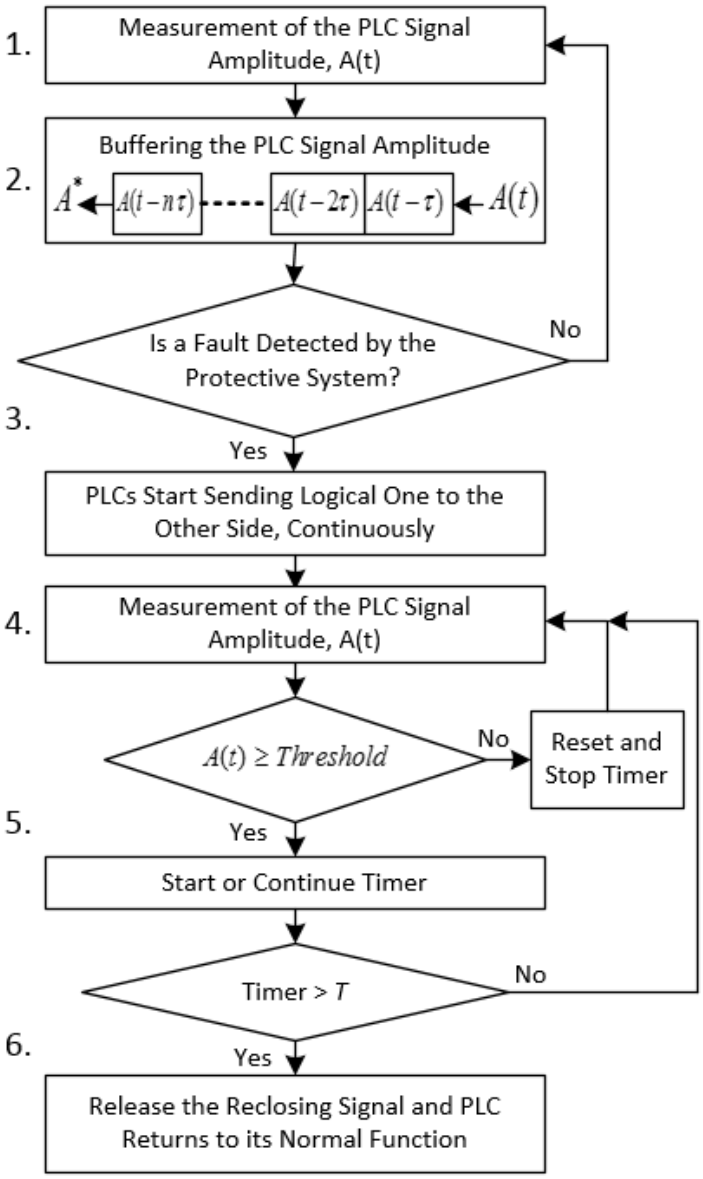

Figure 16. The flowchart of the proposed method.

3.4 Test Cases and Simulation Results

In order to evaluate the proposed method, EMTP-RV and MATLAB are utilized for carrying out and implementing the transient simulations and the proposed method, respectively. Two different transmission line topologies (Sys-1 and Sys-2) are considered based on [99] and [100], as shown in Figures 17(a) and (b), and the specifications of the test systems are provided in Table 7. The lines are modelled using the frequency dependant

(FD) line model in EMTP-RV. The following parameters are utilized for simulation of the arcs: $\tau_0 = 10^{-3}$ s, $u_0 = 12$ V/cm, $r = 2$ mΩ/cm, $l_0 = 40$ cm, and the values used for l_{arc} are based on [97]. A coupling capacitor of 4 nF and a coupling inductor of 0.5 mH are selected for both systems that leads to a resonance frequency of 112.5 kHz [8] and [93]. The shunt reactors are 50 and 100 MVAR for Sys-1 and Sys-2, respectively, and they are modelled using impedances as 16.7+j5000 Ω for Sys-1 and 19.5+j5800 Ω for Sys-2 based on [89]. The PLC signal is extracted from the measurement at the tuner location using DFT that filters out the undesirable contents of the measurement such as noises.

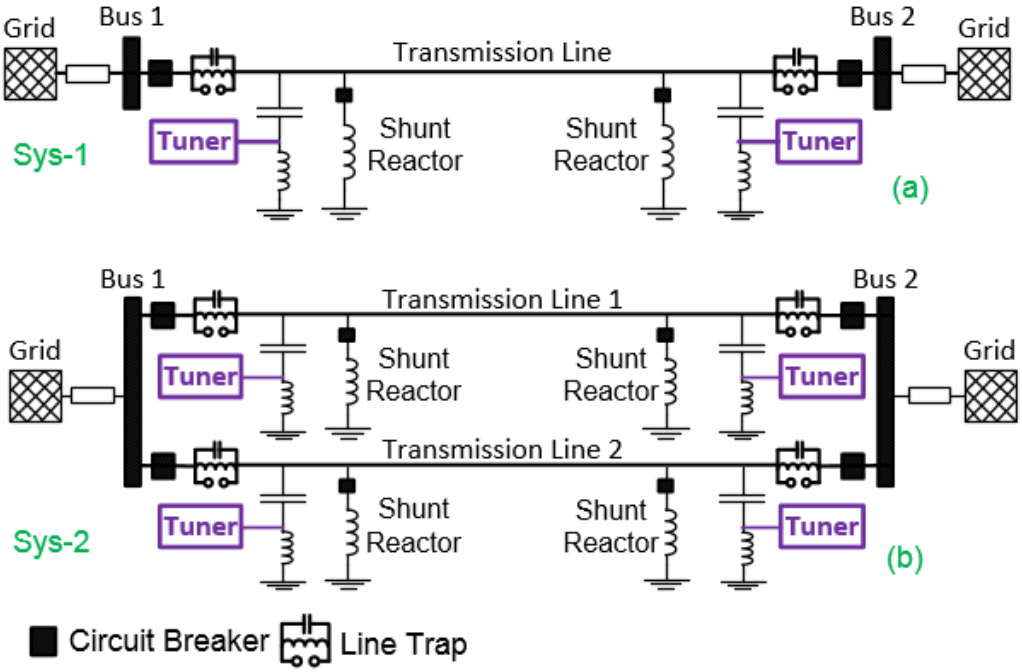

Figure 17. Single-line diagram of the test transmission lines.

Table 7. Specifications of the test systems.

System	Freq. [Hz]	Voltage [kV]	Length [km]	Circuit Type
Sys-1	60	500	100	Single
Sys-2	50	765	200	Double

3.4.1 Sensitivity Assessment

As it is common in the literature, the effects of different parameters (i.e., power system frequency, fault location, faulty phase, system loading, transmission line transposition, shunt reactors, PLC carrier frequency, and noises) on the proposed method are considered and the efficiency of the proposed method is evaluated based on the simulation results. In all of the case studies, time margins of 0.07 and 0.1 ms are considered for Sys-1 and Sys-2, respectively. Therefore, referring to the step 6 of the proposed method flowchart, $T =$ 8.4 ms for Sys-1 and $T = 10.1$ ms for Sys-2. The threshold is selected to be 95% of the normal PLC signal amplitude ($k = 0.95$). A zero-mean Gaussian noise, $\mathcal{N}(0, \sigma^2)$, is added to the measured PLC signals for consideration of the system and measurement noises, where σ^2 is the noise variance, and its size is 1% of the normal PLC signal amplitude. Different PLC carrier frequencies are evaluated as well.

Power System Frequency

As mentioned in Section 2.3, the proposed method is capable of detecting the secondary arc extinction after a delay (T), which is related to the power system frequency. For evaluation of the power frequency effect, a fault is placed on phase-*a* in the middle of the lines in both Sys-1 and Sys-2. Each simulation is carried out for connected and disconnected shunt reactors. The PLC carrier frequencies for Sys-1 are 300, 400, and 500 kHz, and the PLC carrier frequency for Sys-2 is 300 kHz. One thousand Monte Carlo simulations (MCSs) are carried out, and the average delays between the secondary arc extinction and the release of the reclosing command are 7.56 and 9.10 ms for Sys-1 and Sys-2, respectively. Therefore, the power system frequency changes the delay in secondary arc detection as described in the step 6 of the proposed method flowchart. The delays in

detection of arc extinction are shorter than 8.4 and 10.1 ms (for Sys-1 and Sys-2, respectively) since the timer starts counting before the arc extinction time (Figure 15) as the threshold is smaller than the normal PLC signal amplitude.

Fault Location

SLG faults are placed at different locations along the phase-*a* of the test systems, and the effect of fault location is evaluated. The shunt reactors are considered connected and disconnected for each fault location. The PLC carrier frequencies are selected as 30, 150, and 200 kHz. One thousand MCSs are carried out for each situation, and the average delays between secondary arc extinction and the release of the reclosing signal is presented in Table 8. The negligible differences in the delays arise from the additive noises. The fault location does not adversely affect the proposed method.

Table 8. Delays in detection of arc extinction

System	Fault Location [km]	Avg. Delay [ms]
Sys-1	25	7.56
	50	7.55
	75	7.55
Sys-2, TL1	50	9.09
	100	9.09
	150	9.09
Sys-2, TL2	50	9.09
	100	9.09
	150	9.10

Faulty Phase

An SLG fault in the middle of the lines occurs on different phases. The shunt reactors are considered connected and disconnected for each fault. The PLC carrier frequencies of 200 and 300 kHz are utilized. One thousand MCSs are carried out for each fault, and the average of the delays in detection of the secondary arc extinction are provided in Table 9.

According to the negligible differences in the average delays, the faulty phase has no effect on the proposed method.

Table 9. Delays in detection of arc extinction

System	Faulty Phase	Avg. Delay [ms]
Sys-1	a	7.55
	b	7.54
	c	7.55
Sys-2, TL1	a	9.09
	b	9.10
	c	9.09
Sys-2, TL2	a	9.09
	b	9.09
	c	9.10

System Loading

The performance of the proposed method is evaluated with respect to different system loading conditions. An SLG fault is placed in the middle of the phase-a in each transmission line. System loading conditions are simulated using various phase angle differences between Buses 1 and 2 as $\delta_{12} = 0°$, $\delta_{12} = 5°$, $\delta_{12} = 10°$, and $\delta_{12} = 15°$, where δ_{ij} indicates the phase angle difference between Buses i and j, and $(.)°$ is degree symbol. The PLC carrier frequency is 250 kHz. The average of the delays based on one thousand MCSs are provided in Table 10. As it can be noticed, the system loading has no effect on the proposed method.

Table 10. Delays in detection of arc extinction

System	Faulty Phase	Avg. Delay [ms]
Sys-1	a	7.55
	b	7.55
	c	7.54
Sys-2, TL1	a	9.09
	b	9.09
	c	9.09
Sys-2, TL2	a	9.08
	b	9.09
	c	9.09

Transmission Line Transposition

The effect of line transposition on the proposed method is also considered. Three transposition types, including ideally (fully) transposed, partially transposed, and not transposed are considered for the lines in both Sys-1 and Sys-2. For partially transposed lines, the position of the phases (line configuration) is changed at three points along the lines with the following configurations: ‘a-b-c’, ‘b-c-a’, and ‘c-a-b’. The fault occurs on phase-*a* in the middle of the lines. Both connected and disconnected shunt reactors are considered. PLC carrier frequencies of 50, 80, and 130 kHz are selected for simulations and based on one thousand MCSs, and the average delays are provided in Table 11. As it can be noticed, line transposition does not affect the proposed method accuracy.

Table 11. Delays in detection of arc extinction

System	Transposition	Avg. Delay [ms]
Sys-1	Ideally Trans. (†)	7.55
	Not Trans. (‡)	7.55
	Partial Trans. (+)	7.55
Sys-2, TL1	Ideally Trans.	9.09
	Not Trans.	9.09
	Partial Trans.	9.09
Sys-2, TL2	Ideally Trans.	9.08
	Not Trans.	9.08
	Partial Trans.	9.09

(†) denotes ideally or fully transposed line.
(+) the line is transposed only at three points.

Shunt Reactor Effect

As PLC carrier frequency is relatively high, the impedance of the shunt reactors are very high for PLC signals. Therefore, the PLC signal does not pass through the shunt reactors, and consequently, the existence of the shunt reactors does not affect the proposed method. Also, in the previous experiments, the shunt reactors are considered connected and

disconnected, and the results show that the shunt reactors do not affect the proposed method.

PLC Carrier Frequency and Operating Mode

There are two types of carrier operation modes, frequency shift keying (FSK) and On-Off modes. In FSK operation mode, the carrier frequency is keyed from a frequency to another frequency indicating zeros and ones. In On-Off mode, the PLC signal is switched on and off to send ones and zeros [8] and [93]. Both PLC operating modes can be used since the proposed method relies on logical ones as described in '2. 3. 1. Proposed Method Flowchart'. The PLC carrier frequency has no effect on the proposed method as different PLC carrier frequencies (i.e., 30, 50, 80, 130, 150, 200, 250, and 300 kHz for both Sys-1 and Sys-2, and 350, 400, 450, and 500 kHz for Sys-1) are used in the previous experiments, and it does not influence the proposed method.

3.5 Comparison

As the ASPAR method proposed in [69] detects the secondary arc extinction time faster than the other methods in the literature utilising adaptive CUSUM (ACUSUM) filter, we compare the proposed ASPAR method in this dissertation with the results in [69]. The measurement devices and the environment surrounding the transmission lines, especially in adverse weather [93], add noises to the measurements. Therefore, the proposed method is evaluated with respect to different noise levels. For each noise level one thousand MCSs carried out, and the percentages of the unsuccessful reclosing actions are provided. The variances of the noises are selected as 0.005%, 0.01%, 0.015%, 0.02%, and 0.025% of the normal PLC signal amplitude and the line-to-ground voltage for our proposed method and

the method in [69], respectively. The comparison results are given in Table 12. Also, the performance of the proposed ASPAR method is compared with recently published methods and the results are presented in Table 13. As it is noticed, the proposed method is proper for a wide range of transmission lines with different specifications.

Table 12. Noise efficiency

Method	Noise Variance	Unsuccessful Reclosure [%]
Proposed Method	0.005	ε (†)
	0.01	ε
	0.015	0.2
	0.02	0.6
	0.025	2.1
Ref. [69]	0.005	ε
	0.01	1.1
	0.015	16
	0.02	23
	0.025	41

(†) Although zero unsuccessful reclosure occurred in MCSs, absolute zero does not seem proper, considering the Gaussian noise characteristics.

Table 13. Comparison of the existing and proposed methods

Method	Single/Double Ended	Maximum Delay (†)	Transposition (I, P, N) (‡)	Single/Double Circuit Line	Shunt Reactors	Loading Condition
[69]	Single	50 Hz: 4 ms	NR (+)	AP (*)	AP	AP
[73]	Single	60 Hz: 105 ms	I, P, and N	NR	AP	AP
[79]	Single	60 Hz: 8.62 ms	NR	NR	NR	NR
[80]	Single	60 Hz: 8.60 ms	NR	NR	AP	AP
[81]	Single	60 Hz: 280 ms	I, P, and N	NR	AP	AP
[85]	Double	60 Hz: 700 ms	NR	AP	AP	AP
[86]	Double	NA (★)	NR	NR	NR	AP
[87]	Double	Less than 1 Power Cycle	NR	NR	AP	AP
[88]	Double	60 Hz: 17 to 58 ms	I	NR	AP	NR
Proposed Method	Double	Less than 1 Power Cycle	I, P, and N	AP	AP	AP

(†) The delay in reclosing after the extinction of the secondary arc. The delays are provided in millisecond or in power cycle in the literature. Therefore, the power frequency is provided in the table for the delays stated in millisecond.

(‡) Line transposition; I, P, and N indicate ideally, partially, and not transposed, respectively.

(+) NR indicates not reported.

(*) AP indicates applicable.

(★) NA indicates not applicable and the method differentiates permanent and transient faults.

3.6 Conclusion

This chapter proposes a new adaptive single-phase auto-reclosing (ASPAR) method for transmission lines, utilising power line carrier (PLC) signals. In the proposed method, the amplitude of the PLC signal for logical ones, which is received from the remote end, is always measured and buffered. After the occurrence of a fault, the protection system (e.g., distance relays together with circuit breakers) de-energizes the faulty phase. Based on the comparison of the measured amplitudes before and after the fault occurrence, the arc extinction is determined. Then, the reclosing signal is released to the local circuit breaker, and consequently, the de-energized phase becomes connected to the power system again. As PLCs are widely used over the world, the proposed method can be considered as an auxiliary application of PLC systems for enhancement of power system resilience. The performance of the proposed method is studied with respect to the following important parameters: power system frequency, fault location, faulty phase, system loading, transmission line transposition, shunt reactors, and PLC carrier frequency. The proposed method efficiency with respect to the noise is also evaluated and compared with a fast ASPAR method in the literature. Based on the simulation outcomes, it is concluded that the proposed method has proper efficiency against the mentioned parameters.

Chapter 4. Traveling-Wave Arrival-Time Detection

4.1 Introduction

Accurate fault location is a necessary post-event tool for quick power system restoration. Fault location methods are broadly divided into three major categories [29]: impedance-based, traveling wave-based, and artificial intelligence-based methods. By virtue of TRs and GPS signal receivers, traveling wave-based fault location methods become more applicable compared to impedance-based methods [104].

Occurrence of a fault induces traveling waves in transmission lines. One of the main steps in traveling wave-based methods is wave arrival time detection (so-called transient detection). Several techniques for detection of arrival times (ATs) are introduced in the literature. In [105], an arrival wave is detected through a differentiator-smoother with a three-sample window. Sliding discrete Fourier transform (SDFT) is a well-known signal analysis tool for time-frequency decomposition. However, its application in AT detection is discussed in [106] and [107], and it is concluded that SDFT results in improper time resolution for fault location purposes.

In [40], the use of discrete wavelet transform (DWT) in fault location is first proposed. Different mother wavelets (e.g., Daubechies (db) and Haar) in different scales are utilized for AT detection mainly depending on the test cases, noise severity, and sampling frequency [102], [52], and [108]. Selection of different mother wavelets and scales drastically affects the performance of DWT-based methods [109]. Therefore, customized mother wavelets based on fault-initiated waves are proposed in the literature. In [110], Morlet mother wavelet is improved to match the successive arriving waves in lateral distribution systems. This technique requires pre-fault studies on the test system for

determination of the characteristic frequencies corresponding to different wave paths. In [111], a customized mother wavelet is proposed for fault location using the time differences among the successive ATs. It results in sharper and narrower peaks at ATs compared to classical db mother wavelets. However, this method finds the customized mother wavelet through an unconstrained optimization problem with an initial guess based on db mother wavelet. According to the above-mentioned issues, other transient-detection methods are proposed in the literature.

In [112], the application of Park's transform in AT detection is addressed. It is computationally fast and does not require a window of measurement samples. Therefore, it is proper for online applications. In [113] and [114] the sensitivity of Park's transform-based methods to the noises and imbalances in power systems is reduced. However, the Park's transform is only applicable to three-phase measurements that limits the application of Clarke's transform for modal decomposition.

The performance of DWT and Hilbert transform (HT) in AT detection are compared in [115], and it is concluded that HT detects ATs more accurately than DWT. In [116] and [117], HT is utilized for AT detection and subsequently for traveling wave-based fault location. However, low sampling frequencies detract from HT-based fault location methods.

Accordingly, a robust technique is required for AT detection since the current techniques (e.g., DWT and HT) are to some extent affected by the measurement noise, sampling frequency, and fault parameters. In this chapter, we propose two novel AT-detection methods as follows

i) An AT-detection method based on the short-time matrix pencil method (STMPM) is

first proposed. However, as STMPM detects the ATs through matrix algebra, it requires high processing capability, that is challenging for implementation of STMPM in on-site microprocessor-based fault locators for online applications.

ii) As STMPM is a computationally-expensive algorithm, a new recursive method for detection of the first traveling-wave arrival times (ATs) in power systems is proposed. The new method enhances the performance of the traveling wave-based fault-location methods relying on the first wave arrival times. The proposed method is based on the detection of the abrupt changes in the innovation sequence (residuals) generated by Adaptive Discrete Kalman Filter (ADKF). As the proposed method is recursive, it is proper for being implemented in microprocessors for online applications.

The sensitivity of the proposed methods is evaluated for the following parameters: measurement noise, non-ideal fault (NIF), fault inception angle (FIA), location of the fault, and sampling frequency (F_s). The proposed technique is compared to DWT (with db-4 and Haar mother wavelets in different scales) and HT. According to the simulation results, the proposed techniques are less influenced by the above parameters. Thus, traveling wave-based fault location methods will be profoundly improved if the proposed techniques are used for AT detection (e.g., instead of DWT), especially for highly noise-contaminated measurements, small FIAs, and low sampling frequencies. As the proposed techniques are able to accurately estimate ATs using low sampling rate measurements, they can readily be used for fault location processing using the existing commercial digital fault recorders (DFRs) and power quality analyzers.

4.2 Traveling-wave detection technique using short-time matrix pencil method[4]

In the following subsections the AT-detection method based on STMPM is described. The simulation results are provided and the STMPM-based method is compared to the existing AT-detection methods.

4.2.1 Short-Time Matrix Pencil Method (STMPM)

Based on Fourier series, a band-limited signal in a time period of T is represented by a summation of sinusoidals as

$$x(t) = \sum_{n=1}^{N} A_n \cos(2n\pi t/T + \phi_n) \tag{20}$$

where Signal $x(t)$ in a period T is expanded by sinusoidals with residues $A_n \angle \phi_n$, N is the number of the terms to be used in reconstruction of the signal, and n indicates the term number. Similarly, one can represent a signal by a summation of damped sinusoidals as

$$x(t) = \sum_{n=1}^{N} A_n e^{-\alpha_n t} \cos(\omega_n t + \phi_n) \tag{21}$$

where $\alpha_n \pm j\omega_n$ is the n-th complex frequency, α_n [s^{-1}] and ω_n [Hz] are the real part (i. e., damping factor) and imaginary part of the complex frequency, respectively. Fourier series in (20) can be considered as a special case of (21) if $\alpha_n = 0, \forall n$. Various approaches, such as Prony [118] and the matrix pencil method (MPM) [119], are employed for extraction of the complex frequencies and residues in (21) and MPM shows promising performance [119].

In practice, a part of a signal bounded in a sliding window is often considered and

[4] Reprinted in line with copyright and author-rights for "Traveling-wave detection technique using short-time matrix pencil method," by R. J. Hamidi, H. Livani, and R. Rezaeisarlak, IEEE Trans. Power Delivery, Early Access.

represented with a few number of terms. Figure 18(a) shows a pulse in a window of length T_W. The window is located at $t = t_0$ and slided along the time axis. The MPM is applied to each snapshot of the signal. This method is called short-time matrix pencil method (STMPM) and extracts time-indexed complex frequencies [120]. In Figure 18(b), the reconstructed signals by STMPM and SDFT are compared for the same number of terms. When the sliding window moves along the signal, different numbers of complex frequencies are extracted by STMPM at different locations. SDFT is then used to reconstruct the signal at each location using the same number of terms that STMPM provides. As it is observed from Figure 18(b), STMPM represents the original signal more accurately compared to SDFT. STMPM provides a more accurate reconstructed signal compared to SDFT because in STMPM, two degrees of freedom as damping factors and sinusoidals are utilized, while in SDFT, only the sinusoidals are used.

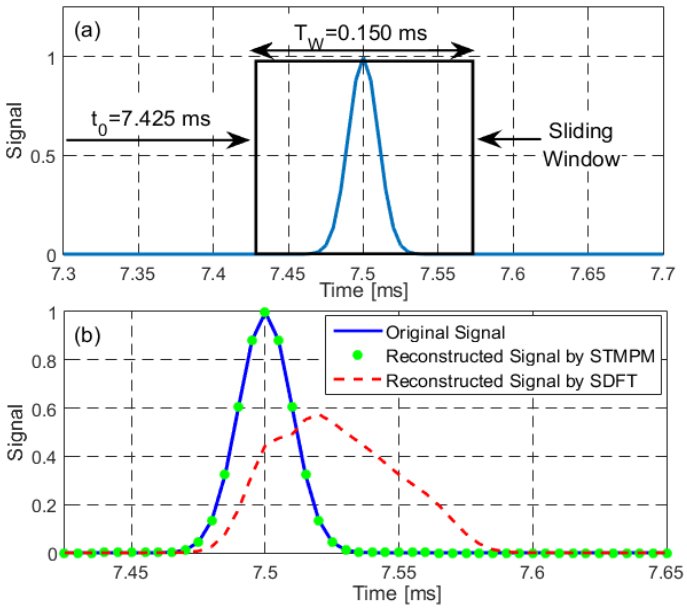

Figure 18. (a) Pulse-shape signal and sliding window. (b) Reconstructed pulse by STMPM and sliding discrete Fourier transform (SDFT) with the same number of terms. The sampling frequency is 200 kHz.

4.2.2 Trace of Arriving Waves and STMPM Formulation

The proposed technique is based on a feature of STMPM discussed in [120] and [121] as follows: referring to Figure 18(a), in STMPM, a sliding window moves along the signal. In each snapshot, MPM is applied to the samples inside the window and time-indexed complex frequencies are extracted. As described in [121], before reaching the pulse (produced by an arriving wave), the damping factors (α) are ideally zero (damping factors deviate from zero due to rounding errors, measurement resolution, and measurement noises). When the pulse is placed on the right side of the window, the damping factors become positive. As the window moves further, the damping factors tend to zero, and become almost zero when the pulse is exactly placed in the middle of the window. The damping factors become negative once the pulse is placed on the left side of the window.

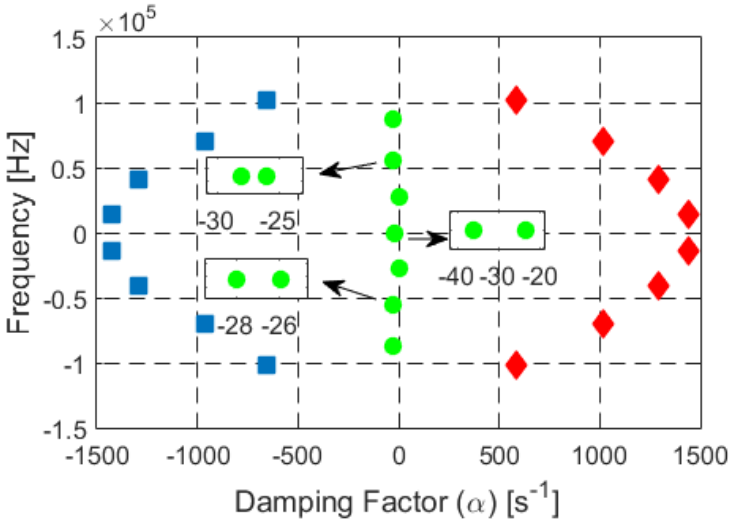

Figure 19. The complex frequencies extracted by applying STMPM to the pulse shown in Figure 1(a). Diamonds, circles, and squares show the complex frequencies when the pulse is in the right, middle, and left side of the sliding window, respectively.

For example, the extracted complex frequencies of the signal shown in Figure 18(a) are depicted in Figure 19 for three cases: $t_0 = 7.375, 7.425$, and 7.475 ms, and $T_W = 0.150$

ms. As Figure 19 shows, the extracted damping factors (α) are positive (diamonds) when the pulse is located on the right side of the window ($t_0 = 7.375$ ms), and they are negative (squares) when the pulse is on the left side ($t_0 = 7.475$ ms). As an important case, the damping factors are close to zero (circles) for the pulse placed in the middle of the window ($t_0 = 7.425$ ms). This trend can be used for AT detection, and it is mathematically written as

$$\alpha_n = 0, \forall n \rightarrow AT = t_0 + T_W/2 \tag{22}$$

where α_n is the damping factor, t_0 denotes the sliding window location, T_W is the sliding window length, and AT is the arrival time ($AT = 7.425 + 0.150/2 = 7.5$ ms).

4.2.3 STMPM Formulation

The formulation of STMPM is as follows: first, using the samples in an N-sample sliding window, the matrix $\boldsymbol{Y}_{(N-L)\times(L+1)}$ is formed as

$$\boldsymbol{Y} = \begin{bmatrix} x(1) & x(2) & \dots & x(L+1) \\ x(2) & x(3) & \dots & x(L+2) \\ \vdots & \vdots & \vdots & \vdots \\ x(N-L) & x(N-L+1) & \dots & x(N) \end{bmatrix} \tag{23}$$

where $x(.)$ denotes the samples, N indicates the number of samples in the window, and L is referred to as pencil parameter, which is selected between $N/3$ to $N/2$ for effective noise filtering [119]. In the next step, applying singular-value decomposition (SVD) to the matrix $\boldsymbol{Y}$ yields

$$\boldsymbol{Y} = \boldsymbol{U} \sum \boldsymbol{V}^H \tag{24}$$

where $(.)^H$ denotes complex conjugate, $\boldsymbol{U}$ and $\boldsymbol{V}$ are unitary matrices comprising eigenvectors of $\boldsymbol{Y}\boldsymbol{Y}^H$ and $\boldsymbol{Y}^H\boldsymbol{Y}$, respectively. $\sum$ is a diagonal matrix consisting of the singular values of $\boldsymbol{Y}$.

For reducing the measurement noise, dominant singular values of $\sum$ are selected as $\sigma_d \geq 10^{-p}\,\sigma_{max}$, where σ_d is the dominant singular value, σ_{max} is the maximum singular value, and p is the filtering factor [119]. The columns of $\sum$ corresponding to its dominant singular values are saved and the remaining columns are removed, and the reduced matrix is called $\sum'$. Also, the matrix $\boldsymbol{V}$ is reduced to $\boldsymbol{V'}$ by saving its columns corresponding to the dominant singular values and removing the remaining columns [119]. Then, two new matrices $\boldsymbol{Y}_1$ and $\boldsymbol{Y}_2$ are constructed as

$$\boldsymbol{Y}_1 = \boldsymbol{U}\sum'\boldsymbol{V}_1'^{H}\ ,\boldsymbol{Y}_2 = \boldsymbol{U}\sum'\boldsymbol{V}_2'^{H} \tag{25}$$

where $\boldsymbol{V}_1$ is obtained by removing the last row of $\boldsymbol{V'}$ and $\boldsymbol{V}_2$ is obtained by removing the first row of $\boldsymbol{V'}$. Then, the eigenvalues of $\boldsymbol{Y}_1^{+}\boldsymbol{Y}_2$ ($(.)^{+}$ indicates Moore–Penrose pseudoinverse) are calculated. The relation between these eigenvalues and complex frequencies is given by [119]

$$\lambda_n = e^{(-\alpha_n \pm j\omega_n)T_s}, \forall n = 1,2,\dots,m \tag{26}$$

where λ indicates the eigenvalues and T_s is the sampling period. After calculation of eigenvalues, time-indexed complex frequencies for each snapshot are obtained as

$$\alpha_n(t) \mp j\omega_n(t) = -\ln(\lambda_n)/T_s, \forall n = 1,2,\dots,m \tag{27}$$

The procedure described in (23)-(27) is repeated for each snapshot provided by the sliding window. As an example, Figure 20 shows a noise-contaminated voltage measurement with arriving waves. Applying STMPM with $T_W = 0.150$ ms to the signal shown in Figure 20 provides the damping factor-time diagram depicted in Figure 21(a). It is noticed that the location of the first arriving wave matches the location of almost zero damping factors.

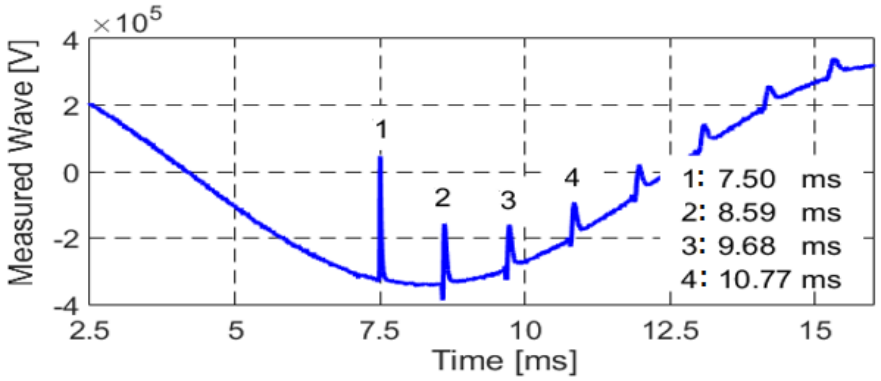

Figure 20. A typical fault-induced arriving wave. The fault inception time is set such that the first arriving wave reaches the ending terminal at 7.5 ms. The sampling frequency is 100 kHz.

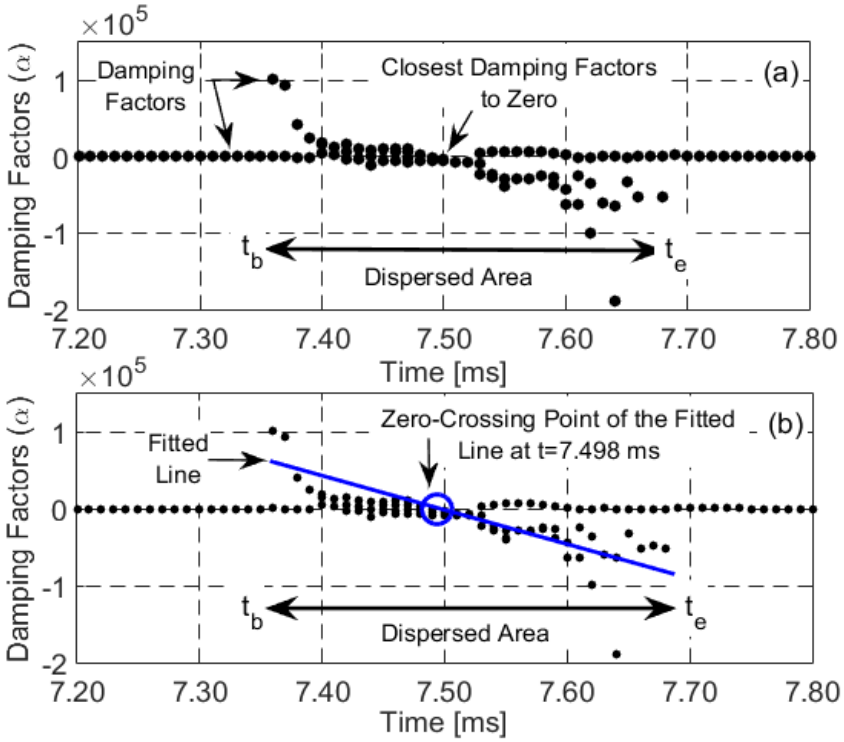

Figure 21. (a) The damping factor-time diagram obtained by applying STMPM to the measurement shown in Figure 3. (b) The fitted line to the dispersed damping factors, and its zero-crossing point.

4.2.4 Arrival Time Detection

For a more accurate estimation of the zero-crossing point of the damping factors, linear regression is applied to the dispersed damping factors (dependent variables) and time (the independent variable). Then, the zero-crossing point of the fitted line approximates the AT,

as shown in Figure 21(b). Linear regression is formulated as

$$\alpha_n(t) = b_0 + b_1 t + \epsilon_n(t), \forall t \in (t_b, t_e), \forall n \tag{28}$$

where $\alpha_n(t)$ is the time-indexed damping factor at time t, t_b and t_e indicate the beginning and end of the dispersed area, respectively, as shown in Figures 21(a) and 21(b). b_0 and b_1 are the linear regression coefficients and $\epsilon_n(t)$ is the error at time t. Equation (9) is written in matrix form as

$$\boldsymbol{\alpha} = \boldsymbol{x}\boldsymbol{b} + \boldsymbol{\epsilon} \tag{29}$$

where $\boldsymbol{\alpha} = [\alpha_n(t_b), \dots, \alpha_n(t_e)]^T$ is the vector of time-indexed damping factors, $\boldsymbol{b} = [b_0, b_1]^T$ is the vector of regression coefficients, $\boldsymbol{\epsilon} = [\epsilon_n(t_b), \dots, \epsilon_n(t_e)]^T$ is the vector of errors, and $\boldsymbol{x} = \begin{bmatrix} 1 & \dots & 1 \\ t_b & \dots & t_e \end{bmatrix}^T$ is the matrix of independent variables. The regression coefficients are calculated by solving

$$\min_{b_0, b_1} (\boldsymbol{\alpha} - \boldsymbol{x}\boldsymbol{b}) \tag{30}$$

As (10) is a set of linear equations, the solution to (11) is

$$\hat{\boldsymbol{b}} = (\boldsymbol{x}^T\boldsymbol{x})^{-1}\boldsymbol{x}^T\boldsymbol{\alpha} \tag{31}$$

where $\hat{\boldsymbol{b}} = \left[\hat{b}_0, \hat{b}_1\right]^T$ is the vector of the estimated regression coefficients, $(.)^T$ indicates matrix transposition. Since $\alpha = 0$ at the zero-crossing point, the AT is found by solving $\hat{b}_0 + \hat{b}_1 t = 0$ and obtained as

$$AT = -\hat{b}_0/\hat{b}_1 \tag{32}$$

where AT is the estimated arrival time.

As an example, the ATs of the first four arriving waves in Figure 20 are estimated and shown in Figure 22.

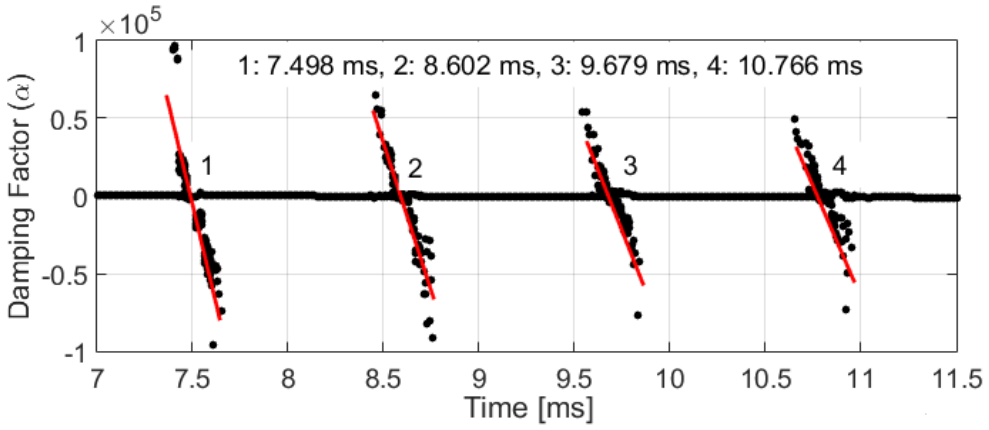

Figure 22. The estimated arrival times for the first four arriving waves shown in Figure 20.

4.2.5 The Proposed Technique Flowchart

Figure 23 shows the flowchart of the proposed technique with the following steps:

1. The sliding window moves forward along the time axis.
2. Using the samples in the window, the matrix $\boldsymbol{Y}$ is formed as described in (23).
3. Applying SVD to the matrix $\boldsymbol{Y}$ yields the matrices $\boldsymbol{U}$, $\sum$, and $\boldsymbol{V}$ as stated in (24).
4. The dominant singular values in $\sum$ are selected.
5. The matrices $\sum'$ and $\boldsymbol{V}'$ are formed by selection of the columns corresponding to the dominant singular values.
6. The matrices $\boldsymbol{Y}_1$ and $\boldsymbol{Y}_2$ are formed using (25).
7. The eigenvalues of $\boldsymbol{Y}_1^{+}\boldsymbol{Y}_2$ are calculated.
8. As the calculated eigenvalues are related to the complex frequencies, using (27) the time-indexed damping factors are obtained.
9. The procedure continues until the last sample of the signal is reached.
10. The dispersed area in damping factor-time diagram is observed that begins at t_b and finishes at t_e as shown in Figures 21(a) and 21(b).
11. Using linear regression, a line is fitted to the dispersed damping factors for obtaining

the relation between time and damping factors.

12. The zero-crossing point of the fitted line is calculated using (32), and it estimates the AT.

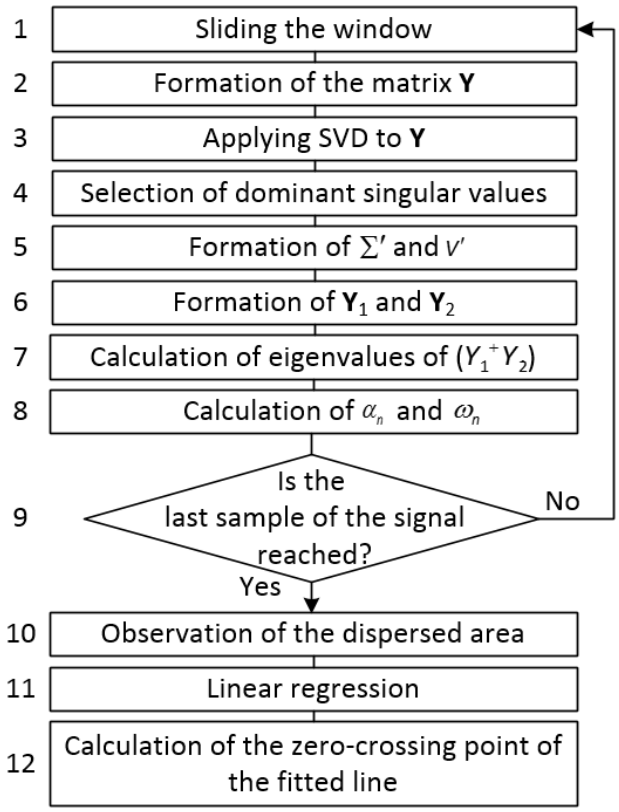

Figure 23. The flowchart of the proposed technique.

4.2.6 Computational Burden of the Method

As the proposed technique utilizes matrix algebra, the computational burden is relatively high, and it requires high processing ability for online applications. However, fault location is usually carried out offline as a post-fault analysis task. Therefore, the proposed technique can be utilized using normal computers. Table 14 provides the processing time related to each step of the proposed algorithm using MATLAB installed on a computer with an Intel(R) Xeon(R) E5420 processor and 16 GB of RAM. No effort was made for optimization of the running time.

A part of the signal shown in Figure 20 (from $t = 0$ to $t = 10$ ms) with the length of 1000 samples ($F_s = 100$ kHz) is fed to the proposed algorithm. The average computational time for each step is then calculated and reported in Table 14. The size of the matrix $\boldsymbol{Y}$ is 20-by-11 corresponding to the selection of $N = 30$ and $L = 10$, and the filtering parameter, P, is 3. The total running time for processing 1000 measurement samples is 18.520 s and the average process time for each sample is 18.520 ms.

Table 14. Processing times of the proposed algorithm steps

Step Number	Avg. time [ms]	Step Number	Avg. time [ms]	Step Number	Avg. time [ms]
1	0.002	5	0.902	9	0.002
2	0.032	6	3.122	10	N/A (†)
3	4.770	7	7.368	11	0.542
4	1.004	8	0.774	12	0.002

(†) "N/A" denotes not applicable.

4.2.7 Test Case

In order to evaluate the performance of the proposed technique, the test case and fault location method in [107] are utilized. However, the proposed technique is applicable to more complicated transmission systems (e.g., hybrid [45] or multi-terminal transmission systems [43]) and more sophisticated fault location methods [20], as shown in Appendix C. 2. As Figure 24 shows, both ends of the transmission line are equipped with transient recorders (TRs) and GPS signal receivers for synchronization of the measurements. The topology of the transmission line is based on [49]; its length is 200 mi and the voltage level is 345 kV. The transmission line is transposed. It is modeled using the frequency-dependent line model (EMTP FD model). Traveling wave velocity is 183486 mi/s in the aerial mode (i.e., wave traveling time is 1090 μs in the aerial mode). The fault location method proposed in [106] is formulated as

$$CFL = (L - v\,t_d)/2 \tag{33}$$

where CFL [mi] is the calculated fault location, L [mi] is the transmission line length, $t_d = t_2 - t_1$ [s] in which t_1 and t_2 are the ATs at Terminals 1 and 2, respectively. v [mi/s] is the traveling wave velocity. Fault location errors are calculated as

$$err = \frac{|AFL - CFL|}{L} \times 100\% \tag{34}$$

where err [%] is the fault location error, AFL [mi] is the actual fault location, and L [mi] is the length of the transmission line.

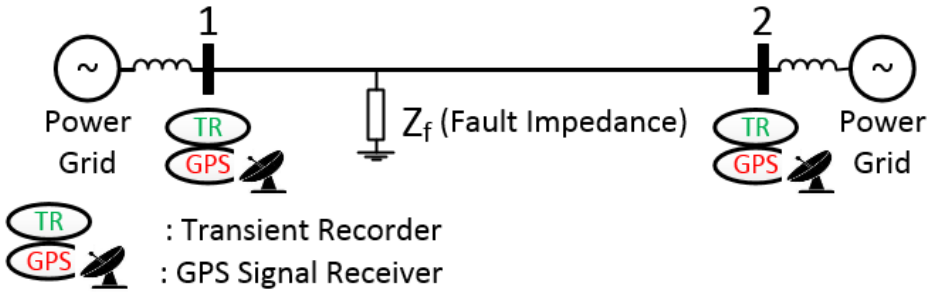

Figure 24. One-line diagram of the test system.

4.2.8 Arrival Time Detection

In this section, the ability of the proposed technique for AT detection is compared to the existing techniques in two cases with noisy measurements. A single-line-to-ground (SLG) fault occurs in the middle of the line at 12 ms (100 mi from Terminal 1, $FIA = -8^0$ and $F_S = 200$ kHz). Zero-mean Gaussian noises are added to all the measured voltages, where their standard deviations (SDs) equal $0.01V_p$ and V_p is the peak voltage ($V_p = 345 \times \sqrt{2/3}$ kV).

Figure 25(a) shows the aerial mode of three-phase voltage measurements at Terminal 1 which is calculated using Clarke's transform [105]. The actual AT at Terminal 1 is 12.545 ms and $Z_f = 1\ \Omega$. Figure 25(b) depicts normalized squares of wavelet transform coefficient

(WTC^{2}s) for db-4 mother wavelet in scale 1. It is observed that the AT cannot be detected due to the measurement noise. Figure 25(c) shows the WTC^{2}s for db-4 mother wavelet in scale 2 which is more robust against the noise and detects the AT as 12.545 ms. Figure 25(d) shows the WTC^{2}s for Haar mother wavelet in scale 1. It detects AT as 12.540 ms. Figure 25(e) shows the normalized squared instantaneous frequency calculated using HT. The formulation of HT transform is given in Appendix A. It detects the AT at 12.545 ms. Figure 25(f) shows the damping factors-time diagram using the proposed technique and the AT is estimated as 12.544 ms. Figure 26(a) shows the aerial mode voltage at Terminal 1 corresponding to an identical fault to Figure 8, except for $Z_f = 5\ \Omega$. It is noticed that only the proposed technique is able to detect the AT and the other techniques fail to detect the AT since the signal-to-noise ratio (SNR) is small compared to that in Figure 25. Table 15 presents the absolute errors in AT detection related to the different techniques. Therefore, it is concluded that the proposed technique accurately estimates the ATs in the case of fault-initiated traveling waves with low SNRs.

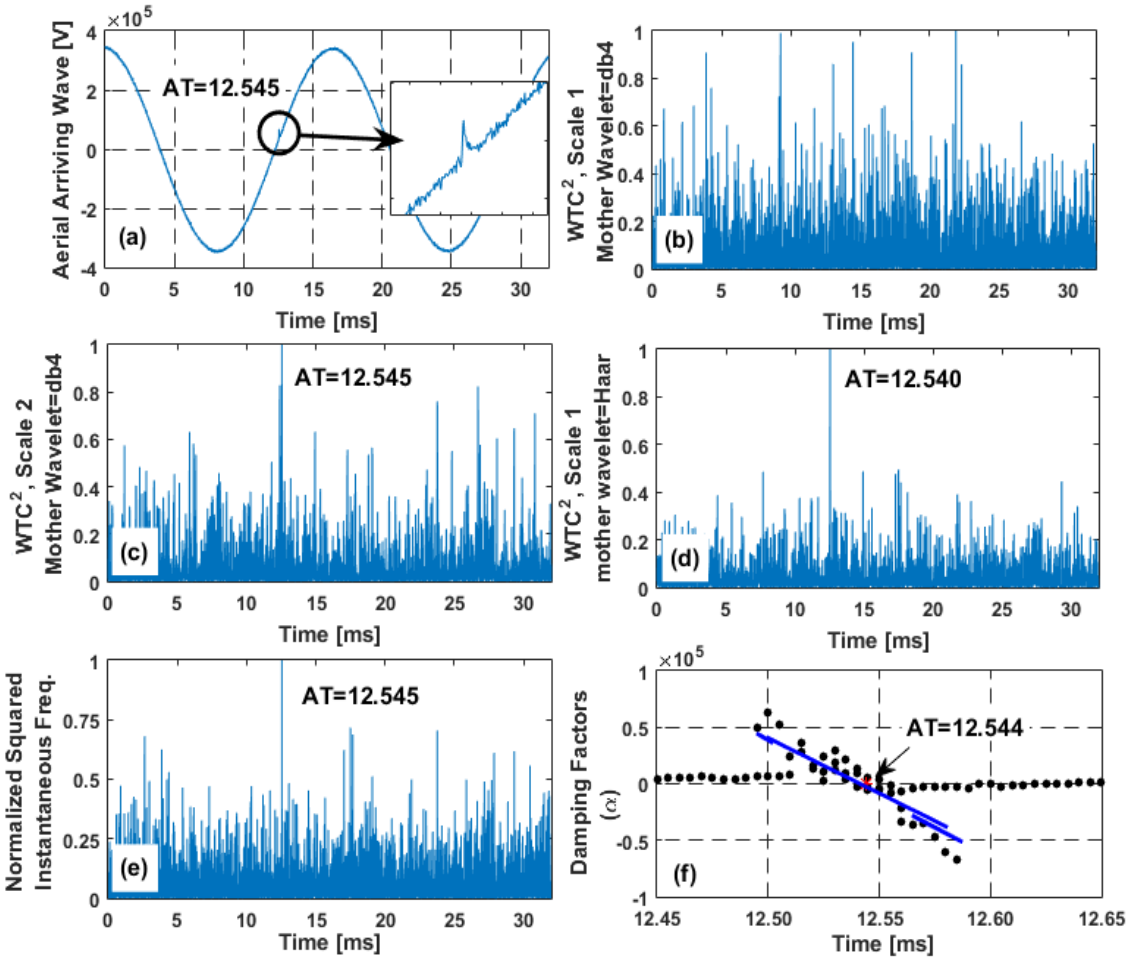

Figure 25. Arrival time detection by different techniques. (a) the aerial mode of three-phase voltage measurement at Terminal 1. (b) Normalized WTC^2s with db-4 in scale 1. (c) Normalized WTC^2s with db-4 in scale 2. (d) Normalized WTC^2s with Haar in scale 1. (e) Normalized squared instantaneous frequency. (f) The proposed technique.

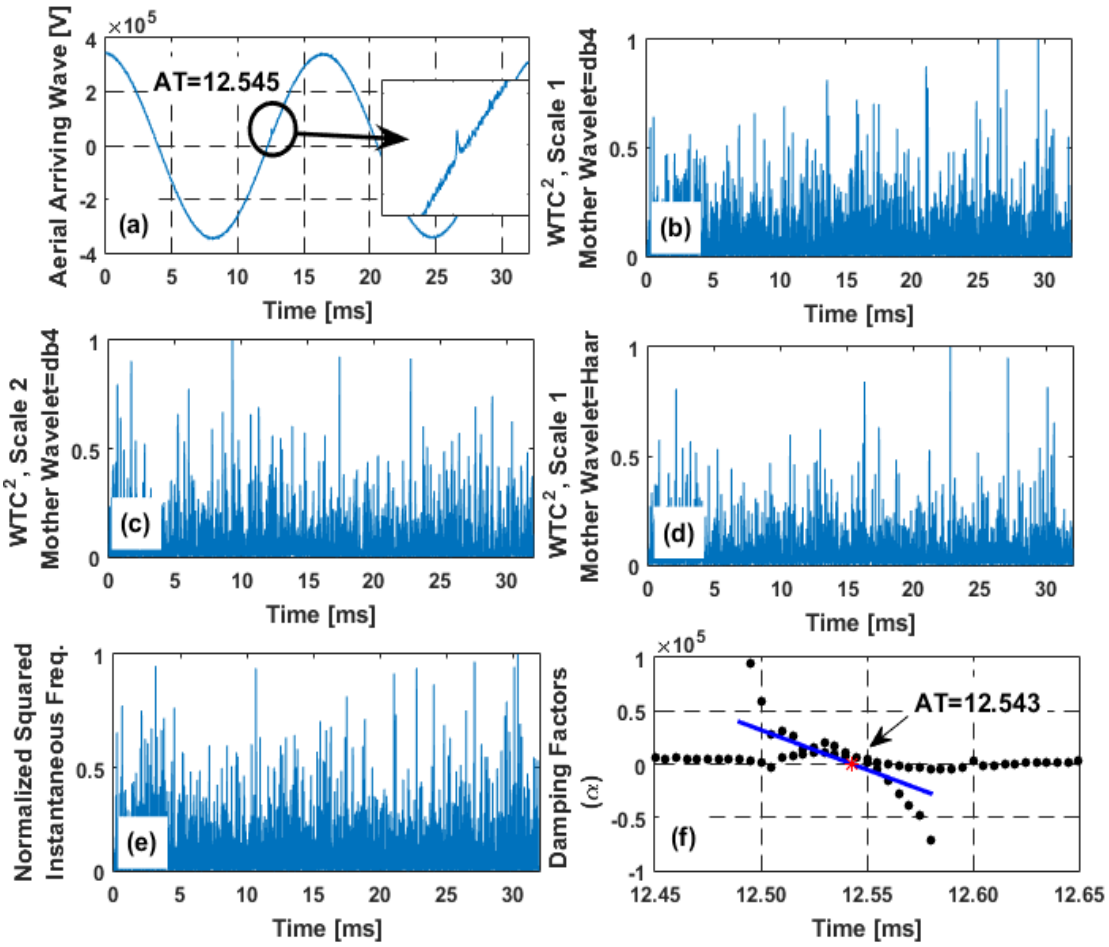

Figure 26. Arrival time detection by different techniques. (a) The aerial mode of three-phase voltage measurement at Terminal 1. (b) Normalized WTC^2s with db-4 in scale 1. (c) Normalized WTC^2s with db-4 in scale 2. (d) Normalized WTC^2s with Haar in scale 1. (e) Normalized squared instantaneous frequency. (f) The proposed technique.

Table 15. Absolute errors resulted from different techniques

Z_f [Ω]	1				
Technique	db-4, scale 1	db-4, scale 2	Haar, scale 1	HT	Proposed technique
Absolute Error (†) [μs]	N. D. (‡)	0	5	0	1
Z_f [Ω]	5				
Absolute Error [μs]	N. D.	N. D.	N. D.	N. D.	2

(†) Absolute Error = |actual arrival time-detected arrival time|.
(‡) Arrival time is not detected.

4.2.8.1 Sensitivity Analysis

In this section, the effect of influencing parameters (i.e., measurement noises, non-ideal

faults, FIA, sampling frequency, and fault location) on the proposed and other AT-detection techniques are evaluated and compared as a common practice for sensitivity analysis of a new proposed algorithm [41], [52], and [102].

Noise Sensitivity

In this section, the sensitivity of the proposed technique with respect to measurement noises is compared to other existing techniques. First, an SLG fault is assumed to occur at 100 mi from Terminal 1 ($Z_f = 5\ \Omega$, $FIA = 30^0$, and $F_S = 200$ kHz). The fault location is then estimated using different AT- detection techniques in one hundred Monte Carlo simulations (MCSs) with Gaussian measurement noises. The statistical results of the fault location errors are shown in Figure 27 for different detection techniques. The box-plot represents median, minimum, maximum, first quartile, and third quartile of the fault location errors. The fault location errors in a noiseless case are provided in Figure 27(a) for comparison purposes. As the measurements are noisy in practical conditions, zero-mean Gaussian noises are added to all voltage measurements with the following SDs: $0.005V_p$, $0.0075V_p$, $0.01V_p$, and $0.0125V_p$.

According to the results shown in Figure 27, DWT with db-4 in scale 1 does not provide accurate outcomes for $SD \geq 0.005V_p$ (i.e., large fault location errors such as 100% indicate that the related AT-detection technique is not able to detect the AT). The performance of db-4 in scale 2 is acceptable for the noise with an SD up to $0.01V_p$. However, for a heavily noise-contaminated measurement ($SD = 0.0125V_p$, Figure 27(e)), it fails to detect the AT, while the proposed technique, Haar mother wavelet, and HT are still able to correctly find the fault location. Figure 28 provides the statistical results of 100 MCS fault location errors

for a fault at 1 mi from Terminal 1 (SLG fault, $Z_f = 5\ \Omega$, $FIA = 30^0$, and $F_S = 200$ kHz) with the same range of measurement noises. As it can be observed and compared in Figures 27 and 28, and in accordance with [102], [48], and [122], AT detection becomes more challenging, and consequently, fault location errors become larger for close-in faults. Referring to Figure 28, db-4 mother wavelet in scale 1 does not provide accurate outcomes.

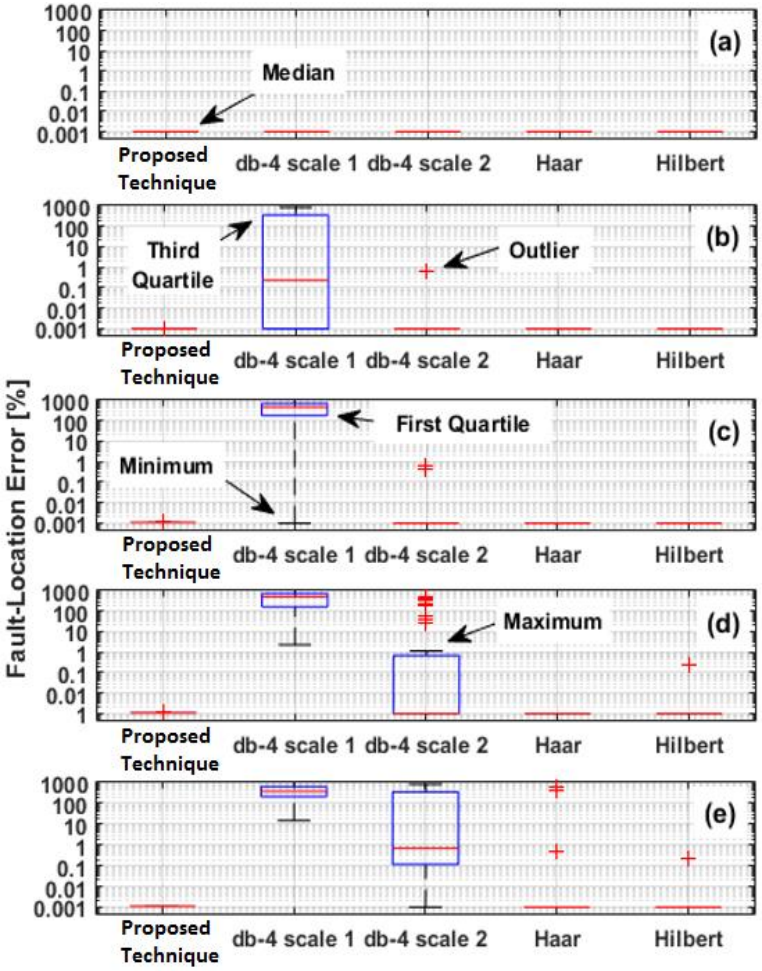

Figure 27. Fault location error, SLG fault at 100 mi away from Terminal 1, $Z_f = 5\ \Omega$, and $FIA = 30^0$, and $F_S = 200$ kHz. (a) Noiseless case. (b) $SD = 0.005V_p$. (c) $SD = 0.0075V_p$. (d) $SD = 0.01V_p$. (e) $SD = 0.0125V_p$.

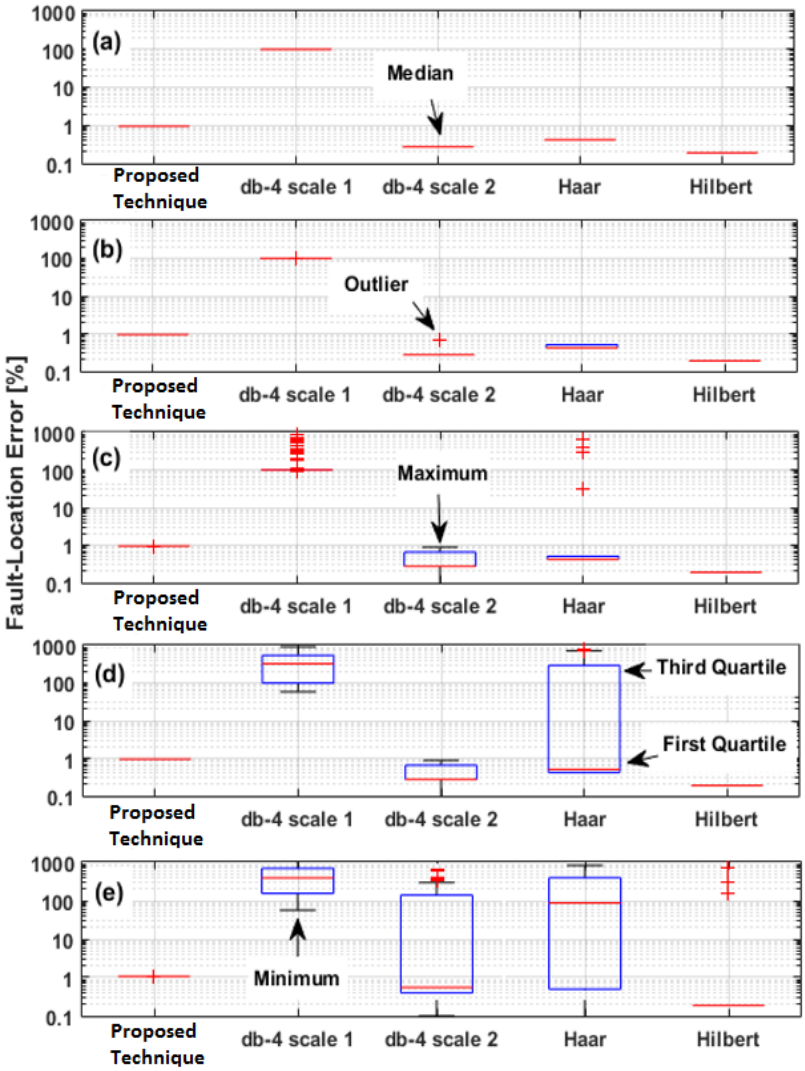

Figure 28. Fault location error, SLG fault at 1 mi away from Terminal 1, $Z_f = 5\ \Omega$, and $FIA = 30^0$, and $F_S = 200$ kHz. (a) Noiseless case. (b) $SD = 0.005V_p$. (c) $SD = 0.0075V_p$. (d) $SD = 0.01V_p$. (e) $SD = 0.0125V_p$.

The performance of Haar mother wavelet is relatively inaccurate for close-in faults since it is able to find the fault location only for noisy measurements with $SD \leq 0.075V_p$. Db-4 in scale 2, HT and the proposed technique provide accurate and consistent results for noisy measurements in the case of a close-in fault. Therefore, the fault location is found with a negligible variation.

Non-Ideal Faults

Fault impedance (Z_f in Figure 24) influences the shapes of the fault-induced traveling waves [102]. A resistive Z_f (Figure 24) is generally considered in the literature. However, the inductive part of Z_f becomes considerable for a fault between phases and towers or ground wires [56] and [123]. The fault impedance with different X_f/R_f ratios generates traveling waves with different shapes that affect AT-detection techniques. An SLG fault ($FIA = 15^0$ and $F_S = 200$ kHz) occurs at 25 mi from Terminal 1. The fault impedance is constant ($Z_f = R_f + jX_f = 2\ \Omega$), however, the X_f/R_f ratios are 0.05, 0.1, and 0.2. The shapes of the arriving waves at the terminals are shown in Figure 29. As it can be observed, the arriving waves at Terminal 1 are not similar with respect to their shapes for different X_f/R_f.

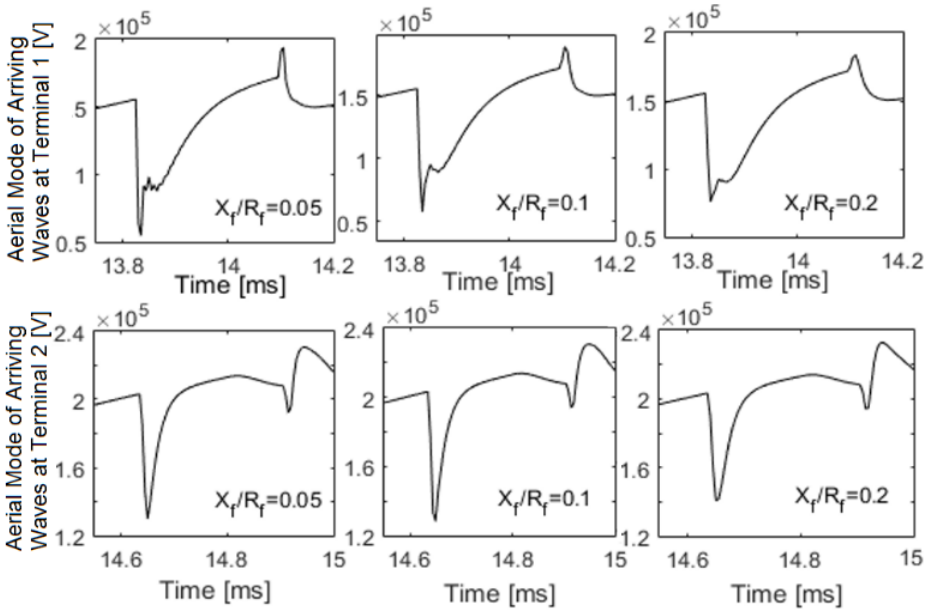

Figure 29. Arriving waves at Terminals 1 and 2 for different X_f/R_f ratios.

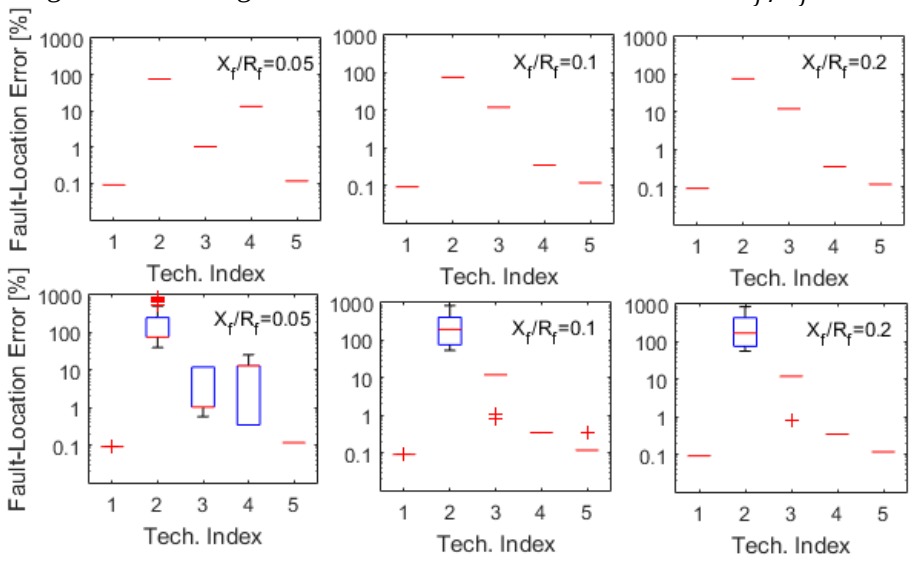

Figure 30. Fault location errors related to $Z_f = R_f + jX_f = 2\ \Omega$ with a variant X_f/R_f ratio. Tech. indices are: 1, the proposed technique; 2, db-4 in scale 1; 3, db-4 in scale 2; 4, Haar; and 5, HT.

Fault Inception Angle (FIA)

FIA influences the severity of fault-initiated traveling waves. The faults with smaller FIAs produce traveling waves with smaller amplitudes and the traveling waves are more prone to vanish in the noise, and therefore, their detection becomes more challenging. Table 16 provides the effect of FIA on the transient-detection techniques for an SLG fault

($Z_f = 1\ \Omega$ and $F_S = 200$ kHz) with different FIAs. Zero-mean Gaussian noises with $SD = 0.01V_p$ are added to all measurements and the actual fault locations are given in Table 16. Based on the simulation results, the proposed method, db-4 mother wavelet in scale 2, and HT correctly estimate the location of the faults with $FIA \geq 7^0$. However, for transmission lines with higher attenuation factors (i.e., attenuation factor equals $e^{-\alpha L}$, where α is the attenuation constant [mi^{-1}], [51]) or for higher noise levels, the location of faults with larger FIAs can be found.

Table 16. The effect of FIA on fault location

Transient Detection Technique	AFD [mi]	FIA [^{0}]				
		4	5	6	7	8
		Fault Location Error [%]				
db-4, scale 1	1	N/A	N/A	N/A	N/A	N/A
	5	N/A	N/A	N/A	N/A	N/A
	50	N/A	N/A	N/A	N/A	N/A
	100	N/A	N/A	N/A	N/A	N/A
db-4, scale 2	1	N/A	N/A	N/A	1.044	1.028
	5	N/A	N/A	N/A	1.026	1.011
	50	N/A	N/A	0.408	0.402	0.401
	100	N/A	N/A	0.022	0.018	0.018
Haar, scale 1	1	N/A	N/A	N/A	N/A	N/A
	5	N/A	N/A	N/A	N/A	N/A
	50	N/A	N/A	N/A	N/A	N/A
	100	N/A	N/A	N/A	N/A	N/A
HT	1	N/A	N/A	N/A	0.288	0.271
	5	N/A	N/A	N/A	0.178	0.172
	50	N/A	N/A	0.082	0.069	0.068
	100	N/A	0.009	0.005	0.005	0.005
The Proposed Technique	1	N/A	N/A	N/A	0.488	0.423
	5	N/A	N/A	0.418	0.318	0.317
	50	N/A	N/A	0.150	0.150	0.142
	100	N/A	0.007	0.003	0.002	0.002

"N/A" shows that the technique is not applicable.

Sampling Frequency and Fault Location

According to Nyquist-Shannon's sampling theorem, frequency contents up to half of the

sampling frequency are measurable. As a measuring device has a limited bandwidth, it filters out high frequency contents of the measurements. Thus, the sharpness and amplitude of arriving waves are mitigated, and therefore, AT detection becomes more challenging. Moreover, a lower sampling frequency leads to a lower time resolution that increases AT-detection errors. Additionally, the attenuation factor of cables drastically increases for high frequency contents of traveling waves [102]. Hence, the high frequency contents mitigate and disappear in the noise. Accordingly, high sampling measurements (e.g., $F_S = 500$ kHz) are not applicable in the case of long cables [102]. Therefore, the performance of the AT-detection techniques should be evaluated with respect to relatively lower sampling frequencies.

Furthermore, high sampling rate digital fault recorders (DFRs) and power quality meters provide measurements with a sampling frequency around 20 kHz [124]-[126]. The proposed technique is able to detect the ATs using low sampling frequencies, therefore, it provides traveling wave-based fault location application as an additional feature for the mentioned devices.

Figure 31 depicts the fault location errors along the transmission line for every 10 mi (SLG fault, $Z_f = 1\ \Omega$, and $FIA = 90^0$) with sampling frequencies of 200, 100, 50 and 20 kHz. As it is observed in Figure 31, db-4 mother wavelet in scales 1 and 2 and also HT are adversely influenced by sampling frequency. Although DWT with Haar mother wavelet is not severely affected by sampling frequency, it provides relatively higher fault location errors for most of the locations along the transmission line. The proposed technique is not affected by the sampling frequency as the ATs are estimated using linear regression (Figure 23, step 11), which fits a line to the dispersed damping factors (Figure 21(b)). Therefore,

the zero-crossing point (i.e., the estimated AT) is obtained regardless of the sampling frequency. The arriving waves initiated by a close-in fault are challenging to be detected for two major reasons: 1) the fault-induced traveling waves require to pass a long distance to reach the other end, therefore, they are mitigated more and their amplitudes and shapes become small and smooth, respectively. Thus, the arriving waves at two terminals are not similar and transient-detection techniques detect them with different errors leading to higher fault location errors. 2) As fault-induced traveling waves reflect at the close terminal and the fault location, they provide successive arriving waves with short intervals [114]. These successive arriving waves cannot be easily distinguished from one another or from the noise. This leads to less accurate AT detection, and consequently, higher fault location errors as shown in Figure 31.

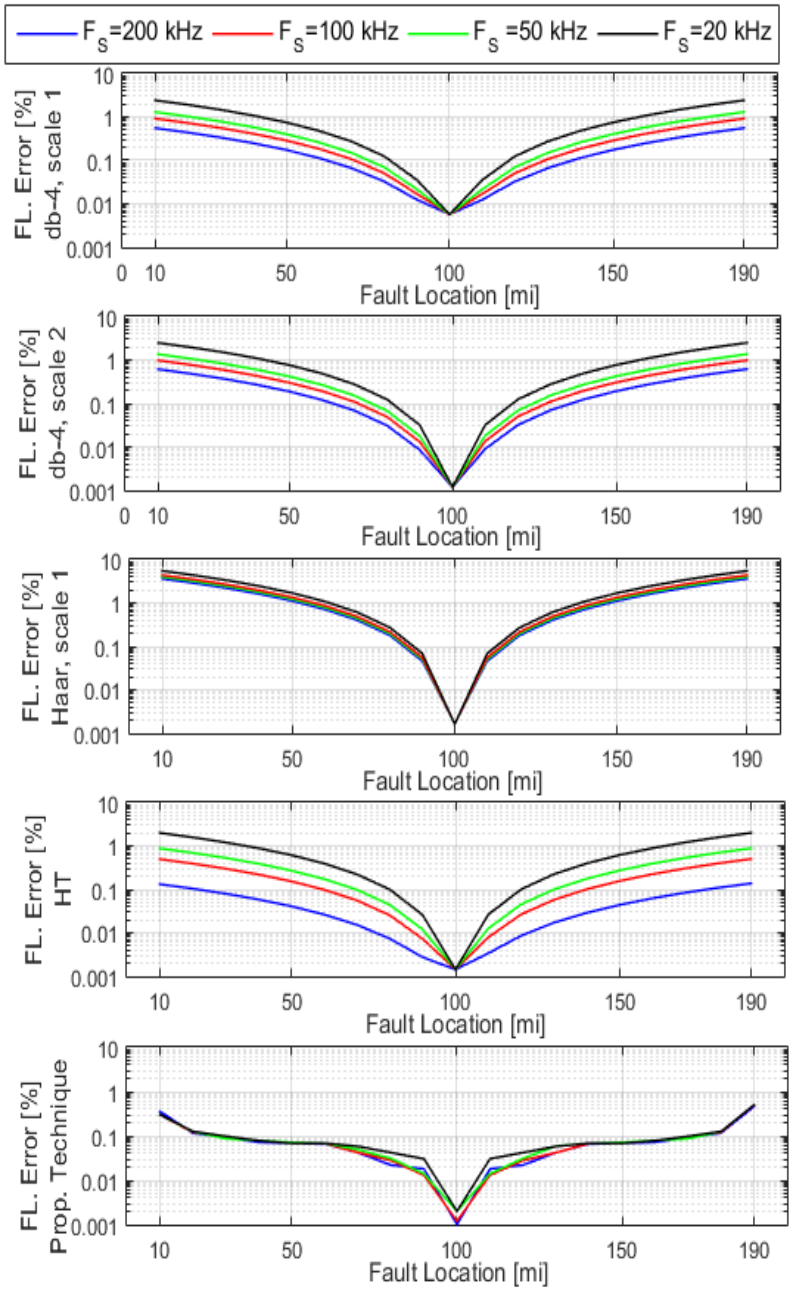

Figure 31. Fault location errors along the transmission line with different sampling frequencies, SLG fault, $Z_f = 1\ \Omega$, and $FIA = 90^0$.

4.2.9 Comparison

Table 17 compares the performance of different transient-detection techniques based on the simulation results. It can be observed that DWT-based technique with db-4 mother wavelet in scale 1 has a weak performance with respect to different influencing parameters.

However, db-4 mother wavelet in scale 2 is robust with respect to the measurement noises and FIA. Although Haar mother wavelet is robust with respect to the sampling frequency, its performance deteriorates with the measurement noise, non-ideal faults, and low FIAs. HT-based technique provides promising outcomes in comparison with DWT-based techniques, and generally results in less fault location errors. However, low sampling frequency detracts from the performance of HT-based technique. The proposed technique appears to be more robust against the influencing parameters compared to the existing AT-detection techniques.

Table 17. Comparison of the AT-detection methods

Technique	Noise	FIA	NIF(†)	F_s
db-4, scale 1	Weak	Weak	Weak	Weak
db-4, scale 2	Robust	Robust	Weak	Weak
Haar, scale 1	Rel. Rob. (‡)	Weak	Weak	Robust
HT	Robust	Robust	Robust	Weak
Prop. Tech.	Robust	Robust	Robust	Robust

(†) Non-ideal fault.

(‡) "Rel. Rob." indicates relatively robust.

4.3 Recursive Method for Traveling Wave Arrival Time Detection in Power Systems[5]

4.3.1 Introduction

According to the high computational capability required for STMPM-based AT-detection technique, a new AT-detection method is required for compensation of the mentioned shortcomings of the existing AT-detection methods. Therefore, in this chapter, a new method for wave AT-detection is proposed with the following merits: i) As the method is recursive, it is computationally efficient and proper to be implemented in on-site microprocessor-based fault locators, ii) the proposed method is relatively less affected by measurement noises and fault parameters compared to the existing methods, iii) it is independent of the arriving wave shape, therefore, the proposed method does not require pre-assessment of the fault-induced traveling waves as DWT-based methods require for the proper selection of the mother wavelet and scale.

The simulations are carried out using EMTP-RV and RSCAD (RTDS). The results are then analyzed using MATLAB for comparison of the proposed method with the existing AT-detection method (e.g., DWT with db-4 and Haar mother wavelets in different scales, HT, and STMPM) with respect to measurement noises, fault inception angle (FIA), sampling frequency, and non-ideal faults (NIF). According to the simulation results, the proposed method is less influenced by the mentioned parameters. Therefore, the performance of the traveling wave-based fault location methods depending on the first ATs will improve if the proposed method is used for wave AT detection (i.e., instead of DWT). However, the proposed method is capable of detecting the first AT, and consequently, it is

[5] Reprinted in line with copyright and author-rights for "Recursive Method for Traveling Wave Arrival Time Detection in Power Systems," [will be submitted] R. J. Hamidi and H. Livani.

only applicable to the fault location methods utilizing the first wave ATs.

4.3.2 Methodology

After the occurrence of a fault in power systems, transients (so called abrupt changes) in the relevant voltage and current measurements arise due to the fault-induced arriving waves. Then the corresponding voltages and currents start drifting from their previous trajectories, as shown in Figure 32. The objective of the proposed method is to detect the first traveling-wave ATs. The flowchart of the proposed method is shown in Figure 33, and the steps are described as follows,

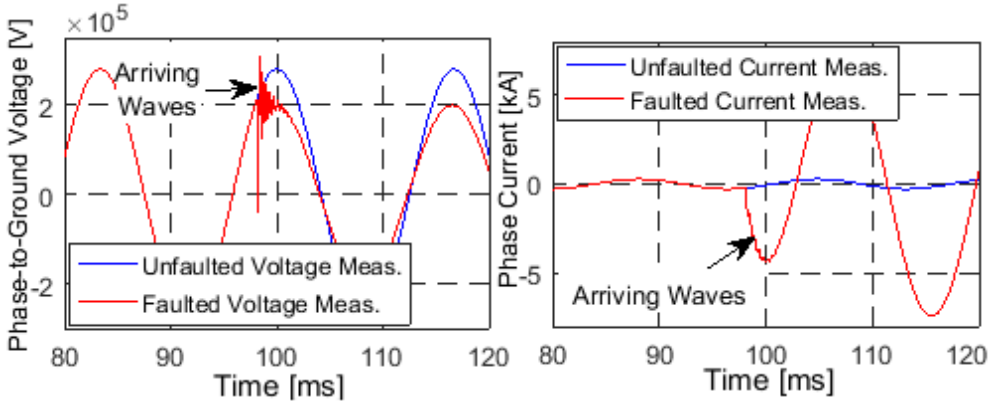

Figure 32. Typical aerial mode of voltage and current measurements with a high sampling rate after the occurrence of a fault. The voltage level is 230 kV and the sampling frequency is 200 kHz.

1. High Time-Resolution Measurements

The input to the proposed method is a stream of high time-resolution measurements in the form of $\tilde{z}_k = z_k^{true} + \gamma_k$, where $\tilde{z}_k$ is the k-th measured sample, z_k^{true} is the true value of the measurement, and $\gamma_k \sim \mathcal{N}(0, \sigma^2)$ is a zero-mean Gaussian noise with a variance of σ^2. Three-phase measurements are converted to modal components using Clarke's transformation as traveling wave-based fault location methods usually utilize one of the modes (commonly the aerial mode).

2. Parameter Estimation

Adaptive discrete Kalman filter (ADKF) is used for parameter estimation of the measured voltage samples. Therefore, the following formulations are considered to provide state variable representation of the sinusoidal voltages. The power system voltages may consist of several harmonics [127], therefore,

$$z_k^{true} = \sum_{h=1}^{N_h} A^h \sin(kh\omega_0 T_s + \phi^h) \tag{35}$$

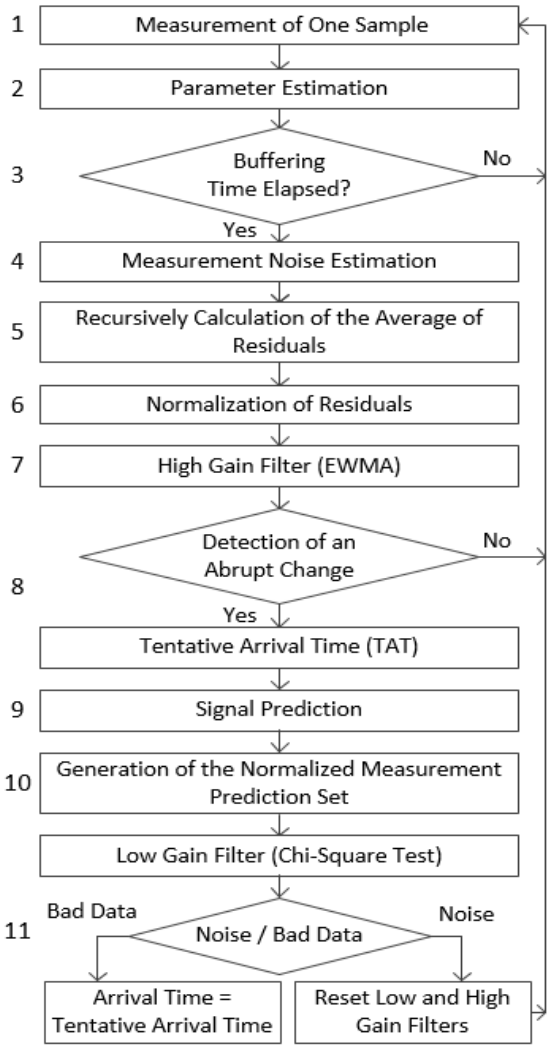

Figure 33. The flowchart of the proposed method.

where A^h and ϕ^h are the amplitude and phase angle of the h-th harmonic, respectively, k is the sample number, ω_0 is the power system angular frequency (i.e., $2\pi 60$ or $2\pi 50$), T_s is the sampling period, and N_h is the number of the harmonics existing in the power system. The extension of (35) is

$$z_k^{true} = \sum_{h=1}^{N_h} A^h \cos(\phi^h) \sin(kh\omega_0 T_s) + A^h \sin(\phi^h) \cos(kh\omega_0 T_s) \tag{36}$$

Applying the following definitions to (36), yields the state-variable representation of z_k^{true} as [131]

$$\begin{cases} x^{2h-1} = A^h \cos(\phi^h) \\ x^{2h} = A^h \sin(\phi^h) \\ a_k^{2h-1} = \sin(kh\omega_0 T_s) \\ a_k^{2h} = \cos(kh\omega_0 T_s) \end{cases}, \forall h = 1,2,\dots,N_h \tag{37}$$

where x denotes the states ($2N_h$ states are required for a signal with N_h harmonics) and a indicates coefficients. Therefore,

$$z_k^{true} = \sum_{h=1}^{N_h} a_k^{2h-1} x^{2h-1} + a_k^{2h} x^{2h} \tag{38}$$

and (38) can be shown in matrix form as

$$z_k^{true} = \boldsymbol{H}_K \boldsymbol{x}_k \tag{39}$$

where $\boldsymbol{H}_K = [a_k^1, a_k^2, \dots, a_k^{2N_h}]$ is the measurement coefficient vector and $\boldsymbol{x}_k = [x^1, x^2, \dots, x^{2N_h}]^T$ is the measurement state vector, and $(.)^T$ indicates matrix transposition. The state-space representation of the measurement is [128]

$$\begin{cases} \boldsymbol{x}_{k+1} = \boldsymbol{\phi}_k \boldsymbol{x}_k + \boldsymbol{w}_k \\ \tilde{z}_k = \boldsymbol{H}_k \boldsymbol{x}_k + \gamma_k \end{cases} \tag{40}$$

where $\boldsymbol{\phi}$ is the state transition matrix, $\boldsymbol{w}$ is the process noise vector, and γ is the measurement noise. The algorithm of ADKF is as follows

$$\begin{cases} \boldsymbol{G}_k = \boldsymbol{P}_k^- \boldsymbol{H}_k^T \left(\boldsymbol{H}_k \boldsymbol{P}_k^- \boldsymbol{H}_k^T + \hat{R}_k\right)^{-1} \\ \hat{\boldsymbol{x}}_k = \hat{\boldsymbol{x}}_k^- + \boldsymbol{G}_k (\tilde{z}_k - \boldsymbol{H}_k \hat{\boldsymbol{x}}_k^-) \\ \boldsymbol{P}_k = (\boldsymbol{I} - \boldsymbol{G}_k \boldsymbol{H}_k) \boldsymbol{P}_k^- \\ \hat{\boldsymbol{x}}_{k+1}^- = \boldsymbol{\phi}_k \hat{\boldsymbol{x}}_k \\ \boldsymbol{P}_{k+1}^- = \boldsymbol{\phi}_k \boldsymbol{P}_k \boldsymbol{\phi}_k^T + \boldsymbol{Q}_k \end{cases} \tag{41}$$

where $\boldsymbol{G}$, $\boldsymbol{P}$, $\boldsymbol{I}$, and $\boldsymbol{Q}$ are gain, error covariance, identity, and process noise covariance matrices, respectively. $(.)^-$ denotes prediction. It is realistic to assume $\boldsymbol{\phi}_k = \boldsymbol{I}, \boldsymbol{x}_{k+1} = \boldsymbol{x}_k, \forall k$ [131], considering slow-changing power system parameters and the short sampling time at a high sampling rate. Also, the process noise covariance is constant, $\boldsymbol{Q}_k = \boldsymbol{Q}_{k+1}, \forall k$, where $\boldsymbol{Q}_k = q\boldsymbol{I}$ and q is small, but not zero, (e.g., $q = 1$). $\hat{R}$ is the scalar estimated variance of the measurement noise since the measurement is a stream of samples.

3. Buffering Time

Since the measurement and states are gradually updated through Kalman filter, a short period (buffering time) is considered for Kalman-filter results to become reliable.

4. Measurement Noise Estimation

The measurement noise variance is inconsistent since the environmental noise and the measuring device accuracy are inconsistent [93]. Therefore, ADKF is utilized to update the measurement noise variance for more accurate estimation [129]. The measurement noise variance is updated as [132]

$$\begin{cases} \hat{R}_k = \hat{R}_0, \forall k T_s \le b \\ \hat{R}_k = \dfrac{1}{m} \sum_{i=1}^{m} r_{k-i}^2 - \boldsymbol{H}_k \boldsymbol{P}_k \boldsymbol{H}_k^T, \forall k T_s > b \end{cases} \tag{42}$$

where $\hat{R}_0$ is the initial estimation of the measurement noise variance, b is the buffering time (as the residuals are very large in the beginning, the initial estimated measurement

noise must be considered in the beginning of the process), and r is the residual (innovation sequence), which is the difference between the measured and estimated sample defined as

$$r_k = \tilde{z}_k - \boldsymbol{H}_k \hat{\boldsymbol{x}}_k \tag{43}$$

As (42) requires a long history of m residuals and a large number of summations, we formulated (42) in a recursive manner as follows (the formulation resulting to (44) is provided in Appendix D. 1)

$$\hat{R}_k = \Lambda\left(\hat{R}_{k-1} + \boldsymbol{H}_{k-1}\boldsymbol{P}_{k-1}\boldsymbol{H}_{k-1}^T\right) + (1-\Lambda)r_{k-1}^2 - \boldsymbol{H}_k\boldsymbol{P}_k\boldsymbol{H}_k^T \tag{44}$$

where $\Lambda \in (0,1)$ is the forgetting factor.

5. Recursive Average of Residuals

The normalized values of the residuals are necessary in the next steps, therefore, the average of the residuals is updated at each time step. In this regard, the exponential average method is utilized as a recursive method for calculation of the average of the residuals as follows [133] and [134] (Appendix D. 2).

$$\bar{r}_k = \lambda \bar{r}_{k-1} + (1-\lambda) r_k, \bar{r}_0 = 0 \tag{45}$$

where $\lambda \in (0,1)$ is the forgetting factor.

6. Normalization of the Residuals

The calculated residuals are normalized as follows

$$r_k^N = (r_k - \bar{r}_k)/\hat{R}_k \tag{46}$$

where r_k^N is the normalized value of the k-th residual.

7. High-Gain Control Chart (Filter)

The application of cumulative summation (CUSUM) filter as a random walk-based transient-detection method in power system protection is proposed in [135]. As the control charts can be designed to raise their sensitivity without increasing their errors [134], a two-

sided exponentially weighted moving average (EWMA) with a small forgetting factor is selected as a high-gain filter that is able to pinpoint the abrupt changes in a signal [133] and [134]. Two-sided EWMA is formulated as

$$\begin{cases} g_k = \max\{\psi g_{k-1} + (1-\psi) r_k^N, 0\}, g_k > T \rightarrow \ alarm \\ g'_k = \max\{\psi g'_{k-1} - (1-\psi) r_k^N, 0\}, g'_k > T \rightarrow \ alarm \end{cases} \quad (47)$$

where g_k and g'_k ($g_0, g'_0 = 0$) are EWMA outputs for rising and falling abrupt changes, respectively. $\psi \in (0,1)$ is the forgetting factor, and T is the threshold, which is selected based on the probability distribution function (PDF) of the normal Gaussian noise (Appendix D. 3).

8. Tentative Arrival Time

The selection of smaller values for ψ and T increases the gain of the EWMA control chart, enabling it to pinpoint the abrupt changes in normalized residuals (r_k^N). However, high-gain (short-window) control charts are prone to release false alarms due to the measurement noises. Therefore, the abrupt change in the normalized residuals (r_k^N) detected by EWMA is considered tentative as $EWMA\ alarm \rightarrow TAT = kT_s$, where TAT is the tentative traveling wave arrival time. The validity of TAT should be confirmed. In this regard, low-gain (long-window) filters can be utilized, which are less prone to release false alarms due to the measurement noises. However, they are not able to pinpoint the abrupt changes (i.e., the time resolution of a low-gain filter is low). As low-gain filters require a history of samples (i.e., in the proposed method r_k^N), Steps 9 and 10 in Figure 33 are considered to provide a sufficient data set for the low-gain filter.

9. Signal Prediction

For generation of a data set of r_k^N for the low-gain filter, the measured signal is predicted

for the next n samples based on the last estimated states ($\hat{\boldsymbol{x}}_k$) as [128]

$$Z_{pre} = \{\hat{z}_{k+1}^{-}, \hat{z}_{k+2}^{-}, \dots, \hat{z}_{k+n}^{-}\} \tag{48}$$

where Z_{pre} is the measurement prediction set. $\hat{z}_{k+i}^{-} = \boldsymbol{H}_{k+i}\hat{\boldsymbol{x}}_k, \forall i = 1,2, \dots, n$. The size of the set, n, should be properly selected for the low-gain filter.

10. Normalized Predicted Residuals

It takes time for the protection systems in high-voltage transmission grids to disconnect a faulty transmission line. Therefore, after the alarm of EWMA and before the protection systems clear the event, sampling continues, and a set of normalized residuals based on the predicted and measured samples is generated as

$$r_{pre}^{N} = \{r_{k+1}^{N}, r_{k+2}^{N}, \dots, r_{k+n}^{N}\} \tag{49}$$

where r_{pre}^{N} is the normalized predicted residual set,

$r_{k+i}^{N} = (r_{k+i}^{-} - \bar{r}_k)/\hat{R}_k, \forall i = 1, 2, \dots, n$, and

$r_{k+i}^{-} = (\tilde{z}_{k+i} - \hat{z}_{k+i}^{-}), \forall i = 1, 2, \dots, n.$

11. Low-Gain Filter

The normalized predicted residuals are in the form of $r_{k+i}^{N} = v_k + e_k$, where $v_K \sim \mathcal{N}(0,1)$ is the normalized measurement noise and e_k is the error in the k-th residual. Before the occurrence of a fault, $e_k \approx 0$, and the elements of r_{pre}^{N} belong to a normal Gaussian probability distribution function (PDF). However, when a fault occurs, the voltage starts drifting from its trajectory (Figure 32). Therefore, e starts becoming large ($e_k \gg 0$), and the elements of r_{pre}^{N} no longer belong to the normal Gaussian PDF. Hence, Chi-square testing technique is applicable as

$$Y = \sum_{i=1}^{n} (r_{k+i}^{N})^2 \tag{50}$$

where Y is an random variable with Chi-Square distribution with $(n-1)$ degrees of freedom.

$$\int_0^{y_t} \chi_{n-1}^2(\zeta)\, d\zeta = CPL \tag{51}$$

where χ_{n-1}^2 is the Chi-square PDF with $(n-1)$ degrees of freedom, ζ is the integration variable, CPL is confidence probability level, y_t is the largest acceptable value for Y and it is selected based on the predefined confidence level.

If $Y \geq y_t$, the elements of the normalized predicted residual set (r_{pre}^{N}) do not belong to the normal Gaussian PDF that implies $e \gg 0$. Therefore, a fault occurred and $AT = TAT$.

If $Y < y_t$ the elements of the normalized prediction residual set (r_{pre}^{N}) belong to the normal Gaussian PDF that implies $e \approx 0$. Therefore, EWMA released a false alarm due to the noises, and both low- and high-gain filters are reset and the procedure continues.

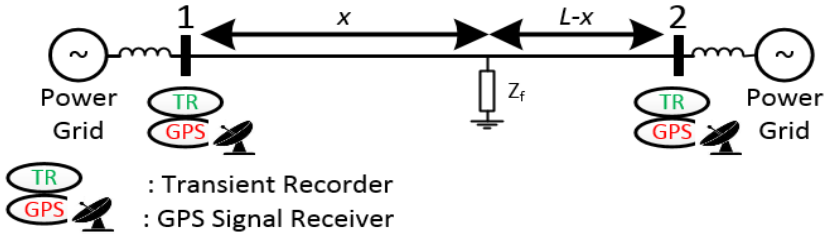

Figure 34. One-line schematic of the test case 1.

Table 18. Harmonic Contents in the Voltage

Harmonic Level [%]	V_{h2}	V_{h3}	V_{h5}	V_{h7}	V_{h9}	V_{h11}
	0.2	1	0.5	0.5	0.5	0.5
Harmonic Phase [^{0}]	ϕ_{h2}	ϕ_{h3}	ϕ_{h5}	ϕ_{h7}	ϕ_{h9}	ϕ_{h11}
	2	5	3	3	3	3

4.3.3 Case Study and Discussion

For evaluation of the proposed method, the test case and the fault location method based on [40] are considered. However, the proposed method is applicable to any traveling wave-based fault location method utilizing the first ATs (e.g., [20]). As Figure 34 depicts, there are transient recorders (TRs) equipped with GPS signal receivers (for time-synchronization of the measurements) at both ends of the transmission line. The transmission line length and voltage level are 100 mi and 350 kV, respectively. The voltage contains the harmonics given in Table 18 Transmission line is transposed with a topology based on [49]. The line is modeled using the frequency-dependent line model (EMTP FD model). Traveling wave velocity is 183486 mi/s in the aerial mode (i.e., wave traveling time (τ) is 545 μs in the aerial mode). The two-ended fault location method proposed in [40] is

$$CFL = (L - v\, t_d)/2 \tag{52}$$

where CFL [mi] is the calculated fault location, L [mi] is the transmission line length, $t_d = t_2 - t_1$ [s] in which t_1 and t_2 are the first ATs at Buses 1 and 2, respectively. v [mi/s] is the traveling-wave velocity. Fault location error is

$$err = |AFL - CFL|/L \times 100\% \tag{53}$$

where err [%] is the fault location error, AFL [mi] is the actual fault location, and L [mi] is the line length.

4.3.3.1 Illustrative Test Case

The following parameters are selected for ADKF: $\hat{R}_0 = 0.005 \times V_p$ where V_p is the peak voltage ($V_p = 350 \times \sqrt{2/3}$=285000 kV), $q = 1$, $b = 20$ ms (i.e., the first 4000 samples), $\Lambda = 0.99$, $\lambda = 0.99$, $\psi = 0.1$, $T = 1.77$ is selected for a confidence level of 95%, $n = 10$ is selected for a fast Chi-Square test. A single-line-to-ground (SLG) fault occurs in the

middle of the line at $t = 250$ ms. The voltage measurements contain zero-mean Gaussian noises with $\sigma^2 = 0.01 \times V_p$. The sampling frequency is $F_s = 200$ kHz. Figure 35(a) shows the measured and estimated values in the beginning of the procedure during the buffering time ($t < 20$ ms). It is noticed that the estimated signal quickly converges to the measured wave and the normalized residuals become small, as shown in Figure 35(b) since the sampling frequency is high and the states update at a high rate. After the buffering time, the estimated signal closely follows the true values of the measured samples and the normalized residuals deviate around zero, corresponding to the zero-mean Gaussian noise, as shown in Figures 35(c) and 35(d). Figure 35(e) depicts the arriving wave reaching Bus 1 at 250.275 μs. The arriving wave is shown in Figure 35(e). As Figure 35(f) shows, the residual size becomes greater than the threshold ($T = 1.77$), therefore, EWMA determines $TAT = 250.275$ ms. Then, the proposed

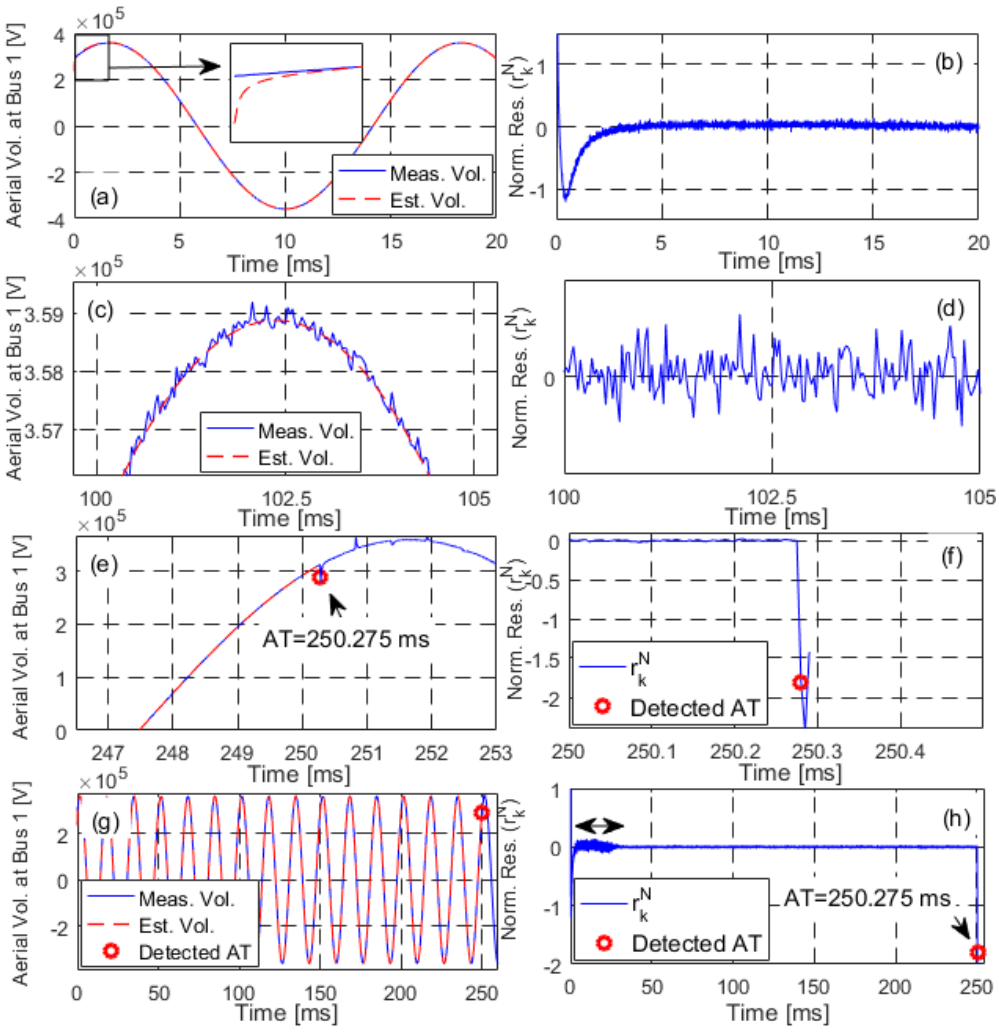

Figure 35. An SLG fault in the middle of the line at $t = 250$ ms and $Z_f = 1\ \Omega$. (a) and (b) the measured and estimated signals as well as the normalized residual in the beginning of the method. (c) and (d) the estimated and measured signals and also the normalized residuals after the buffering time. (e) and (f) the fault-induced arriving wave and the corresponding normalized residual that is larger than the EWMA threshold. (g) and (h) the entire measurement and normalized residuals during the procedure.

method generates predicted samples for the next 10 samples. Figure 35(f) shows the values of the normalized residuals close to the first fault-induced arriving wave. It is noticed that the normalized residuals are large after the occurrence of the fault. In the next step, Chi-square testing technique determines that the normalized predicted residual set (r_{pre}^N) does not belong to the normal Gaussian noise. Therefore, the low-gain filter confirms that the

arriving wave is induced by a fault, and $AT = TAT$ that equals 250.275 ms. Figures 35(g) and 35(h) illustrates the entire procedure. In Figure 35(h), the double-head arrow shows the larger values of normalized residuals in the first 20 ms of the procedure. Then, they start updating and becoming smaller, indicating that ADKF updates the normalized residuals that improves the efficiency of the proposed method.

4.3.3.2 Sensitivity Analysis Based on Test Case 1

The following subsections evaluate and compare the efficiency of the proposed method with that of the existing AT-detection methods based on Test Case 1.

Noise Sensitivity

The traveling waves mitigate along the lines and the environmental and measuring device noises skew the measurements. Therefore, the AT-detection methods must be able to detect the ATs of the traveling waves with low signal-to-noise rations (SNR). Accordingly, the noise sensitivity of the proposed method is compared to that of the existing AT-detection methods. An SLG fault occurs in the middle of the line, $F_S = 200$ kHz and the following parameters are selected to provide low SNR fault-induced arriving waves: $Z_f = 10\ \Omega$ and $FIA = 15^0$. Then, the fault location is estimated utilizing different AT-detection methods. The statistical results of the fault location errors based on one hundred Monte Carlo simulations (MCSs) are compared and shown in Figure 36. Box-plots show median, minimum, maximum, first quartile, and third quartile of the fault location errors. The fault location errors for the noise-contaminated measurements with $\sigma^2 = 0.0075V_p$, $\sigma^2 = 0.01V_p$, and $\sigma^2 = 0.0125V_p$ are shown in Figures 36 (a), 36(b) and 36(c), respectively. It is noticed that the proposed and STMPM methods are able to detect

the arriving waves with smaller SNRs, however, DWT with db-4 mother wavelet in scale 1 cannot accurately detect the arriving waves as Figures 36 (a) to 36(c) depict. DWT with db-4 mother wavelet in scale 1 is able to detect the arriving wave with a noise variance less than $0.01V_p$ as Figures 36 (a) and 36 (b) show. DWT with Harr mother wavelet and also HT are able to detect the ATs for a noise variance less than $0.0125V_p$.

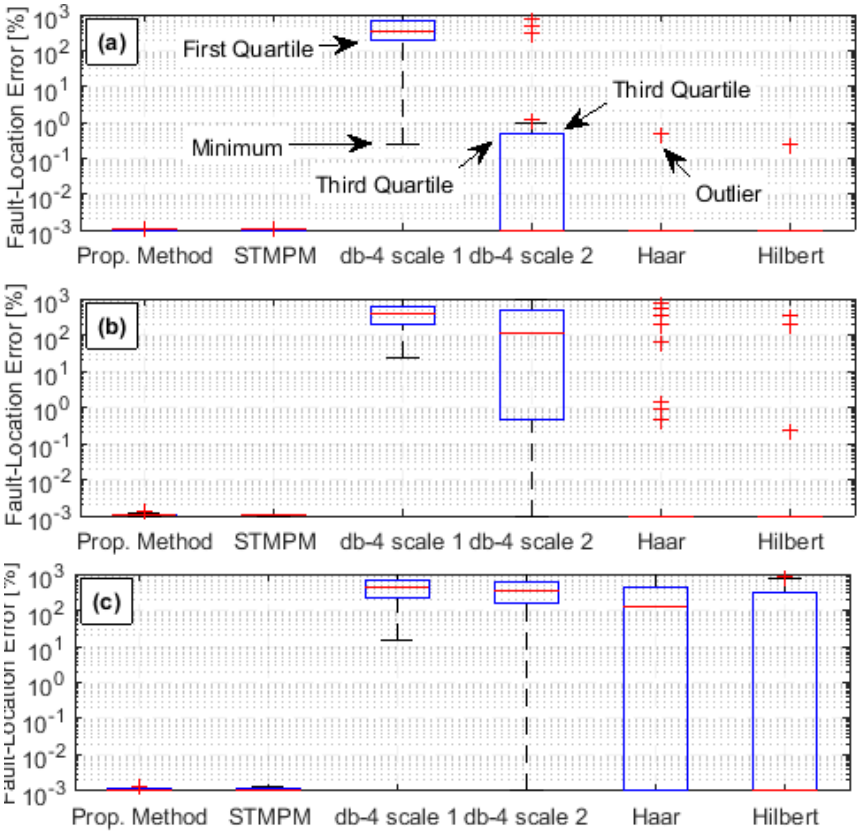

Figure 36. Fault location errors, SLG fault in the middle of the line, $Z_f = 10\ \Omega, FIA = 15^0$, and $F_S = 200$ kHz. (a) $\sigma^2 = 0.075V_p$. (b) $\sigma^2 = 0.01V_p$. (c) $\sigma^2 = 0.0125V_p$.

Fault Inception Angle (FIA)

As the faults with lower FIAs generate traveling waves with smaller amplitudes, the fault-induced waves are more vulnerable to disappear in the noise. Thus, the proposed method is compared to the existing methods with respect to FIA, and the results are

provided in Table 19. The fault location is in the middle of the line with $Z_f = 5\ \Omega$, $F_S = 200$ kHz, and the additional noises to all the measurements are $\mathcal{N}(0,0.01V_p)$. According to the results given in Table 19 and considering the shaded cells in Table 19, STMPM is able to locate the faults with $FIA \geq 5^0$ and the proposed method can find the location of the faults with $FIA \geq 6^0$. However, it is worth noting that if the attenuation factor (i.e., attenuation factor equals $e^{-\alpha L}$, where α is the attenuation constant [mi^{-1}], L is the line length [mi], [51]) of the transmission line is larger or in the case of higher measurement-noise levels, the location of faults with larger FIAs can be determined.

Table 19. The effect of FIA on fault location

Transient Detection Method	AFD [mi]	FIA [^{0}]				
		4	5	6	7	8
		Fault location Error [%]				
db-4, scale 1	1	N/A	N/A	N/A	N/A	N/A
	5	N/A	N/A	N/A	N/A	N/A
	50	N/A	N/A	N/A	N/A	1.120
db-4, scale 2	1	N/A	N/A	N/A	1.021	1.060
	5	N/A	N/A	1.109	1.015	1.001
	50	N/A	N/A	0.388	0.382	0.381
Haar, scale 1	1	N/A	N/A	N/A	N/A	N/A
	5	N/A	N/A	N/A	N/A	N/A
	50	N/A	N/A	N/A	N/A	N/A
HT	1	N/A	N/A	N/A	0.227	0.214
	5	N/A	N/A	0.188	0.168	0.160
	50	N/A	N/A	0.074	0.071	0.066
STMPM	1	N/A	0.960	0.420	0.404	0.395
	5	N/A	0.528	0.418	0.392	0.367
	50	N/A	0.271	0.216	0.201	0.194
The Proposed Method	1	N/A	N/A	0.455	0.404	0.395
	5	N/A	0.414	0.391	0.391	0.370
	50	N/A	0.223	0.188	0.176	0.191

N/A indicates that the method fails to detect the AT.

Sampling Frequency

Higher sampling frequencies provide higher time-resolution, therefore, ATs can be detected more precisely. However, the attenuation factors corresponding to higher frequency contents of the traveling waves increase, especially in the case of cables. Accordingly, the performance of AT-detection methods with respect to sampling frequency is studied and the results are provided in Figure 37. Two fault locations (i.e., 5 and 10 mi from Bus 1) are considered with $Z_f = 5\ \Omega$, $FIA = 90^0$, and the additional noises to all the measurements are $\mathcal{N}(0,0.01V_p)$. It is noticed that the performance of db-4 in scale 2 and HT methods is drastically affected by the sampling frequency. The performance of the proposed method relatively decreases as the sampling frequency decreases. However, STMPM, Haar, and db-4 in scale 1 are less affected by sampling frequency.

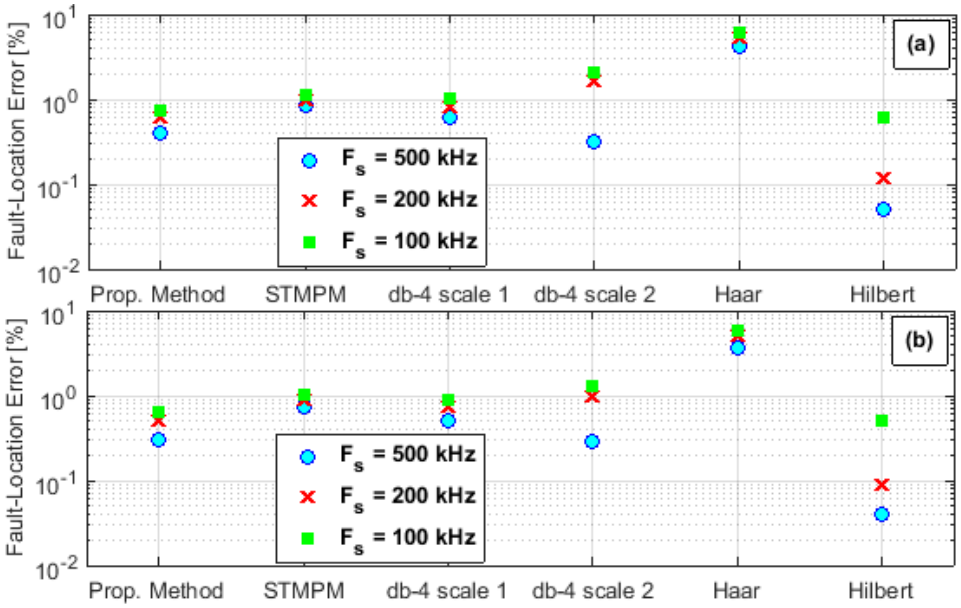

Figure 37. Fault location errors with respect to the sampling frequency. (a) The fault is 5 mi away from Bus 1 ($AFL = 5$ mi). (b) The fault is 10 mi away from Bus 1 ($AFL = 10$ mi).

Non-Ideal Faults

The fault impedance (shown with Z_f in Figure 34) with different X_f/R_f ratios generates

fault-induced traveling waves with different shapes affecting AT-detection methods [130]. It is assumed that an SLG fault occurs at 20 mi from Bus 1 with $FIA = 90^0$, $F_S = 200$ kHz, and the additional noises to all the measurements are $\mathcal{N}(0,0.01V_p)$. The absolute value of the fault impedance is constant ($Z_f = R_f + jX_f = 2\ \Omega$), however, X_f/R_f ratio is variant as: 0.05, 0.1, and 0.2. The shapes of the arriving waves at the Bus 1 are shown in Figure 38. It is noticed that the arriving-wave shapes are slightly different, therefore, AT-detection methods estimate different ATs. One hundred MCSs are run for each X_f/R_f ratio. The resulted fault location errors by different AT-detection methods are shown in Figure 39. It is noticed that the proposed method and STMPM are not affected by fault impedance.

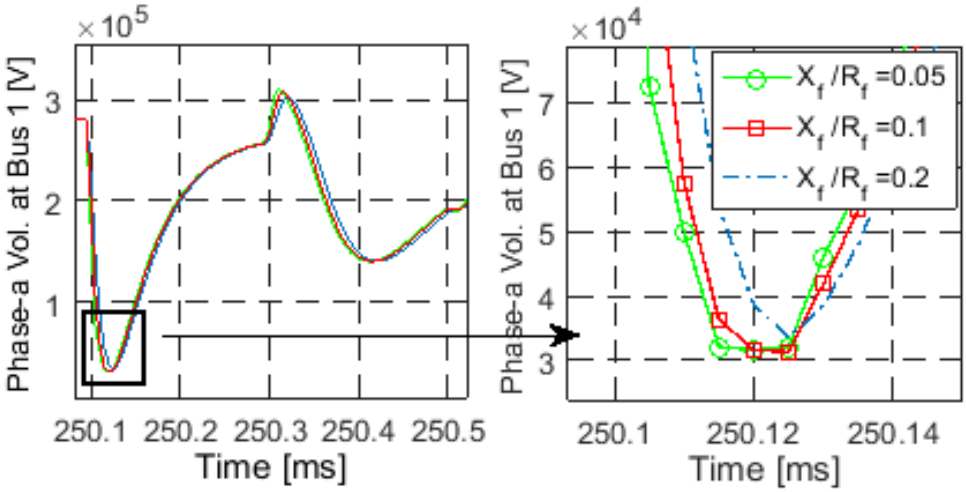

Figure 38. Fault-impedance effect on the arriving waves at Bus 1, $AFL = 10$ mi from Bus 1, $F_s = 200$ kHz, $Z_f = R_f + jX_f = 2\ \Omega$, and $FIA = 90^0$.

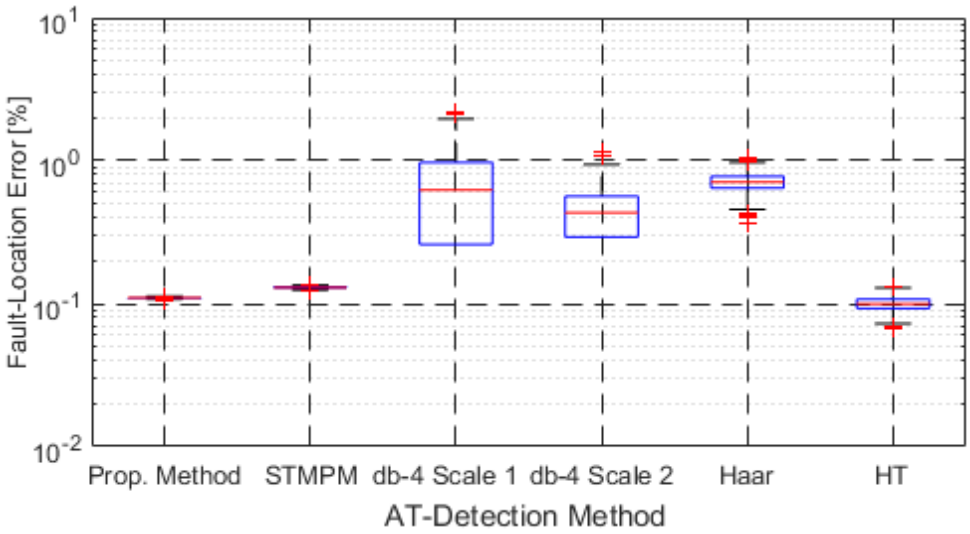

Figure 39. Fault-impedance effect on fault location errors.

4.3.3.3 Test Case 2: Real-Time Digital Simulation-Based

The schematic of the second test case is shown in Figure 40(a), which is developed in RSCAD to run by real-time digital simulator (RTDS) with an analog-to-digital (A/D)-in-the-loop. The system voltage and frequency are 230 kV and 60 Hz, respectively. The length of the overhead transmission line is 200 mi with the specification based on [136]. Traveling wave speed is 178430 mi/s [136]. Figure 40(b) shows the schematic of the used hardware. The digital-to-analog converter (DAC) of the RTDS produces signals based on the simulation results at 1 MHz. The data acquisition (DAQ), "IOTech DAQ/3000", is used to provide time-stamped measurements at a sampling rate up to 1 MHz [138], and the digitalized measurements are then processed in MATLAB.

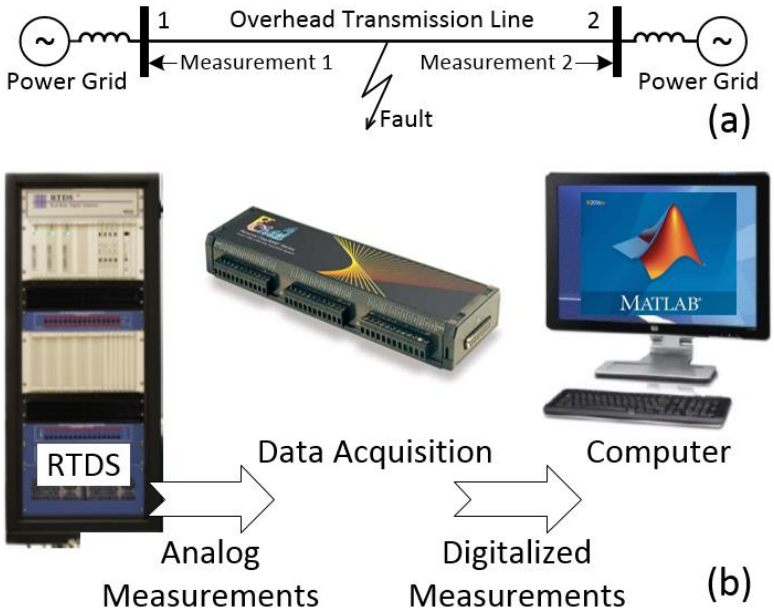

Figure 40. (a) the schematic of the test system in RSCAD. (b) The schematic of the hardware for converting the analog measurements to digital and sent to MATLAB.

Figure 41 shows the measurements and the detected ATs for a fault at 75 miles from Bus 1. Referring to (52) and (53), $t_1 = 74.945$ ms, $t_2 = 75.220$ ms, therefore, $t_d = 275$ µs, and the calculated fault location is $CFL = 75.465$, with $err = 0.23\%$. The measurement noise variance estimated by ADKF is almost 975 V (i.e., $0.0052V_p$). The fault location errors related to different locations of the faults are provided in Table 20.

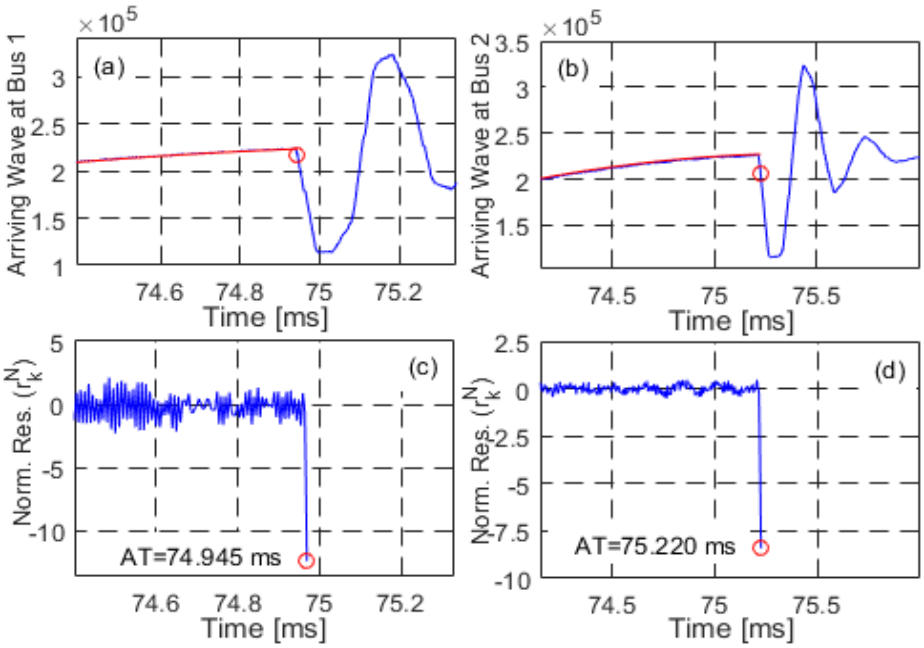

Figure 41. (a) and (b) show the arriving waves at Buses 1 and 2, respectively. (c) and (d) show the corresponding normalized residuals and the ATs.

Table 20. Average fault location errors in Test Case 2

	AFL [mi] from Bus 1					
		5	10	25	50	100
F_s = 200 kHz	Error [%]	0.87	0.81	0.32	0.26	≈0
F_s = 500 kHz	Error [%]	0.51	0.28	0.18	0.09	≈0

4.3.4 Comparison

The proposed method is also compared with STMPM in terms of computational burden since STMPM is more capable of detecting ATs, especially in low-SNR measurements. The total processing time is measured using MATLAB installed on a computer with an Intel(R) Xeon(R) E5420 processor and 16 GB of RAM. In both proposed and STMPM methods, calculation of the sine and cosine functions are fulfilled through lookup tables, and the divisions by constants are replaced with multiplication (i.e., ÷ 2 replaced with × 0.5, which runs drastically faster in microprocessors, [139]). The measurement shown in

Figure 35(g) for $0 \leq t \leq 100$ ms is considered. As $F_s = 200$ kHz, 100 ms is equal to 20000 samples. The total running times of STMPM and the proposed method for processing the 20000 samples are 244.539002 s and 0.088102 s (88.102 ms), respectively. This verifies the superior performance of the proposed method with respect to computational efficiency.

Table 21 qualitatively compares the performance of the existing and proposed AT-detection methods according to the simulation results. It is observed that the DWT-based method with db-4 mother wavelet in scale 1 provides weak performance with respect to the influencing parameters. However, db-4 mother wavelet in scale 2 is relatively robust against the measurement noises and FIA. The sampling frequency affects Haar mother wavelet, however, its performance deteriorates with the measurement noise, non-ideal faults, and low FIAs. The HT-based method provides promising results compared to DWT-based techniques, and generally results in less fault location errors. However, low sampling frequencies detract from its performance. STMPM-based methods are robust against all the influencing parameters. The proposed method results in reliable results against the influencing parameters, however, except for sampling frequency.

Table 21. Comparison of the AT-detection methods

Technique	Noise	FIA	NIF(†)	F_s
db-4, scale 1	Weak	Weak	Weak	Weak
db-4, scale 2	Robust	Robust	Weak	Weak
Haar, scale 1	Rel. Rob. (‡)	Weak	Weak	Robust
HT	Robust	Robust	Robust	Weak
STMPM.	Robust	Robust	Robust	Robust
The Proposed Method	Robust	Robust	Robust	Rel. Rob

(†) Non-ideal fault.
(‡) "Rel. Rob." is relatively robust.

4.3.5 Conclusion

This chapter proposes two new techniques for detection of traveling-wave arrival times

(ATs) in transmission systems. Fault location is one of the most important applications of the proposed technique. The existing methods for AT-detection are influenced by a number of parameters such as measurement noises, non-ideal faults, fault location, sampling frequency. Therefore, an AT-detection method less affected by the mentioned influencing parameters is required, that enhances traveling wave-based fault location methods in terms of accuracy. The proposed techniques in this chapter are based on 1) short-time matrix pencil method (STMPM) for optimal decomposition of a time-domain signal into time-indexed complex frequencies and 2) Kalman filter for estimation of the parameters of the measured signal. Considering the extensive simulation results, STMPM-based method is superior in detection of ATs in heavily noise-contaminate measurements. The Kalman filter-based method is computationally efficient and it is proper for implementation in microprocessors (for on-site and online applications). Both proposed methods are evaluated with respect to the abovementioned influencing parameters, and it is noticed that they both are superior to the existing AT-detection methods. Therefore, if the proposed AT-detection methods are used for estimation of ATs, the traveling wave-based fault location methods will improve. For example, in a large portion of the traveling wave-based fault location methods, discrete wavelet (DWT) transformation is utilized, however, as the studies in the dissertation show, replacement of DWT with each of the proposed methods mitigate the fault location errors.

Chapter 5. Conclusion and Future Work

A new algorithm based on fault-induced traveling waves is proposed in Chapter 2. The algorithm is applicable for fault location in hybrid multi-terminal transmission systems consisting of one onshore overhead line and multiple offshore submarine cables. The algorithm uses time-synchronized high-time-resolution transient voltage measurements at all of the ending terminals. The first traveling wave arrival times (ATs) are detected by observing the wavelet transformation coefficient squared (WTC^2) of mode 1 (i.e., aerial mode) voltages at all terminals. Through an over-determined set of linear equations (i.e., for noise reduction), the faulty segment and the exact location of the fault are estimated. According to the simulation results, the proposed algorithm is capable of calculating the fault location at a high accuracy level in comparison to the existing methods.

In Chapter 3, a new method for adaptive single-phase auto-reclosing (ASPAR) in transmission lines is proposed. The objective of the proposed ASPAR method is to raise the percentage of successful reclosing operations in the case of transient faults occurrence. In ASPAR, once a fault occurs, only the faulty phase is disconnected by the protection system (e.g., distance relays and circuit breakers). Then, the proposed method uses the power line carrier (PLC) signals for determination of the secondary arc extinction time. Once the clearance of the arc is recognized by the proposed method, the reclosing command is sent to the circuit breakers. The proposed method is considered as an additional application of PLC systems to enhance the resilience and stability of power systems. Based on extensive simulation results, the proposed method is not influenced by power system parameters and substantially increases the rate of successful reclosing actions.

In Chapter 4, a new accurate and robust traveling wave arrival time (AT)-detection is presented due to the shortcomings in the existing AT-detection methods. This chapter proposes two new techniques for detection of traveling-wave arrival times (ATs) in transmission systems. Fault location is one of the most important applications of the proposed technique. The existing methods for AT-detection are adversely influenced by a number of factors such as measurement noises, non-ideal faults, fault location, sampling frequency. Therefore, an AT-detection method less affected by the mentioned factors is required to enhance traveling wave-based fault location accuracy. The proposed techniques in Chapter 4 are based on 1) the short-time matrix pencil method (STMPM) for optimal decomposition of a time-domain signal into time-indexed complex frequencies and 2) a method based on adaptive discrete Kalman filter (ADKF) for parameter estimation of the high-frequency measurements, and high- and low-gain filters as exponentially weighted moving average (EWMA) and Chi-Square, respectively. The superiority of the proposed methods in detection of ATs in heavily noise-contaminate measurements is verified using extensive simulation results. ADKF-based method is also computationally more efficient compared to STMPM and it is proper for implementation in microprocessors or digital signal processors (DSPs) for on-site and online applications. The proposed methods are also evaluated with respect to the mentioned influencing parameters, and it is noticed that they are superior compared to the existing AT-detection methods. Therefore, if the proposed AT-detection methods are used for estimation of ATs, the traveling wave-based fault location methods will substantially improve.

As for the future work, the proposed traveling wave-based fault location method can be extended to bulk power systems, consisting of numerous overhead transmission lines with

known network topology. The effect of the substation components (e.g., power transformers and line traps) on the detection of traveling waves can be considered, and a novel wide-area monitoring system for observation of the fast transients in bulk power system can be developed.

The proposed ASPAR method can be implemented in microprocessors, this will enable us to verify the effectiveness of the proposed method using field measurements. However, if the real measurements are not available, the performance of the method can be evaluated using a real-time digital simulator hardware-in-the-loop (RTDS-HIL) testbed. The applicability of the proposed technique in distribution systems can also be a new research direction for the future for reduction of the unnecessary disconnections . Finally, the proposed AT-detection methods, can be implemented in microprocessors, to verify the superiority of the new techniques using RTDS-HIL or field measurements.

APPENDIX A

A. 1

The ability of the proposed method in detection of faulty segments is discussed in this appendix. The proposed method has no mathematically unidentifiable zones, i.e., the faulty segment can be identified for a fault close to the joint point or terminals, provided there is not any uncertainty in the measurements. In order to justify the above claim, if there is no uncertainty in arrival time detection, ε is removed from (1) and (4). Therefore, the arrival time differences are

$$\begin{cases} \tilde{t}_{mn} = (2\lambda - 1)\tau_m - \tau_n, \text{if } m\text{-}J \text{ is faulty} \\ \tilde{t}_{mn} = (1 - 2\lambda)\tau_n + \tau_m, \text{if } n\text{-}J \text{ is faulty} \\ \tilde{t}_{mn} = \tau_m - \tau_n, \text{neither } m\text{-}J \text{ nor } n\text{-}J \text{ is faulty} \end{cases} \tag{54}$$

Considering (6), the elements of the matrix $\boldsymbol{\Delta}$ are

$$\Delta_{mn} = |(2\lambda - 1)\tau_m - \tau_n - (\tau_m - \tau_n)|, \text{if } m\text{-}J \text{ is faulty}$$

$$\Delta_{mn} = \left|(1 - 2\lambda)\tau_n + \tau_m - (\tau_m - \tau_{n)}\right|, \text{if } n\text{-}J \text{ is faulty}$$

$$\Delta_{mn} = |\tau_m - \tau_n - (\tau_m - \tau_n)|, \text{neither } m\text{-}J \text{ nor } n\text{-}J \text{ is faulty}$$

This can be written as

$$\begin{cases} \Delta_{mn} = 2(\lambda - 1)\tau_m, \text{if } m\text{-}J \text{ is faulty} \\ \Delta_{mn} = 2(1 - \lambda)\tau_n, \text{if } n\text{-}J \text{ is faulty} \\ \Delta_{mn} = 0, \text{neither } m\text{-}J \text{ nor } n\text{-}J \text{ is faulty} \end{cases} \tag{55}$$

It is noticed from (55) that the elements of the matrix $\boldsymbol{\Delta}$ are a function of the wave traveling time in the faulty segment and the fault location. Then, the index of the column or row with $\Delta_{ij} > 0$ shows the faulty segment, unless $\lambda = 1$. Thus, the proposed method is not affected by the size of the system, the length of the segments, and the fault location.

However, measurement uncertainties slightly change the values of the elements of the

matrix $\boldsymbol{\Delta}$ (as shown in Table 1). Therefore, for a fault close to the joint point ($\lambda \to 1$), the elements of the matrix $\boldsymbol{\Delta}$ become close to one another, and the proposed method probably fails to identify the faulty segment, and subsequently, the fault location cannot be estimated.

A. 2

Remark: If $X_1 \sim \mathcal{N}(0, \sigma_1^2)$ and $X_2 \sim \mathcal{N}(0, \sigma_2^2)$ are two independent Gaussian random variables, then $(X_1 - X_2) \sim \mathcal{N}(0, \sigma_1^2 + \sigma_2^2)$. As the uncertainties in the arrival time measurements are related to TR noises, the elements of the diagonal weight matrix (i.e., $\boldsymbol{R}^{-1}$ in (10)) are selected according to the noise variances of TRs. Thus, $\boldsymbol{R}_{(N-1)\times(N-1)} = \text{diag}\left(\sigma_m^2 + \sigma_{c^*}^2\right), \forall m = 1,2,\dots,N, m \neq c^*$ and the solution to (10) is

$$\hat{\lambda} = 1/2 \left(\boldsymbol{\tau}^{*T} \boldsymbol{R}^{-1} \boldsymbol{\tau}^{*}\right)^{-1} \boldsymbol{\tau}^{*T} \boldsymbol{R}^{-1} \boldsymbol{b} \tag{56}$$

where the variables are defined in (10). It is noted that this estimator is not robust against outliers. A robust estimator based on least-absolute-value (LAV) may be used instead, as suggested in [20].

A. 3

Daubechies-4 (db-4) mother wavelet is selected for detection of the discontinuities induced by fault initiated waves because of its wide use in fault location literature and according to our investigations of different mother wavelets such as Haar and Symlet. A typical fault induced distortion in the voltage waveform, db-4 mother wavelet, and the resulted normalized WTC[2] are shown in Figures 42(a), 42(b), and 42(c), respectively. Since the sensitivity of the proposed method to FIA is studied, the effect of the FIA on the arriving waves is shown in Figure 33 (SLG fault in the middle of Segment 1-J, $Z_f = 1\ \Omega$, $F_S = 200$

kHz). Figure 43(a) shows the mode-1 voltage for a fault with $FIA \approx 90^0$ that generates large arriving waves. Figure 43(b) shows the mode-1 voltage for a fault with $FIA \approx 15^0$ that generates smaller arriving waves compared to the first one. Figure 43(c) shows the mode-1 voltage for a fault with $FIA \approx 0^0$ where no arriving wave is detected.

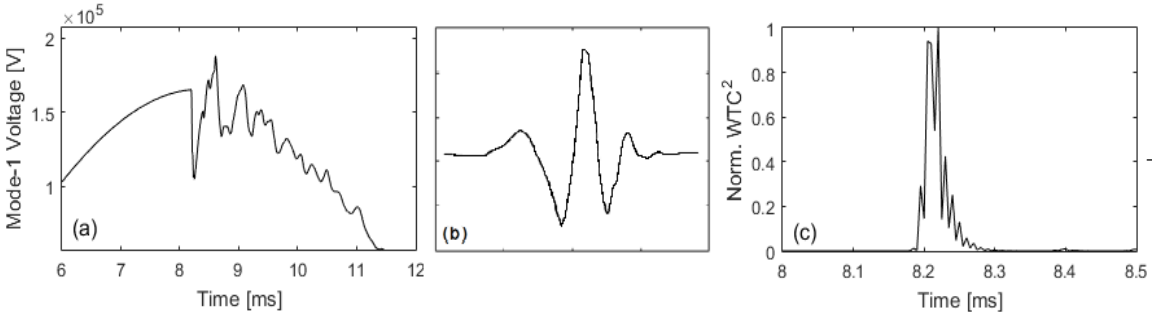

Figure 42. (a) Typical fault induced distortion in the voltage waveform. (b) db-4 mother wavelet. (c) The resulted normalized WTC^2.

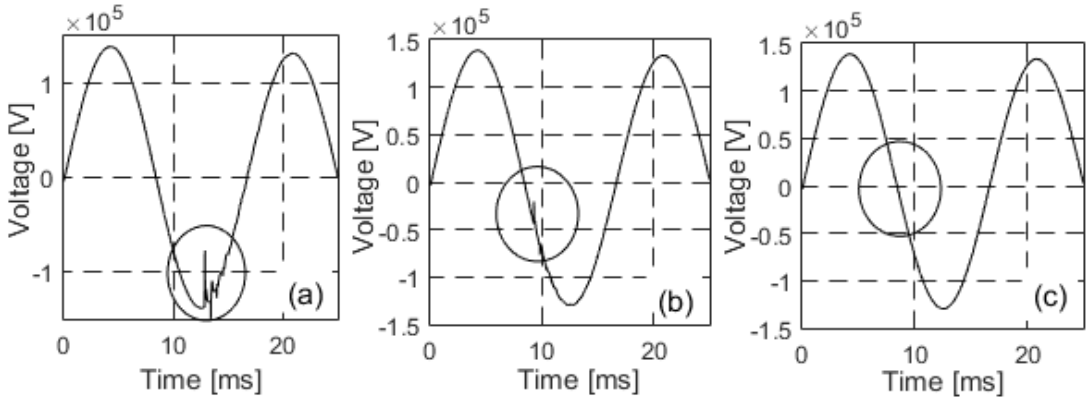

Figure 43. The relationship between FIA and arriving waves. (a) $FIA \approx 90^0$. (b) $FIA \approx 15^0$. (c) $FIA \approx 0^0$.

Appendix B

Referring to Figure 14, the following formulation results in (18). The travelling voltages and currents at the fault location are formulated as $\begin{cases} U_{PLC_1} + U_{PLC_r} = U_{PLC_2} \\ i_{PLC_1} + i_{PLC_r} = i_{PLC_2} + i_{PLC_{arc}} \end{cases}$, therefore, $\frac{U_{PLC_1}}{Z_c} - \frac{U_{PLC_r}}{Z_c} = \frac{U_{PLC_2}}{Z_c} + \frac{U_{PLC_2}}{Z_{arc}}$, replacing U_{PLC_r} with $U_{PLC_2} - U_{PLC_1}$, yields $\frac{U_{PLC_1}}{Z_c} - \frac{(U_{PLC_2} - U_{PLC_1})}{Z_c} = \frac{U_{PLC_2}}{Z_c} + \frac{U_{PLC_2}}{Z_{arc}}$, and finally $U_{PLC_2} = U_{PLC_1} \frac{2Z_{arc}}{2Z_{arc} + Z_c}$.

APPENDIX C

C. 1

Discrete-time Hilbert transform is composed of two parts as empirical mode decomposition (EMD) and Hilbert transform (HT). EMD is a sifting process that decomposes the signal $s(t)$ into intrinsic mode functions (IMFs) as [141]

$$s(t) = \sum_{i=1}^{n} c_i(t) + r_i(t) \tag{57}$$

where $c_i(t)$ and $r_i(t)$ are the IMF and residue, respectively. Each IMF is then converted to a series of instantaneous frequencies that is briefly formulated as

$$y_i(t) = \frac{1}{\pi}\int_{-\infty}^{+\infty} c_i(\tau)/(t-\tau)\, d\tau \tag{58}$$

$$\theta(t) = \tan^{-1}\big(y_i(t)/c_i(t)\big) \tag{59}$$

and instantaneous frequency, $f(t)$, is calculated as

$$f(t) = d\theta(t)/(2\pi\, dt) \tag{60}$$

C. 2

The efficiency of the proposed AT-detection technique is evaluated on a 170-kV, 60-Hz hybrid three-terminal transmission system that is shown in Figure 44. The lead phase sheaths of the cables are fully cross-bounded, and the steel wire armour is continuously grounded. The overhead transmission line is fully transposed to increase its attenuation factor [8]. The sampling frequency is 200 kHz. Referring to Figure 44, the lengths of Segments A-J, B-J and C-J are 50, 35, and 20 miles, respectively. Zero-mean Gaussian noises with variances of $0.01V_p$ ($0.01 \times 138800 = 1388$) are added to the three-phase transient voltage measurements, and solid SLG faults with FIAs of 15^0 are simulated.

Traveling wave velocities in the overhead line and the cables are 181817 and 119048 mi/s in the aerial mode, respectively. The fault location method described in [102] based on STMPM (instead of DWT) is used for calculation of fault locations. The fault location errors are provided in Table 22. As the lengths of the segments are relatively short, considering (31), the fault location errors are larger compared to the errors in the literature [52] and [61].

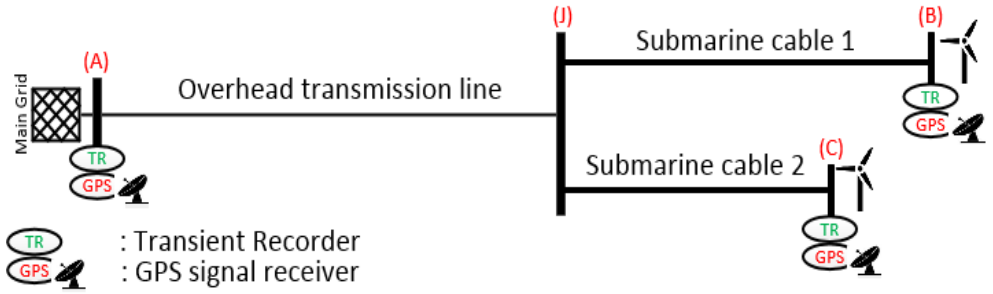

Figure 44. One-line diagram of the hybrid three-terminal test case.

Table 22. Fault location accuracy

Faulted Segment	AFD	Err [%]	Faulted Segment	AFD	Err. [%]
A-J	1 mi from A	0.372	B-J	20 mi from B	0.487
A-J	20 mi from A	0.021	B-J	34 mi from B	1.012
A-J	30 mi from A	0.022	C-J	1 mi from C	1.120
A-J	44 mi from A	0.883	C-J	5 mi from C	0.751
B-J	1 mi from B	0.944	C-J	10 mi from C	0.704
B-J	10 mi from B	0.550	C-J	19 mi from C	1.182

APPENDIX D

D. 1

Recursive Measurement Noise Estimation: For any given $(k-1)$-th sample, r_{k-1} is calculated and saved for the next step, and (42) is written as follows

$$\hat{R}_{k-1} = \frac{1}{m}\underbrace{\sum_{i=1}^{m} r_{(k-1)-i}^2}_{A_{k-1}} - \underbrace{\boldsymbol{H}_{k-1}\boldsymbol{P}_{k-1}\boldsymbol{H}_{k-1}^T}_{B_{k-1}} \tag{61}$$

we replaced A_{k-1} with

$$m\left(\hat{R}_{k-1} + B_{k-1}\right) = \underbrace{\sum_{i=1}^{m} r_{(k-1)-i}^2}_{A_{k-1}} \tag{62}$$

once the next sample, k-th, is measured, the corresponding residual is calculated and saved, and r_{k-1} (saved in the previous step) can be added to both sides of (62) as

$$m\left(\hat{R}_{k-1} + B_{k-1}\right) + r_{k-1}^2 = \underbrace{A_{k-1} + r_{k-1}^2}_{rhs} \tag{63}$$

where $rhs = \sum_{i=1}^{m+1} r_{(k)-i}^2$ and the window length, m, increases by 1. (42) for the k-th sample is

$$\hat{R}_k = \frac{1}{m+1}\underbrace{\sum_{i=1}^{m+1} r_{(k)-i}^2}_{A_k} - \underbrace{\boldsymbol{H}_k\boldsymbol{P}_k\boldsymbol{H}_k^T}_{B_k} \tag{64}$$

A_k is replaced with rhs that leads to

$$\hat{R}_k = \frac{1}{m+1} rhs - \underbrace{\boldsymbol{H}_k\boldsymbol{P}_k\boldsymbol{H}_k^T}_{B_k} \tag{65}$$

Referring to (63), (65) can be written as

$$\hat{R}_k = \frac{m}{m+1}\left(\hat{R}_{k-1} + B_{k-1}\right) + \frac{r_{k-1}^2}{m+1} - \underbrace{\boldsymbol{H}_k\boldsymbol{P}_k\boldsymbol{H}_k^T}_{B_k} \tag{66}$$

by defining $\Lambda = \frac{m}{m+1}$,

$$\hat{R}_k = \Lambda\left(\hat{R}_{k-1} + B_{k-1}\right) + (1-\Lambda)r_{k-1}^2 - \underbrace{\boldsymbol{H}_k \boldsymbol{P}_k \boldsymbol{H}_k^T}_{B_k} \tag{67}$$

or equivalently,

$$\hat{R}_k = \Lambda\left(\hat{R}_{k-1} + \boldsymbol{H}_{k-1}\boldsymbol{P}_{k-1}\boldsymbol{H}_{k-1}^T\right) + (1-\Lambda)r_{k-1}^2 - \boldsymbol{H}_k \boldsymbol{P}_k \boldsymbol{H}_k^T \tag{68}$$

which is identical to (44).

D. 2

Recursive Average of Residuals: the fixed forgetting factor mean is defined as [133], [134]

$$\bar{r}_k = \frac{1}{\omega}\sum_{i=1}^{k} \lambda^{k-i} r_i \tag{69}$$

where $\omega = \frac{1}{1-\lambda}, k \to \infty, \lambda \in (0,1)$. Referring to (45),

$\bar{r}_1 = (1-\lambda)r_1,$

$\bar{r}_2 = \lambda(1-\lambda)r_1 + (1-\lambda)r_2,$

$\bar{r}_3 = \lambda^2(1-\lambda)r_1 + \lambda(1-\lambda)r_2 + (1-\lambda)r_3, \ldots,$

$\bar{r}_k = \lambda^{k-1}(1-\lambda)\bar{r}_{k-1} + \lambda^{k-2}(1-\lambda)\bar{r}_{k-2} + \cdots + (1-\lambda)r_k.$

Therefore, (45) generates (68) in a recursive manner.

D. 3

EWMA threshold: Referring to (47), and considering that $r_k^N \sim \mathcal{N}(0,1)$, then

$g_1, g_1' \sim \mathcal{N}(0, (1-\psi)^2),$

$g_2, g_2' \sim \mathcal{N}(0, \psi^2(1-\psi)^2 + (1-\psi)^2),$

$g_3, g_3' \sim \mathcal{N}(0, \psi^4(1-\psi)^2 + \psi^2(1-\psi)^2 + (1-\psi)^2), \ldots,$

$g_k, g_k' \sim \mathcal{N}(0, \sum_{j=1}^{k} \psi^{2(j-1)}(1-\psi)^2).$

Based on the properties of geometric series, and $\psi < 1$, $g_k, g'_k \sim \mathcal{N}\left(0, \frac{(1-\psi)^2}{1-\psi^2}\right), \forall k \gg 1$ [142]. Therefore, using the normal Gaussian PDF, the value of the threshold T can be selected. For example, assuming $\psi = 0.1$, $g_k, g'_k \sim \mathcal{N}(0,9/11)$. Thus, a threshold of $T = 1.77$ indicates that r_k^N is a Gaussian noise for 95% and the released alarm is false for 5%.

References

[1] P. W. Saucer, M. A. Pai, "Power system dynamics and stability," Prentice Hall, New Jersey, USA, 1st Ed., 1997.

[2] L. Van Der Sluis, "Transients in power systems," John Willey and Sons Ltd., Sussex, England, 5th Ed., 2001.

[3] R. Jalilzadeh Hamidi, H. Livani, S. H. Hosseinian, and G. B. Gharehpetian, "Distributed cooperative control system for smart microgrids," Electric Power System Research, vol. 130, pp. 241-250, Jan. 2016.

[4] R. Jalilzadeh Hamidi, H. Livani, "Myopic real-time decentralized charging management of plug-in hybrid electric vehicles," Electric Power System Research, vol. 143, pp. 522-543, Feb. 2017.

[5] R. Ruedenberg, "Transient performance of electric power systems: phenomena in lumped networks," McGraw-Hill, NewYork, 1950.

[6] H. Peterson, "Transients in power systems," John Willey and Sons Ltd, New York, USA, 1951.

[7] Saša D. Milić, "Comprehensive concept of diagnostic centre in electrical power systems," Mediterranean Conference on Power Generation, Transmission, Distribution and Energy Conversion (MedPower 2016), Belgrade, Serbia, pp. 1-7, Nov. 2016.

[8] R. Jalilzadeh Hamidi, S. H. Hosseinian, and S. H. H. Sadeghi, and Z. Qu, "A novel approach to utilize PLC to detect corroded and eroded segments of power transmission lines," IEEE Trans. Power Delivery, vol. 30, no. 2, pp. 746-754, 2015.

[9] M. Shafiq, "Design and implementation of partial discharge measurement sensors for on-line condition assessment of power distribution system components," Aalto University, Doctoral Dissertation, Oct. 2014.

[10] W. Chen, S. Gu, J. He, and Bin Yin, "Development of arc-guided protection devices against lightning breakage of covered conductors on distribution lines," IEEE Trans., Power Delivery, vol. 25, no. 1, pp. 196-205, Jan. 2010.

[11] J. He, S. Gu, S. Chen, R. Zeng, and W. Chen, "Discussion on measures against lightning breakage of covered conductors on distribution lines" IEEE Trans., Power Delivery, vol. 23, no. 2, Apr. 2008.

[12] J. Zhou, B. Ayhan, C. Kwan, S. Liang, and W. Lee, "High-performance arcing-fault location in distribution networks," IEEE Trans., Industry Applications, vol. 48, no. 3, pp. 1107-1114, May 2012.

[13] H. Chen, P. D. Seul Assala, Y. Cai, and P. Yang, "Intelligent transient overvoltages location in distribution systems using wavelet packet decomposition and general regression neural networks," IEEE Trans., Industrial Informatics, vol. 12, no. 5, pp. 1726-1735, Oct. 2016.
[14] Y. Hong and b. Chen, "Locating switched capacitor using wavelet transform and hybrid principal component analysis network," IEEE Trans., Power Delivery, vol. 22, no. 2, pp. 1145-1152, Apr. 2007.
[15] H. Khani, M. Moallem, S. Sadri, and M. Dolatshahi, "A new method for online determination of the location of switched capacitor banks in distribution systems," IEEE Trans., Power Delivery, vol. 26, no. 1, pp. 341-351, Jan. 2011.
[16] C. Yao, X. Zhang, L. Du, Y. Mi, and C. Sun, "Online lightning and internal overvoltages monitoring system in 10 kV distribution networks," European Transactions on Electrical Power, vol. 21, pp. 282-292, Jun. 2010.
[17] G. A. Hussain, M. Shafiq, and M. Lehtonen, "Predicting arc faults in distribution switchgears," 17th International Scientific Conference on Electric Power Engineering (EPE), pp. 1-6, 2016.
[18] R. Rajvanshi and T. Hawkins, Value of Insulated Bus Bars in Reducing Arcing Fault Duration in Low Voltage Systems, 2016 IEEE-IAS/PCA Cement Industry Technical Conference, Dallas, Texas, pp. 1-7, May, 2016.
[19] M. Khoshdeli, I. Niazazari, R. J. Hamidi, H. Livani, and B. Parvin, "Wide-area electromagnetic transient events (EMTE) classification in transmission grids," IEEE PES GM. Chicago, Illinoise, USA, Jul. 2017, to be appeared.
[20] M. Korkali and A. Abur, "Robust fault location using least-absolute-value estimator," IEEE Trans. Power Systems, vol. 28, no. 4, pp. 4384-4392, Nov. 2013.
[21] M Majidi and H Javadi, "Feasible Installation of Transmission Line Surge Arresters to Decrease Lightning Transient Over-Voltages in Power Systems," International Review of Electrical Engineering (IREE), vol. 6, no. 5, pp. 2666-2674, Sep. 2011.
[22] V. Sarfi and V. Hemmati, "Simulation of partial discharge in closely coupled cavities embedded in solid dielectrics by finite element method. "International Conference on High Voltage Engineering and Application (ICHVE), Poznan, Poland, pp. 1-4. IEEE, 2014.
[23] V. Sarfi, S. Mohajeryami, and A. Majzoobi, "Estimation of water content in a power transformer using moisture dynamic measurement of its oil" IET Trans. High Voltage, vol. 2, no. 1, pp. 11–16, 2017.
[24] Available online: https://www.unr.edu/Documents/graduate-school/dissertation-and-thesis-submission-requirements.pdf
[25] ABB Grid Systems - Offshore Wind Connections. (2003, Nov.). ABB Goes Offshore Products and Solutions for Offshore Wind Energy. ABB, Sweden, [Online]. available: www.abb.com/windpower
[26] C. F. Jensen, C. L. Bak, and U. S. Gudmundsdottir, "Online travelling wave-based fault location on crossbonded ac cables in underground transmission systems," in Proc. CIGRE, Paris, 2014.
[27] Nexans Deutschland Industries GmbH – Energy Networks. (2008, May). Submarine Power Cables. Nexans, Hannover, Germany, [Online]. available: www.nexans.de
[28] IEEE Guide for Fault Location Techniques on Shielded Power Cable Systems, IEEE Standard 1234, 2007.
[29] IEEE Guide for Determining Fault Location on AC Transmission and Distribution Lines, IEEE Standard C37.114, 2004.
[30] D. A. Tziouvaras, "Protection of high-voltage ac cables, in power systems," in Proc. Advanced Metering, Protection, Control, Communication, and Distributed Resources, Clemson, SC, Mar. 2006, pp. 316–328.

[31] C. F. Jensen, "Fault in transmission cables and current fault location methods," in Online Location of Faults on AC Cables in Underground Transmission Systems, Switzerland: Springer, 2014, ch 2, pp. 7-18.
[32] S. W. Min, J. K. Park, S. R. Nam, S. H. Kang, and W. K. Park, "Fault location algorithm for underground power cables using analytical method," in Proc. CIGRE, Paris, 2006.
[33] S. W. Min, S. R. Nam, S. H. Kang, and J. K. Park, "Fault location algorithm for cross-bonded cables using the singularity of the sheath impedance matrix," Electrical Engineering, vol. 89, no. 7, pp. 525–533, Jul. 2007.
[34] X. Yang, M. S. Choi, S. J. Lee, C. W. Ten, and S. I. Lim, "Fault location for underground power cable using distributed parameter approach," IEEE Trans. Power Systems, vol. 23, no. 4, pp. 1809-1816, Nov. 2008.
[35] Z. Xu and T. S. Sidhu, "Fault location method based on single-end measurements for underground cables," IEEE Trans. Power Delivery, vol. 26, no. 4, pp. 2845-2854, Oct. 2011.
[36] D. S. Gazzana, G. D. Ferreira, A. S. Bretas, A. L. Bettiol, A. Carniato, L. F. N. Passos, A. H. Ferreira, and J. E. M. Silva, "An integrated technique for fault location and section identification in distribution systems," Electric Power System Research, vol. 115, pp. 65-73, 2014.
[37] S. L. Zimath, M. A. Ramos, J. S. Filho, J. M. Beck, and N. Mueller, "Traveling wave-based fault location experiences," in Proc. Protective Relay Eng., College Station, TX, pp. 1-7, Mar.-Apr. 2010.
[38] L. Coffeen, J. McBride, and D. Cantrelle, "Initial development of EHV bus transient voltage measurement: an addition to on-line transformer FRA," in Proc. EPRI Substation Equipment Diagnostics, Orlando, FL., Mar. 2008.
[39] A. O. Ibe and B. J. Cory, "A travelling wave-based fault locator for two- and three-terminal networks," IEEE Trans. Power Delivery, vol. 1, no. 2, pp. 283-288, Apr. 1986.
[40] F. H. Magnago and A. Abur, "Fault location using wavelets," IEEE Trans. Power Delivery, vol. 13, no. 4, pp. 1475-1480, Oct. 1998.
[41] C. Y. Evrenosoglu and A. Abur, "Travelling wave based fault location for teed circuits," IEEE Trans. Power Delivery, vol. 20, no. 2, pp. 1115-1121, Apr. 2005.
[42] R. Jalilzadeh Hamidi, H. Khodabandehlou, H. Livani, and M. Sami Fadali, "Application of distributed compressive sensing to power system state estimation," NAPS, Charlotte, North Carolina, pp. 1-6, Oct. 2015.
[43] Z. Yongli and F. Xinqiao, "Fault location scheme for a multi-terminal transmission line based on current traveling waves," Electrical Power and Energy Systems, vol. 53, pp. 367-374, Dec. 2013.
[44] H. Livani and C. Y. Evrenosoglu, "A traveling wave based single-ended fault location algorithm using DWT for overhead lines combined with underground cables," in Proc. IEEE PES GM, Minneapolis, MN., pp.1-6, Jul. 2010.
[45] H. Livani and C. Y. Evrenosoglu, "A machine learning and wavelet-based fault location method for hybrid transmission lines," IEEE Trans. Smart Grid, vol. 5, no. 1, pp. 51-59, Jan. 2014.
[46] M. Majidi, A. Arabali, and M. Etezadi-Amoli, "Fault location in distribution networks by compressive sensing," IEEE Trans. Power Delivery, vol. 30, no. 4, pp. 1761 – 1769, Aug. 2015.
[47] C. F. Jensen, O. M. K. K. Nanayakkara, A. D. Rajapakse, U. S. Gudmundsdottir, and C. L. Bak, "Online fault location on AC cables in underground transmission systems using sheath currents," Electric Power Systems Research, vol. 115, pp. 74-79, Oct. 2014.
[48] R. Jalilzadeh Hamidi and H. Livani, "A travelling wave-based fault location method for hybrid three-terminal circuits," in Proc. IEEE PES GM, Denver, CO., pp. 1-5, Jul. 2015.

[49] EMTP-RV 3, Line Data Example, [Online]. Available: http://emtp.com/content/download
[50] Nexans. (2011, Oct.). 60-500 kV High Voltage Underground Power Cables XLPE Insulated Cables. Nexans, Paris, France, [Online]. available: http://www.nexans.com
[51] H. W. Dommel, "Overhead transmission lines," in EMTP Theory Book, USA: BPA, 1995, ch 4, pp. 64-149.
[52] X. Lin, F. Zhao, G. Wu, Z. Li, and H. Weng, "Universal wavefront positioning correction method on traveling-wave-based fault location algorithms," IEEE Trans. Power Delivery, vol. 27, no. 3, pp. 1601-1610, Jul. 2012.
[53] L. U. Iurinic, R. G. Ferraz, A. S. Bretas, A. L. Bettiol, L. F. N. dos Passos, A. Carniato, I. K. Khairalla, R. Z. Homma, and A. Baader, "Fault induced transient detection in power systems: an adaptive approach considering noisy environment," in Proc. IPST, Cavtat, Croatia, Jun. 2015.
[54] K. R. Caino de Oliveira, R. H. Salim, A. Shuck Jr., and A. S. Bretas, "Faulted branch identification on power distribution systems under noisy environment," in Proc. IPST, Kyoto, Japan, Jun. 2009.
[55] V. De Andrade and E. Sorrentino, "Typical expected values of the fault resistance in power systems," in Proc. T&D-LA, Sao Paulo, Brazil, pp. 602-609, Nov. 2010.
[56] Short-Circuit Currents in Three-Phase A.C. Systems –Part 3: Currents during Two Separate Simultaneous Line-to-Earth Short Circuits and Partial Short-Circuit Currents Flowing through Earth, IEC 60909-3, Second Edition, Sep. 2003.
[57] T. Shindo and T. Suzuki, "A new calculation method of breakdown voltage-time characteristics of long air gaps," IEEE Trans. Power Apparatus and Systems, vol. PAS-104, no. 6, pp. 1556-1563, Jun. 1985.
[58] X. Zhou, S. Chen, H. Wang, R. Zeng, C. Zhuang, J. Yu, and Y. Ding, "Experiment on leader propagation characteristics of air gaps in UHVDC transmission towers under positive switching impulse voltages," CSEE Journal of Power and Energy Systems, vol. 1, no. 3, pp. 42-48, Sep. 2015.
[59] EMTP-RV 3, Air Gap Leader Example, [Online]. Available: http://emtp.com/content/download
[60] M. Kizilcay and T. Pniok, "Digital simulation of fault arcs in power systems," ETEP, vol. 1, no. 1, pp. 55-60, Jan. 1991.
[61] M. Majidi, M. Etezadi-Amoli, and M. Sami-Fadali, "A sparse-data-driven approach for fault location in transmission networks," IEEE Trans. Smart Grid, vol. PP, no. 99, pp. 1-9, Nov. 2015.
[62] J. J. Guo and S. A. Boggs, "High frequency signal propagation in solid dielectric tape shielded power cables," IEEE Trans. Power Delivery, vol. 26, no. 3, pp. 1793–1802, Jul. 2011.
[63] C. K. Jung, J. B. Lee, X. H. Wang, and Y. H. Song, "Wavelet based noise cancellation technique for fault location on underground power cables," Electric Power Systems Research, vol. 77, no. 10, pp. 1349-1362, Aug. 2007.
[64] M. Gilany, D. k. Ibrahim, and E. S. Tag Eldin, "Traveling-wave-based fault location scheme for multiend-aged underground cable system," IEEE Trans. Power Delivery, vol. 22, no. 1, pp. 82-89, Jan. 2007.
[65] P. Chen and K. Wang, "Fault location technology for high-voltage overhead lines combined with underground power cables based on travelling wave principle," In Proc. APAP, Beijing, China, vol. 1, pp. 784-751, Oct. 2011.
[66] IEEE Power System Relaying Committee Working Group, "Single-phase tripping and auto re-closing of transmission lines," IEEE Trans., Power Delivery, vol. 7, no. 1, pp. 182-192, Jan. 1992.

[67] X. Lin, H. Weng, H. Liu, W. Lu, P. Liu, and Z. Bo, "A novel adaptive single-phase reclosure scheme using dual-window transient energy ratio and mathematical morphology," IEEE Trans. Power Delivery, vol. 21, no. 4, pp. 1871–1877, Oct. 2006.

[68] S. Ahn, C. Kim, R. K. Aggarwal, and A. T. Johns, "An alternative approach to adaptive single pole auto-reclosing in high voltage transmission systems based on variable dead time control," IEEE Trans., Power Delivery, vol. 16, no. 4, pp. 676-686, Oct. 2001.

[69] M. Khodadadi, M. R. Noori, S. M. Shahrtash, "Noncommunication adaptive single-pole autoreclosure scheme based on the acusum algorithm," IEEE Trans., Power Delivery, vol. 28, no. 4, pp. 2526-2533, Oct. 2013.

[70] R. Niaz Azari, M. A. Chitsazan, I. Niazazari, "Optimal recloser setting, considering reliability and power quality in distribution networks", American Journal of Electrical Power and Energy Systems. Vol. 6, No. 1, 2017, pp. 1-6.

[71] A. Ghasemkhani, H. Monsef, A. Rahimi-Kian, and A. Anvari-Moghaddam, "Optimal design of a wide area measurement system for improvement of power network monitoring using a dynamic multiobjective shortest path algorithm," IEEE Systems Journal, Early Access.

[72] A. Ghasemkhani, A. Anvari-Moghaddam, J. M. Guerrero, and B. Bak-Jensen, "An Efficient Multi-objective Approach for Designing of Communication Interfaces in Smart Grids," Proceedings of IEEE PES Innovative Smart Grid Technologies, Ljubljana, Slovenia (ISGT Europe 2016), Oct. 2016.

[73] F. Zhalefar, M. R. Dadash Zadeh, T. S. Sidhu, "A high-speed adaptive single-phase reclosing technique based on local voltage phasors," IEEE Trans., Power Delivery, vol. PP, no. 99, 2015.

[74] V. H. Serna Reyna, J. C. Rivera Velázquez, H. E. Prado Félix, H. J. Altuve Ferrer, D. S. Escobedo, and J. G. Guerrero, "Transmission line single-pole tripping: field experience in the western transmission area of Mexico," 37th Annual Western Protective Relay Conference, Spokane, Washington, Oct. 2010.

[75] B. Keyvani, M. Karbalaye Zadeh, and H. Lesani, "Stability enhancement of multi-machine systems using adaptive reclosing of transmission lines," Electrical Power and Energy Systems, vol. 62, pp. 391-397, Nov. 2014.

[76] V. V. Terzija, and H. Koglin, "On the modeling of long arc in still air and arc resistance calculation," IEEE Trans., Power Delivery, vol. 19, no. 3, pp. 1012-1017, Jul. 2004.

[77] V. V. Terzija and H. Koglin, "Long arc in free air: laboratory testing, modelling, simulation and model-parameters estimation," Generation, Transmission and Distribution, IEE Proceedings, vol. 149, no. 3, pp. 319-325, 2002.

[78] Z. M. Radojevic´ and J. R. Shin, "New digital algorithm for adaptive reclosing based on the calculation of the faulted phase voltage total harmonic distortion factor," IEEE Trans., Power Delivery, vol. 22, no. 1, pp. 37-41, Jan. 2007.

[79] S. Jamali and A. Parham, "New approach to adaptive single pole auto-reclosing of power transmission lines," Generation, Transmission & Distribution, IET, vol. 4, no. 1, pp. 115-122, 2010.

[80] S. Jamali and N. Ghaffarzadeh, "Adaptive single-pole auto-reclosure for transmission lines using sound phases currents and wavelet packet transform," Electric Power Components and Systems, vol. 38, no. 14, pp. 1558-1576, Dec. 2010.

[81] M. R. Dadash Zadeh, I. Voloh, M. Kanabar, and Y. Xue, "An adaptive HV transmission lines reclosing based on voltage pattern in the complex plane," 65th Annual Conference for Protective Relay Engineers, College Station, Texas, USA pp. 85-95, Apr. 2012.

[82] Z. M. Radojevic´ and J. R. Shin, "New one terminal digital algorithm for adaptive reclosing and fault distance calculation on transmission lines," IEEE Trans., Power Delivery, vol. 21, no. 3, pp. 1231-1237, Jul. 2006.

[83] I. K. Yu and Y. H. Song, "Development of novel adaptive single-pole autoreclosure schemes for extra high voltage transmission systems using wavelet transform analysis," Electric Power Systems Research, vol. 47, pp. 11–19, 1998.
[84] O. Karacasu and M. H. Hocaoglu, "An Adaline based arcing fault detection algorithm for single-pole autoreclosers," Electric Power Systems Research, vol. 81 pp. 367–376, 2011.
[85] D. Lin, H. Wang, D. Lin, and B. He, "An adaptive reclosure scheme for parallel transmission Lines with shunt reactors," IEEE Trans. Power Delivery, vol. 30, no. 6, pp. 2581-2589, Dec. 2015.
[86] Z. Radojevic, V. Terzija, G. Preston, S. Padmanabhan, and D. Novosel, "Smart overhead lines autoreclosure algorithm based on detailed fault analysis," IEEE Trans., Smart Grid, vol. 4, no. 4, pp. 1829-1838. Dec. 2013.
[87] H. Khorashadi-Zadeh and Z. Li, "Design of a novel phasor measurement unit-based transmission line auto reclosing scheme," Generation, Transmission & Distribution, IET, vol. 5, no. 8, pp. 806-813, 2011.
[88] M. R. Dadash Zadeh and R. Rubeena, "Communication-aided high-speed adaptive single-phase reclosing," IEEE Trans., Power Delivery, vol. 28, no. 1, pp. 499-506, Jan. 2013.
[89] F. D. Zahlay and K. S. Rama Rao, "Neuro-Prony and Taguchi's methodology-based adaptive autoreclosure scheme for electric transmission systems," IEEE Trans., Power Delivery, vol. 27, no. 2, pp. 575-582, Apr. 2012.
[90] J. F. Adami, P. M. Silveira, M. L. B. Martinez, R. C. Perez, and A. C. Dallbello, "New approach to improve high-voltage transmission line reliability," IEEE Trans., Power Delivery, vol. 24, no. 3, pp. 1515-1520, Jul. 2009.
[91] A. N. Milioudis, G. T. Andreou, and D. P. Labridis, "Detection and location of high impedance faults in multiconductor overhead distribution lines using power line communication devices," IEEE Trans., Smart Grid, vol. 6, no. 2, pp. 894-902, Mar. 2015.
[92] J. M. Silva and B. Whitney, "Evaluation of the potential for power line carrier (PLC) to interfere with use of the nationwide differential GPS network," IEEE Trans. Power Delivery, vol. 17, no. 2, pp. 348-352, Apr. 2002.
[93] IEEE Guide for Power-Line Carrier Applications, IEEE Standard 643–2004, IEEE Power Eng. Soc.
[94] S. H. Horowitz and A.G. Phadke, "Power System Relaying," 3rd ed, Ch. 6, John Wiley & Sons, Ltd, West Sussex, England 2008.
[95] Requirements for Power-Line Coupling Capacitors and Coupling Capacitor Voltage Transformers (CCVT), ANSI Standard C93.2, American National Standards Institute.
[96] L. Prikler, M. Kizilcay, G. Ban, and P. Handl, "Improved secondary arc models based on identification of arc parameters from staged fault test records," Power Syst. Comput. Conf., Sevilla, Spain, Jun. 2002.
[97] EMTP-RV 3, Secondary Arc Example, [Online]. Available: http://emtp-software.com/try-buy
[98] J. E. Harry, "A power frequency plasma torch for industrial process heating," IEEE Trans. Industry and General Applications, vol. IGA-6, no. 1, pp. 36-42, Jan. 1970.
[99] C. Jaipradidtham, "Probability parameter estimation of outage rate effects for lightning overvoltage analysis on 500 kV EHV double circuit transmission lines using neural networks," IPEC, vol. 2, Marina Mandarin, Singapore, pp.803-808, 2005.
[100] EMTP-RV 3, Lightning Example, [Online]. Available: http://emtp-software.com/try-buy
[101] S. L. Zimath, M. A. Ramos, J. S. Filho, J. M. Beck, and N. Mueller, "Traveling wave-based fault location experiences," in Proc. Protective Relay Eng., College Station, TX, pp. 1-7, Mar.-Apr. 2010.

[102] R. Jalilzadeh Hamidi and H. Livani, "Traveling wave-based fault location algorithm for hybrid multi-terminal circuits," IEEE Trans. Power Del., vol. 32, no. 1, pp. 135-144, Feb. 2017.
[103] C. A. Apostolopoulos and G. N. Korres, "A novel fault location algorithm for double-circuit transmission lines without utilizing line parameters," IEEE Trans. Power Del., vol. 26, no. 3, pp. 1467–1478, Jul. 2011.
[104] R. Razzaghi, G. Lugrin, F. Rachidi, and M. Paolone, "Assessment of the influence of losses on the performance of the electromagnetic time reversal fault location method," IEEE Trans. Power Del., Early Access Article, 2016.
[105] M. Ando, E. O. Schweitzer, and R. A. Baker, "Development and field-data evaluation of single-end fault locator for two-terminal HVDC transmission lines part 2: algorithm and evaluation," IEEE Trans. Power App. and Syst., vol. PAS-104, no. 12, pp. 3524-3530, Dec. 1985.
[106] R. H. Salim, K. R. C. de Oliveira, and A. S. Bretas, "Fault detection in primary distribution systems using wavelets," in Proc. IPST, Lyon, France, Jun. 2007.
[107] Z. Wang, S. McConnell, R. S. Balog, and J. Johnson, "Arc fault signal detection - Fourier transform VS. wavelet decomposition techniques using synthesized data," in Proc. PVSC, Denver, CO., pp. 3239-3244, Jun. 2014.
[108] S. M. Tayebi and A. Kazemi, "A novel fault direction discrimination and location technique for three-terminal transmission lines," Proc. of Int. Conf. on Applied Superconductivity and Electromagnetic Devices, Sydney, Australia, pp. 92-96, Dec. 2011.
[109] L. Peretto, R. Sasdelli, and R. Tinarelli, "On uncertainty in wavelet based signal analysis," IEEE Trans. Instrum. Meas., vol. 54, no. 4, pp. 1593–1599, Aug. 2005.
[110] A. Borghetti, M. Bosetti, M. Di Silvestro, C. A. Nucci, and M. Paolone, "Continuous-wavelet transform for fault location in distribution power networks: definition of mother wavelets inferred from fault originated transients," IEEE Trans. Power Syst., vol. 23, no. 2, pp. 380-388, May 2008.
[111] P. E. Argyropoulos and H. Lev-Ari, "Wavelet customization for improved fault location quality in power networks," IEEE Trans. Power Del., vol. 30, no. 5, pp. 2215-2223, Oct. 2015.
[112] F. V. Lopes, D. Fernandes Jr, and W. L. A. Neves, "Fault location on transmission lines based on travelling waves," IPST, Delft, the Netherlands, Jun. 2011.
[113] F. V. Lopes, D. Fernandes Jr., and W. L. A. Neves, "Transients detection in EHV transmission lines using Park's transform," IEEE PES T&D, Orlando, FL., pp. 1-6, May 2012.
[114] F. V. Lopes, D. Fernandes, and W. L. A. Neves, "A traveling-wave detection method based on Park's transform for fault locators," IEEE Trans. Power Del., vol. 28, no. 3, pp. 1626-1634, Jul. 2013.
[115] Z. Moravej, M. Movahhedneya, G. Radman, and M. Pazoki, "Effective fault location technique in three-terminal transmission line using Hilbert and discrete wavelet transform," in Proc. EIT, Dekalb, IL, pp. 170-176 May. 2015.
[116] A. Bernadic and Z. Leonowicz, "Determining of fault location with Hilbert–Huang transform on XLPE cables between land and offshore substations," in Proc. EEEIC, Krakow, Poland, pp. 61-64, May 2014.
[117] A. Bernadic and Z. Leonowicz, "Fault location in power networks with mixed feeders using the complex space-phasor and Hilbert–Huang transform," Elec. Pow. and Ener. Syst., vol. 42, pp. 208-219, 2012.

[118] R. Prony, “Essai éxperimental et analytique: sur les lois de la dilatability é de uides élastique et sur celles de la force expansive de la vapeur de l'alkool, à di_érentes temperatures,” Journal de l'École Polytechnique Floréal et Plairial, vol. 1, cachier 22, pp. 24-76, 1795.
[119] T. K. Sarkar and O. Pereira, “Using the matrix pencil method to estimate the parameters of a sum of complex exponentials,” IEEE Trans. Antennas and Propagation, vol. 37, no. 1, pp. 48-55, Feb. 1995.
[120] R. Rezaiesarlak and M. Manteghi, “Short-time matrix pencil method for chipless RFID detection applications,” IEEE Trans. Antennas and Propagation, vol. 61, no. 5, pp. 2801-2806, May. 2013.
[121] R. Rezaiesarlak and M. Manteghi, “Accurate extraction of early-/late-time responses using short-time matrix pencil method for transient analysis of scatterers,” IEEE Trans. Antennas and Propagation, vol. 63, no. 11, pp. 4995-5002, Nov. 2015.
[122] M. Davoudi, J. Sadeh, and E. Kamyab, “Parameter-free fault location for transmission lines based on optimisation,” IET Gen., Trans., and Dist., vol. 9, no. 11, pp. 1061-1068, 2015.
[123] J. Niiranen, S. Seman, J. Matsinen, R. Virtanen, and A. Vilhunen, “Technical Paper: Low voltage ride-through testing of wind turbine converters at ABB helps wind turbines meet the requirements of IEC 61400-21 more quickly,” ABB, Helsinki, Finland, Oct. 2016.
[124] AMETEK. (2014). TR-2000 Multi-Function Recorder. AMETEK Power Instruments, Rochester, NY, USA, [Online]. available: http:// www.ametekpower.com
[125] KOCOS, (Aug., 2016), EPPE Power Quality Analyser, Korbach, Germany, available: http://www.kocos.com
[126] SEL, (Jun., 2016), SEL-2240 Axion, Pullman, WA, USA, available: http://www.selinc.com
[127] M. A. Chitsazan and A. M Trzynadlowski, “Harmonic mitigation in interphase power controllers using passive filter-based phase shifting transformer,” Energy Conversion Congress and Exposition (ECCE), 2016 IEEE, pp. 1-5, Sep. 2016.
[128] S. Akhlaghi and N. Zhou, “Adaptive multi-step prediction based EKF to power system dynamic state estimation,” Power and Energy Conference at Illinois (PECI), pp. 1-8, 2017.
[129] S. Akhlaghi, N Zhou, and Z Huang, “Adaptive adjustment of noise covariance in Kalman filter for dynamic state estimation,” IEEE Power and Energy Conference (PES) General Meeting, Chicago, IL, pp. 1-5, 2017.
[130] R. Jalilzadeh Hamidi, H. Livani, and R. Rezaeisarlak, “Traveling-wave detection technique using short-time matrix pencil method,” IEEE Trans. Power Del., Early Access.
[131] A. A. Girgis, W. B. Chang, and E. B. Makram, “A digital recursive measurement scheme for on-line tracking op power system harmonics,” IEEE Trans. Power Del., vol. 6, no. 3, pp. 1153-1160, Jul. 1991.
[132] R. K. Mehra, “Approaches to adaptive filtering,” IEEE Trans. Automatic Control, vol. 17, no. 5, pp. 693-698, 1972.
[133] Fredrik Gustafsson, “Adaptive filtering and change detection,” John Wiley & Sons, Ltd, West Sussex, England, 2000.
[134] D. A. Bodeman, “Adaptive estimation with change detection for streaming data,” PhD Thesis, University of London and the Imperial College, Nov. 2014.
[135] S. R. Mohanty, A. K. Pradhan, and A. Routray, “A cumulative sum-based fault detector for power system relaying application,” IEEE Trans. Power Del., Vol. 23, No. 1, pp. 79-86, Jan. 2008.
[136] F. V. Lopes, K. M. Silva, F. B. Costa, W. L. A. Neves, and D. Fernandes, Jr., “Real-Time traveling-wave-based fault location using two-terminal unsynchronized data,” IEEE Trans. Power Del., vol. 30, no. 3, pp. 1067-1076, Jun. 2015.

[137] M. Majidi, M. Etezadi-Amoli, and M. Sami Fadali, "A novel method for single and simultaneous fault location in distribution networks," IEEE Trans. Power Systems, vol. 30, no. 6, pp. 3368-3376, Nov. 2015.
[138] Available online: https://www.mccdaq.com/products/pdaq3s
[139] I. Sadinezhad, V. G. Agelidis, "On optimizing DSP implementation of the recursive-least-squares technique for real-time power system applications," IECON 2011 - 37th Annual Conference of the IEEE Industrial Electronics Society, Melbourne, Australia, pp. 640-645, Nov. 2011.
[140] H. Pourbabak and A Kazemi, "Islanding detection method based on a new approach to voltage phase angle of constant power inverters," IET Trans. Generation, Transmission, and Distribution, vol. 10, no. 5, pp. 1190-1198, Apr. 2016.
[141] A. Aghazadeh, I. Niazazari, N. Khodabakhshi, S. H. Hosseinian, and H. A. Abyaneh, "A new method of single-phase active power filter for AC electric railway system based on Hilbert transform," IEEE International Conference on Smart Energy Grid Engineering (SEGE), pp. 1-7, Ontario, Canada, Aug. 2013.
[142] R. Jalilzadeh Hamidi, H. Khodabandelou, H. Livani, and M. Sami-Fadali, "Hybrid state estimation using distributed Compressive Sensing," Power and Energy Society General Meeting (PESGM), Boston, Massachusetts, pp. 1-5, Jul. 2016.